DESIGN, IMPLEMENTATION AND CHARACTERIZATION OF A MICROSCOPE CAPABLE OF THREE-DIMENSIONAL TWO COLOR SUPER-RESOLUTION FLUORESCENCE IMAGING

DISSERTATION ZUR ERLANGUNG DES NATURWISSENSCHAFTLICHEN DOKTORGRADES DER BAYERISCHEN JULIUS-MAXIMILIANS-UNIVERSITÄT WÜRZBURG

vorgelegt von

Sven Martin Proppert

aus Rheda-Wiedenbrück

Würzburg, 2014

To my family.

Zusammenfassung

In dieser Arbeit werden die Grundlagen der dreidimensionalen hochauflösenden Lokalisationsmikroskopie erarbeitet und daraus Spezifikationen für ein geeignetes Mikroskop abgeleitet. Zur Gewinnung der axialen Koordinate der Emission einzelner Farbstoffe wird die Punktspreizfunktion in der Detektion astigmatisch mithilfe einer zylindrischen Linse verändert.

Nach einer kurzen Einleitung in die Grundzüge der Optik und der Lokalisationsmikroskopie werden die Ursachen für typische Aberrationen besprochen, wie sie in der 3D-Lokalisationsmikroskopie häufig auftreten. Weiterhin wird der Einfluss dieser Aberrationen auf die erreichbare Präzision und Exaktheit des Lokalisationsprozesses behandelt. Mit dem Wissen aus diesen Überlegungen wurden Experimente entworfen und durchgeführt um die getroffenen Schlussfolgerungen zu validieren und zu demonstrieren, dass das vorgeschlagene Mikroskop dazu in der Lage ist, biologische Strukturen in den drei räumlichen Dimensionen aufzulösen. Weiterhin wird gezeigt, dass beinahe aberrationsfreie Mikroskopie großer Volumina prinzipiell möglich ist.

Während der Arbeit an dieser Promotion wurde eine neue Methode zur Gewinnung der axialen Koordinaten eingeführt. Diese auf kubischen B-splines basierende Interpolationsmethode stellte sich als anderen Routinen überlegen in der Kalibration eines Mikroskops und der anschließenden Auswertung von Messungen heraus. Deshalb wird dieses Verfahren in der vorliegenden Arbeit verwendet und erklärt.

Da diese Doktorarbeit auch den Anspruch hat, zukünftigen Studenten den Einstieg in die hochauflösende 3D Mikroskopie zu erleichtern, werden abschließend detaillierte Protokolle für spezifische Aspekte der zwei Farben 3D Lokalisationsmikroskopie zur Verfügung gestellt.

Abstract

This thesis reviews the fundamentals of three-dimensional super-resolution localization imaging. In order to infer the axial coordinate of the emission of single fluorophores, the point spread function is engineered following a technique usually referred to as astigmatic imaging by the introduction of a cylindrical lens to the detection path of a microscope.

After giving a short introduction to optics and localization microscopy, I outline sources of aberrations as frequently encountered in 3D-localization microscopy and will discuss their respective impact on the precision and accuracy of the localization process. With the knowledge from these considerations, experiments were designed and conducted to verify the validity of the conclusions and to demonstrate the abilities of the proposed microscope to resolve biological structures in the three spatial dimensions. Additionally, it is demonstrated that measurements of huge volumes with virtually no aberrations is in principle feasible.

During the course of this thesis, a new method was introduced for inferring axial coordinates. This interpolation method based on cubic B-splines shows superior performance in the calibration of a microscope and the evaluation of subsequent measurement and will therefore be used and explained in this work.

Finally, this work is also meant to give future students some guidance for entering the field of 3D localization microscopy and therefore, detailed protocols are provided covering the specific aspects of two color 3D localization imaging.

Acknowledgment

I am most grateful that Prof. Dr. Markus Sauer granted me the chance to work in his group and to write this thesis. I especially want to thank you as you encouraged me when times were rough and I hope we will fruitfully cooperate in the future.

I also want to thank Prof. Dr. Bert Hecht for kindly taking over the part of the second referee.

There are many co-workers who contributed to this work with critical discussions and the preparation of samples. Christian Franke as well as Thorge Holm always showed helpful interest in the fundamentals of the 3D localization process and Katharina Schücker was so kind as to prepare the synaptonemal complex. Anna Löschberger prepared the nuclear pore complex, Teresa Klein provided me with stained centrioles and Thorge Holm contributed nicely stained microtubules. Martin Pauli prepared the brain slices which are about to become an interesting project in the near future. If I would have had to do all the biology myself, it would have taken much longer to finish my work and I very much appreciate your help. It would as well have been significantly harder if I would have had to fiddle with the underlying physics solely on my own and the discussions helped a lot to get things straight.

I had the honor to work with three Master students who helped me in various ways. Daniela Wengler supported my initial work on Lightsheet microscopy, Ina Geier very independently set up an OpenSPIM microscope and Felix Rüdinger always tested my understanding of 3D localization with witty questions and conversations.

I also want to thank the technical assistants for helping me with cell culture issues and especially with the assembly of custom parts. You and the rest of the workgroup formed an inspiring environment that kept me going.

Sebastian van de Linde kindly introduced me to the *d*STORM technique and was always very supportive whenever I encountered problems. It has also been great fun to spend nights together (re-)assembling setups or getting acquainted with the local culture in the Eulenspiegel.

Patrick Zessin was not only interested in my work and spent some thoughtful discussions with me but he also became a good friend and mate for extensive sauna sessions. Cheers.

Thorge evolved to be a very special and dear colleague and friend as we shared a lot of fun in the lab, while skiing, sailing or late-evening-talking. It is my pleasure sharing a flat with you.

Well, most of a Phd's life happens in the lab or the office and I did not talk about the latter yet. I had the honor to share the office with Steve Wolter, Stefan Bollmann and Dominik Pfaff (among others). Each of you has some very special

Contents

1 Introduction

Super-resolution fluorescence microscopy is one of the booming fields of research of the last decade. It uses some tricks to circumvent the classical boundary, that no structures smaller than about 200 nm can be imaged *simultaneously* with visible light. I will describe in the following how researchers succeeded in gaining up to tenfold better resolutions by localizing single emitters at a time rather than imaging them all at once like in conventional microscopy. Whilst the technique is well established for two-dimensional (2D) imaging, I will later focus on the implementation of three-dimensional (3D) localization microscopy and provide solutions to the respective obstacles that were not trivial.

I suppose everybody who reads this thesis is well familiar with microscopy as well as fluorescence and thus I will not take a theoretically coherent approach as a book about the matter would, but will try to describe phenomena in the least complex form needed. For example, you need diffraction to describe classical resolution limits in microscopy and the advantages of super-resolution techniques, but geometrical optics is sufficient to get a grip on aberrations which are usually not too important for 2D localization microscopy but essential to understand for 3D – and are thus treated later in my thesis. I hope this topical order will help to get a sound understanding of how to locate a fluorophore precisely and accurately in 3D.

1.1 Classical limitations

The invention of (modern) microscopes in the late 19th century was a breakthrough especially in biological and medical research. Before, scientists were more or less restricted to studying organisms at a macroscopic level and zoology was still a major field in biology. Even though van Leeuwenhoek already discovered cells in the 17th century, only with the availability of reproducible optical instruments a closer look at living matter became possible and soon led to the general acceptance of cells as the basic units of life no matter whether we deal with simple single-cell organisms like bacteria or complex animals and humans.

Anatomists soon discovered that cells from different organs have different shapes and even neurons as a cellular entity and a fundamental unit of intelligence and mind were finally observed. But still, the first attempts suffered from a poor contrast as the (sub–)cellular environment is optically rather homogeneous. Thus, it is little wonder that fluorescent dyes were invented at this point in time. In combination with the progress in biochemical understanding and the resultant ability to specifically bind dye molecules to a target, the higher contrast by organelle-specific fluorescence was yet another breakthrough.

Still, the degree of understanding provided by optical microscopy was long time hampered by the fact, that the achievable resolution is limited by diffraction as Ernst Abbe described in one of his famous essays (Abbe, 1873). While his sound understanding of the theory behind microscopy combined with Carl Zeiss's ability to produce precise lenses led to the introduction of reliable microscopes, he also observed, that the amount of detail that can be extracted from a specimen is not limited by the magnification of the instrument but by the maximum angle under which an objective can collect (fluorescence–) light. To understand this, it helps to reduce the observed specimen to a single point emitter.

(a)   (b)
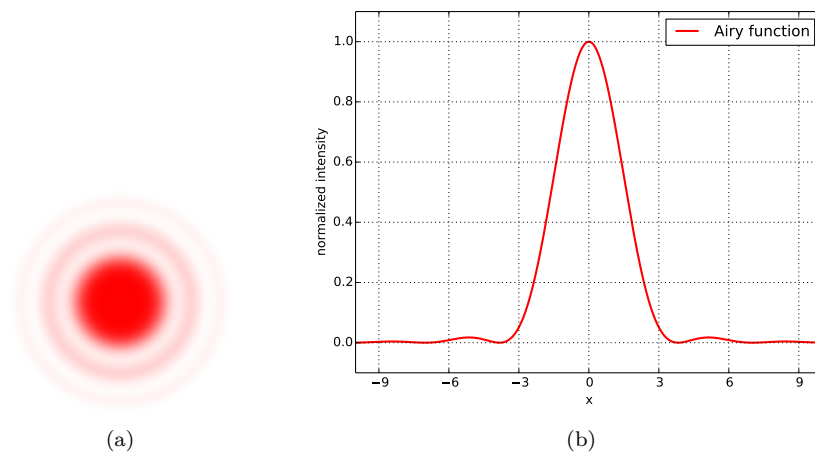
Figure 1.1: The image of a point emitter cannot be infinitely sharp and is always obscured by diffraction. a) shows a sketch of the observed emission pattern (not to scale) while b) is a plot of the functional relation describing the cross-section through the center of a PSF.

The emission pattern of an infinitely small point source imaged to a camera or sensor is always obstructed by the wavelike characteristics of light. Whenever

the light encounters an entrance pupil – and every lens is such a pupil because of its finite size – diffraction occurs. The resulting image is not a sharp point but a blurred pattern with a centered maximum and higher order rings as sketched in Fig. 1.1a with a theoretical line profile through the center given in Fig. 1.1b. Even though mathematically not overly correct, this blurred emission pattern is colloquially called PSF. This is not exactly true as the PSF is the function describing the spread of a point by an optical system and the emission pattern is the convolution of the object with the PSF. While the term PSF is mostly used to describe the imaging properties of a microscope, the term "optical transfer function" can usually be assumed equivalent. In the following the terms PSF, Airy function, and emission pattern will be used synonymously.

The intensity profile of the emission of a fluorescent particle can be described by a function of the observation angle θ (Eq. (1.1)) with I_0 being the maximum intensity of the PSF, and $J_1(x)$ the Bessel function of first kind and first order. The parameter x (Eq. (1.2)) is a function of θ, the wavelength of the detected light λ, the refractive index of the immersion medium n and the radius of the particle a. Mathematically, Eq. (1.1) is the intensity I of the Fraunhofer diffraction pattern occurring at a pinhole aperture illuminated from behind with parallel light.

$$I(\theta) = I_0 \left(\frac{2J_1(x)}{x} \right)^2 \tag{1.1}$$

$$x = k \, a \, n \, \sin(\theta) = \frac{2\pi}{\lambda} \, a \, n \, \sin(\theta) \tag{1.2}$$

Abbe realized that the minimum size of the full width at half maximum (FWHM) of a PSF can never be less than about half of the observed wavelength even if the maximum detected angle was 90° (Eq. (1.4)). Eq. (1.3) gives a short derivation: The intensity drops to half of its amount at $x \approx \pm 1.61$, the minimal distance observable is $d = 2a$.

$$
\begin{aligned}
x = 1.61 &= \frac{2\pi}{\lambda} \, a \, n \, \sin(\theta) \\
a &= \frac{1.61\lambda}{2\pi \, n \sin(\theta)} \\
d &= \frac{2 \cdot 1.61\lambda}{2\pi \, n \sin(\theta)} \\
&\approx \frac{\lambda}{2 \, n \sin(\theta)}
\end{aligned}
\tag{1.3}
$$

He also used the term numerical aperture (NA) for the product of refractive index of the medium immersing the lens (n) and the sine of the detected angle (θ) and is usually referred to with Eq. (1.4). The bottom line of this equation is, that no matter what optics are used, objects smaller than d will always be blurred as if their size actually was d and thus further magnification will not help distinguishing two adjacent particles but will only make their respective minimal PSF appear bigger. As initially stated, thus the ability to resolve small structures is restricted by the NA of the objective and not its magnification.

$$d = \frac{\lambda}{2\ n\ \sin(\theta)} = \frac{\lambda}{2\ \text{NA}} \tag{1.4}$$

For assessing the lateral resolution of an optical system, in 1903 Lord Rayleigh introduced the criterion, that two adjacent point sources are distinguishable if their separation is at least such that the maximum of emission pattern2 coincides with the first minimum of emission pattern1 (Rayleigh, 1903) (cf. Fig. 1.2). The first minimum of Eq. (1.1) is at $x = 3.83$ and calculations similar to that of the minimum size of a single PSF give the result in Eq. (1.5).

$$x = 3.83 = \frac{2\pi}{\lambda}\ a\ \text{NA}$$
$$d_{Rayleigh} = \frac{3.83}{2\pi}\frac{\lambda}{\text{NA}}$$
$$\approx 0.61\frac{\lambda}{NA} \tag{1.5}$$

While the aforementioned is valid for the lateral resolution, the axial resolution follows other rules. According to (Pawley, 2006), the axial resolution follows Eq. (1.6) and is thus, as a rule of thumb, about three– to four times worse than laterally.

$$z_{min} = \frac{2n\lambda}{\text{NA}^2} \tag{1.6}$$

If we take the objective mostly used throughout this thesis with NA = 1.15 and a deep-red emitting dye like Alexa Fluor 647 (Alexa647) with peak emission λ around 700 nm in aqueous environment (n = 1.33) as an example, the lateral resolution according to Eq. (1.5) is $d \approx 370$ nm, while Eq. (1.6) for the axial resolution gives $z_{min} \approx 1400$ nm.

As the resolution of optical systems is limited by the NA and the detected wavelength and the NA itself cannot be infinitely increased, scientists first succeeded to use shorter wavelengths finally resulting in the invention of electron micros-
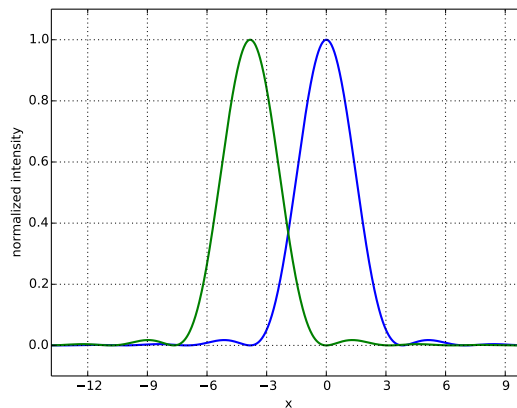
Figure 1.2: According to the Rayleigh criterion, the minimum distance between two simultaneously luminescent point sources is given when the maximum of emission pattern2 and the first minimum of emission pattern1 coincide.

copy (EM). EM benefits from the fact that even small particles as electrons show a wave-like behavior with very short wavelengths and in theory, the achievable resolution should go down to the nanometer regime. Unfortunately, even today the electron optics (focusing magnets) suffer from poor quality and especially in biological research the extensive sample preparation is a major drawback.

On the other hand, the limits of optical imaging were pushed further by the invention of confocal laser scanning microscopy (CLSM) where a confocal point excitation is scanned over the specimen. The resulting fluorescence light can only originate from the diffraction limited focus and de-focused light is blocked by a pinhole. Thus the reconstructed image shows a much higher contrast in comparison to an image with epifluorescent excitation. Despite the benefits from the higher contrast it is important to realize that this technique is still diffraction limited.

In order to bypass the diffraction limit with visible light, stimulated emission depletion (STED) and structured illumination (SIM) were invented. STED (Hell and Wichmann, 1994) is also a confocal scanning technique but in addition to the excitation laser, a second doughnut-shaped depletion laser forces excited fluorophores to stimulated emission and thus narrows the area where fluorescence can occur to a sub-diffraction size of about 50 nm. In theory, even higher resolutions are possible as the size of the minimum of the depletion laser is only a function

of the laser power but one should be aware of the fact that at high powers the depletion laser itself can also excite fluorophores with a non-negligible possibility. Despite the lateral resolution enhancement, STED as originally introduced only has the same axial resolution as a confocal microscope. SIM (Gustafsson, 2000) on the other hand is a widefield technique that makes use of patterned illumination that is successively rotated by several degrees. The respective images show differing fluorescence modulations and can be computationally combined with an approximate twofold resolution increase in all dimensions as compared to standard microscopy.

1.2 Localization microscopy

The limitation of classical optical microscopy as discussed in the previous section only holds true for **simultaneously luminescent stains of the same kind**. That is, if there was any means to distinguish two adjacent fluorophores by sequential imaging, each PSF could be localized independently from others. Here and in the following, **localization** means the determination of the center (point of maximum intensity) of a fluorescent spot. The advantage is, that the peak-determination can be much more precise than the distribution itself. To give some sort of analogy: Even though a hill might be a very big object, we can easily tell with a precision of a few meters where to find the peak.

The most obvious feature which can differ from one stain to another is their spectrum, i.e., their color – a feature that is widely used in multi-color fluorescent microscopy. Another characteristic could be the fluorescence lifetime. But as for the color, the variety of stains with a big enough difference in any of these features is way too small to bypass the resolution limit significantly by ensuring that adjacent fluorophores can be distinguished by their respective spectral– or lifetime properties. Thus it appears that employing different dyes can hardly be the key to better resolutions.

But if on the other hand we are able to separate fluorophores not by lifetime or color but by the time when they show luminescene, the localization is straightforward. A first attempt leading in this direction was the exploit of the blinking of single quantum dots (QD) (Lidke et al., 2005). But the blinking characteristics proved not to be sufficient to resolve a densely labeled structure, i.e., even though the QDs are switching between a fluorescent on– and a dark off-state, the off-states are too short and thus too many QDs reside in their on-state simultaneously. But then it was shown, that organic dyes or fluorescent proteins can

show fluorescence switching with sufficient switching ratios (Bates et al., 2005; Heilemann et al., 2005).

First, in 2006 the photoactivated localization microscopy (PALM) and FPALM approaches (Betzig et al., 2006; Hess et al., 2006) showed that it is possible to activate only a very sparse subset of fluorescent proteins (FP) to a fluorescent on-state, read out the signal, bleach them and activate another subset afterward. By repeating this scheme many times, they were able to localize enough FPs to resolve cellular structures with sub-diffraction resolution. A similar approach called stochastic optical reconstruction microscopy (STORM) using switchable pairs of organic dyes (Rust et al., 2006) was also published in 2006 and in 2008, direct STORM (*d*STORM) (Heilemann et al., 2008, 2009; van de Linde et al., 2011) simplified that method to the use of single organic dyes.

While those approaches (and only a few have been mentioned) differ in some aspects, they all follow the same strategy and will thus be pooled to **localization microscopy** approaches:

1. registration of a sparse fluorophore subset

2. activation of another subset

3. many repetitions

4. localization of each individual fluorophore PSF

5. summation of all found localizations to a reconstructed image

Because the details of localization microscopy exceed the scope of this thesis, I recommend the study of one of the many reviews published, e.g., (Galbraith and Galbraith, 2011; van de Linde and Sauer, 2014; Klein et al., 2014) and will only sketch the position determination process. As already indicated and schematically shown in Fig. 1.3, the center of a single PSF can be precisely determined if there are no disturbances in the vicinity. Usually, the Airy pattern is approximated with a two-dimensional Gaussian normal distribution as in Eq. (1.7), because the loss in localization precision in negligible, the method is well described (Cheezum et al., 2001; Thompson et al., 2002; Mortensen et al., 2010; Stallinga and Rieger, 2010) and the computational cost is very low compared to fitting with a physically derived model.

$$G = B + \frac{A}{2\pi\sigma_x\sigma_y} \exp\left[-\frac{1}{2}\left(\frac{(x-x_0)^2}{\sigma_x^2} + \frac{(y-y_0)^2}{\sigma_y^2}\right)\right] \qquad (1.7)$$
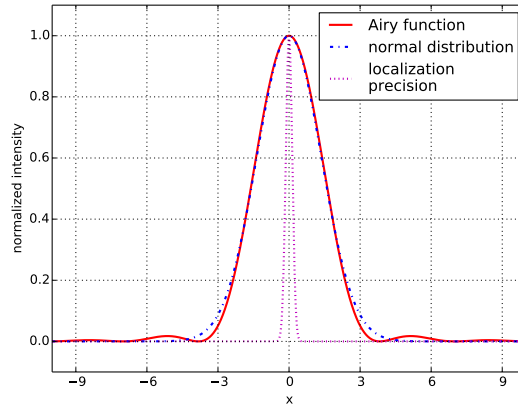
Figure 1.3: The PSF of a single fluorophore (red) can be fitted by a Gaussian normal distribution (blue). The localization precision (magenta) of the center position determination is significantly narrower than the PSF.

Fitting a Gaussian to a PSF gives the center coordinates (x_0, y_0) and the respective standard deviations of the Gaussian (σ_x, σ_y), an amplitude factor A that corresponds to the collected number of photons and the background level B. Thompson et al. calculated (Thompson et al., 2002) the precision of the center localization Δx and Mortensen et al. (Mortensen et al., 2010) modified their findings to the expression given in Eq. (1.8) with pixelsize a, the variance of the local background b, σ as computed with Eq. (1.7) and the number of photons N. Most simply speaking, for a given microscope the achievable precision of a localization scales with the inverse of the number of photons collected (Eq. (1.9)).

$$\langle \Delta x^2 \rangle = \frac{\sigma^2 + \frac{a^2}{12}}{N} \left(\frac{16}{9} + 8\pi b^2 \frac{(\sigma^2 + \frac{a^2}{12})}{a^2 N} \right) \tag{1.8}$$

$$\Delta x \approx \frac{1}{\sqrt{N}} \tag{1.9}$$

Thompsons's and Mortensen's considerations led to the common belief that for successful implementation of localization microscopy it is helpful to take an objective lens with an as high as possible NA – usually oil immersion objectives of NA = 1.4 or higher. As we deal with very small – point-like – emitters and

we can assume for simplicity that their bond to the labeled structure is flexible enough to allow rotation of the dipole orientation, the light of a single fluorophore is isotropically distributed. An ideal objective with a maximum acceptance angle θ of 90° would detect every photon emitted towards the microscope, i.e., half of the full spherical emission (cf. Fig. 1.4). The light collection efficiency of an objective can thus be judged by comparing the detected amount of photons with the ideal. As derived in Eq. (1.10), the number of collected photons is solely a function of the NA and the refractive index of the sample n_{medium}.

$$dA = r^2 d\phi' \sin(\theta')d\theta' \qquad \text{(cf. Fig. 1.4)}$$
$$S = \text{surface of half a sphere} = 2\pi r^2$$

$$I = \frac{\text{detected surface}}{\text{whole surface}} = \frac{1}{S}\int dA$$
$$= \frac{1}{2\pi r^2}\int_{\phi_{min}}^{\phi_{max}}\int_{\theta_{min}}^{\theta_{max}} r^2 d\phi' \sin(\theta')d\theta'$$
$$= \frac{1}{2\pi r^2}r^2\int_0^{2\pi} d\phi'\int_{\theta_{min}}^{\theta_{max}}\sin(\theta')d\theta'$$
$$= \frac{1}{2\pi}\int_{\theta_{max}}^0 d\theta' 2\pi \sin(\theta')$$
$$I = 1 - \cos(\theta_{max})$$
$$\theta_{max} = \sin^{-1}\left(\frac{NA}{n}\right)$$

$$I = 1 - \cos\left(\sin^{-1}\left(\frac{NA}{n_{medium}}\right)\right) \qquad (1.10)$$

It is perfectly reasonable to use oil immersion objectives if the studied specimen adheres to the cover slip, is either very flat, or only the bottommost part is of interest and localization microscopy is used in two dimensions only, i.e., the lateral coordinates (x,y) are determined, but the axial z is assumed to be the same for all emitters. In this scenario it is valid to pay attention to get the highest precision possible because the accuracy for all localizations is the same (cf. Fig. 1.5). Therefore, if there is any systematic shift from the true position, that shift will apply to the whole image.

On the other hand, in three dimensions it becomes essential to make sure, that all fluorophores are localized not only precisely but also accurately. While
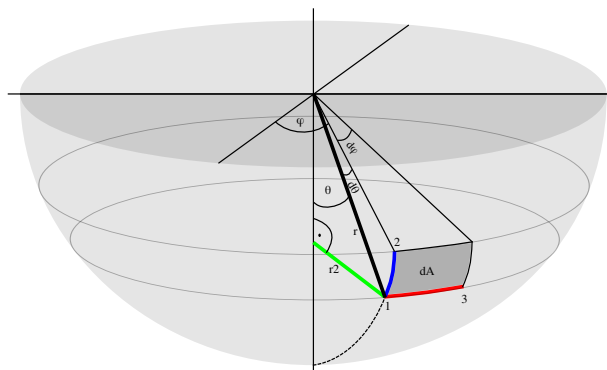
Figure 1.4: Detected fraction of the isotropic emission sphere. For the collection of as much light as possible, the objective must have a large angle of acceptance θ.

the precision is more or less determined by the detected photon budget, the accuracy is determined by the amount and kind of aberrations of the optical system. Unfortunately, all objectives suffer from distinct kinds of aberrations that will transform the resultant image (the objective's immersion medium and the refractive index of the specimen are the key characteristics). If one does not have a sound understanding of whether or not the measurement is disturbed, the use of inappropriate optics may even lead to false conclusions. Thus it is inevitable for a good calibration that the microscope is fit to the individual specimen that is to be measured.
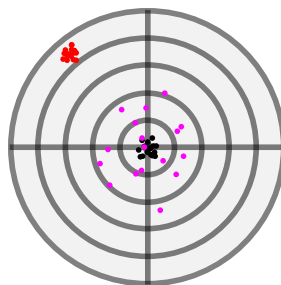
Figure 1.5: This figure displays the meaning of the terms "precision" and "accuracy" as they might not be trivial. The color of the dots encodes the three different regimes: red: low accuracy, high precision; magenta: high accuracy, low precision; black: high accuracy, high precision.

I will take a step back in the theory of optics for the rest of this introduction and will recap the fundamentals of geometrical optics and image aberrations because

the next chapter will deal with real image perturbations and their implications for the assembly of a 3D localization microscope.

1.3 A brief summary of geometrical optics

After all the proceedings in the field of super-resolution it became more and more apparent, that the extension of the technique into the third dimension is desirable. In principle, there should be no big deal in accepting slightly de-focused PSFs and find ways to assign a z-coordinate to each degree of de-focusing. Apparently, the precise control and sound understanding of a PSF is crucial for successful calibrations (as will be discussed in more detail in chapter 2). That is, why I want to shortly recapitulate optics, even though having already talked about more complex topics. In the successive section I will outline the aberrations that can occur and have to be avoided.

Geometrical optics is an old story and well described in various books and lectures. For deeper insight I recommend the book "Optics" by Eugene Hecht (Hecht, 2002) – also available in German (Hecht, 2014) – because it is overall well written and understandable. German readers might also take a look at the second volume of the "Demtröder Experimentalphysik" (Demtröder, 2006) and a more theoretical approach can be found in "Principles of optics" by Max Born and Emil Wolf (Born and Wolf, 2002). The knowledge in this and the following section 1.4 about aberrations is adapted from these books and some given information may originate from similar literature.

Nevertheless, I want to give a short introduction to the field as especially aberrations (see section 1.4) become a serious issue in 3D localization microscopy and can be sufficiently introduced using basic concepts in optics. Optics in general describes the propagation of electromagnetic waves through media with refractive index n and their behavior at (curved) interfaces of different refractive index. As long as the medium is homogeneous and of constant refractive index, a light travels without change in its direction following **Fermat's principle** (by Pierre de Fermat):

A ray of light always takes the path that minimizes the time needed.

A generalized emitter can usually be assumed to be a point source with isotropic behavior. This emission results in a spherical electromagnetic wave. In order to get from wave optics to the easier to treat description of geometrical optics, it can be assumed for simplicity, that far away from the emitter this spher-

ical wave can be described by a bundle of equally spaced parallel rays. Please be aware, that this simplification is not valid on small scales and for example fails to describe the real focus that is not infinitely sharp as in geometrical optics but broadened by diffraction. I will come back to wave optics only if needed.

Furthermore, I will only treat simple paraxial cases in this section. That means, that lens diameters are considered significantly larger than the diameters of the light bundles and only small angles between the bundle and the optical axis – an imaginary straight line, along which the centers of all optical elements are aligned – are allowed. The light is also restricted to the close proximity of the optical axis and shall be monochromatic. These simplifications (listed below) lead to imaging without aberrations.

- $\sin(\alpha) = \alpha$, $\cos(\alpha) = 1$

- as a result of the moderate curvature of optical elements around its center, the angles of incidence remain small

I will then describe in section 1.4 the more general cases of non-paraxial optics with the resultant aberrations.
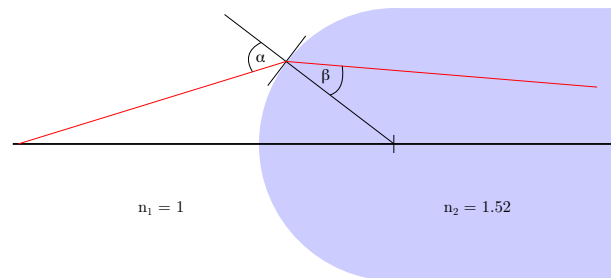
Figure 1.6: Refraction at a curved boundary surface between refractive indices $n_1 = 1$ (air) and $n_2 = 1.52$ (glass).

At refractive index boundaries such as the interface between glass and water, light gets refracted. In general, the angle between the incident light ray and a straight line perpendicular to the surface is bigger while in the optically thinner medium whereas the refracted ray leaves the boundary under a more acute angle as sketched in Fig. 1.6. The behavior of refracted light is described by **Snell's Law** (Eq. (1.11)), with the angle of incidence α, angle after refraction β and the respective refractive indices n_1 and n_2 as shown in Fig. 1.6. If the refractive indices in Fig. 1.6 were switched, the boundary would not lead to converging but diverging light.

$$n_1 \cdot \sin(\alpha) = n_2 \cdot \sin(\beta) \tag{1.11}$$

Events, where only one refractive index boundary is encountered, are rather rare. If the object which exhibits a different refractive index has a second surface the light can pass we may generally call it a lens. These lenses – usually but not necessarily with spherical surfaces and made of glass – are widely used to manipulate light. I have summarized some sorts of common lenses as they are used in laboratories or may be used in eyeglasses in Fig. 1.7. While the converging (a) - c)) and diverging (d) - e)) lenses are very simple, lens f) represents a doublet of two lenses of different refractive indices. I will come back to this kind of lens in section 1.4.6. Here it should only indicate the existence of more complex optical instruments such as lenses correcting for image errors and highly corrected microscope objectives.
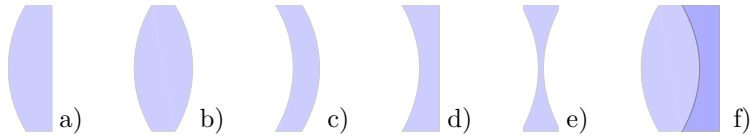
Figure 1.7: Some common shapes of lenses.a) - c): converging lenses, d) - e): diverging lenses, f): a doublet of a converging– and a diverging lens of different refractive indices.

Lenses are mostly used for imaging and / or magnifying (distant) objects. The fundamental properties of the formation of real– and virtual images via a lens are depicted in Fig. 1.8. An Object O is located in the distance s in front of a converging lens with focal length f. Three fundamental rays can be used to assess size and location of the image I: Light emitted parallel to the optical axis is refracted and passes the rear focal point F, while light passing the focal point F' in front of the lens will be parallel to the optical axis behind the lens. A third ray from the tip of the object through the intersection of the lenses' principal plane (PP) and the optical axis can be used. The intersection of those rays indicates the real image of the tip of O in the distance i.

The location of an image or the object can as well be calculated if two of the following are known: focal length (f), object distance (s) and image distance (i). The relation of these three variable is given by the **geometrical lens equation** (1.12):

$$\frac{1}{f} = \frac{1}{s} + \frac{1}{i} \tag{1.12}$$
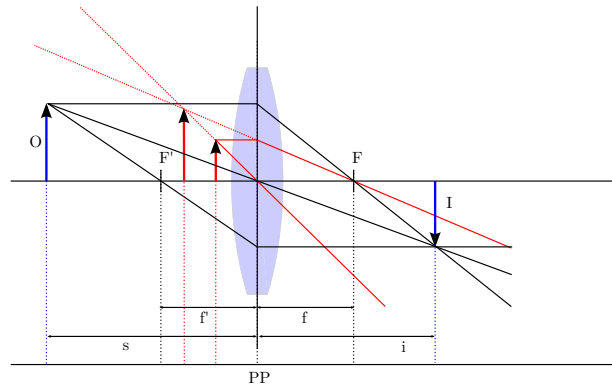
Figure 1.8: Image formation in geometrical optics: An object O is located in the distance s in front of a converging lens with focal length f. The image I forms at a distance i behind the lens. The red arrows and light paths indicate the formation of a virtual image.

Because lenses are frequently used as magnifiers, I will shortly explain that case as well. If the object is closer to the lens than f, there will be no real image but an imaginary image as indicated by the red rays and arrows in Fig. 1.8. The smaller red arrow is the object and the rays emitted by its tip appear as if they would originate from an imaginary point that can be determined by tracing them backwards. The image is imaginary in this case, because it cannot be detected by any sensor placed in the image distance.

Another interesting quantity is the magnification of the optical system, i.e., how big the image is compared to the object size. For known image– and objective distances or one of those quantities and the lenses' focal length, the magnification A can be calculated by any of equations (1.13):

$$
\begin{aligned}
A = \frac{I}{S} &= \frac{i}{s} \\
&= \frac{i-f}{f} = \frac{f}{s-f}
\end{aligned}
\tag{1.13}
$$

Some special imaging conditions are summed up in Tab. 1.1. Without claiming completeness these resemble some basic rules of thumb I found useful and I hope they might help others as well.

Of course, systems of more than one lens can be assembled and for introductory purpose, I will spend some words on two-lens-systems. Two-lens-systems are often used to magnify light beams. Contrary to magnifying glasses, these tele-

Table 1.1: Summary of some imaging conditions for converging lenses. The way the image location annotation is to be understood: left is where the light enters the lens (in front of the lens) and right denotes the part where the light has passed through the lens (behind the lens).

condition	image size and location
$b = g = 2f$	$A = \frac{i}{s} = 1$, right
$f < g < 2f$	$b > 2f$, A > 1, right
$g > 2f$	$A < 1$, right
$g \leq f$	imaginary image, A≥ 1, left

scopes produce a real image that can be seen or recorded. The magnification of a telescope is given by Eq. (1.14) where f_{obj} is the focal length of the lens closer to the object and f_{ocu} denotes the focal length of the detector-sided lens. The prerequisite for a proper magnification is that the focal points of lens one and two coincide. A simple example: If $f_1 = 25$ mm and $f_2 = 50$ mm, the distance between both lenses must be exactly 75 mm. If this condition was not true, the two-lens-system would not be a telescope with a focus at infinite distance but a generalized lens with very long focal length or a negative one (diverging lens).

$$A = \frac{f_{obj}}{f_{ocu}} \tag{1.14}$$

It is often desired to deliberately de-tune a telescope, that is, to take two lenses but put them in a further distance than $f_1 + f_2$ because we then end up with a very long focal length and more importantly, the focal length of that system is a function of the distance d between the lenses. Both aspects come very handy, for example if a laser has to be focused on the back focal plane of an objective but as the objective operates in different locations on the optical axis, some readjusting of the focus is necessary. And on the other hand, it is much easier to take two lenses than to overcome long distances with a single lens (for example, the distance between objective and last illumination lens can easily be more than 500 mm).

As already mentioned, the focal length of that system is a function of the distance between the lenses and is given by Eq. (1.15). In practice, the needed spacing is rarely calculated but found by "trial and error", but nevertheless the

equation is on the other hand useful to get some estimates that help in the design of a fluorescence localization microscope.

$$\frac{1}{F} = \frac{1}{f_1} + \frac{1}{f_2} - \frac{d}{f_1 \cdot f_2} \tag{1.15}$$

Without deeper discussion, I want to note that a third important aspect comes into play in the assembly of the illumination of a microscope: As a focusing two-lens-system is still a detuned telescope, of course the illumination light, i.e., the laser beam gets expanded and thus the illuminated area in the specimen can comfortably adjusted by using the right pair of lenses. The laser has to be expanded by an appropriate amount, because if on one hand the focusing angle was very acute, the laser would only illuminate a tiny area (the extreme would be a confocal illumination) or on the other hand it is not helpful to illuminate an area larger than what is imaged on the camera.

1.4 A phenomenological introduction to optical aberrations

Whenever an optical system leaves the paraxial regime, systematic image errors – called aberrations – become prominent. Usually, most of them are more or less correctable by intelligently designing the system, but of course a first step is to know what has to be accounted for. Thus, I will give an introduction – again based on the more detailed descriptions in the books mentioned in the previous section – to the different sorts of monochromatic and chromatic aberrations. We will see later, that aberrations and their control play a fundamental role in 3D localization microscopy and that these can in fact not be neglected even when most components used are highly sophisticated commercial optics.

1.4.1 Spherical aberration occurring at interfaces of imperfect shape

Spherical surfaces are theoretically not well suited for focusing lenses because they don't account for the sinus in Snell's law as a hyperbolic surface would. Nevertheless, spherical surfaces are much easier and cheaper to fabricate and thus widely used. If we now allow light, that enters the lens parallel to but far away from the optical axis, we will observe, that the focal point of different rays is a function of their distance from the optical axis. As shown in Fig. 1.9
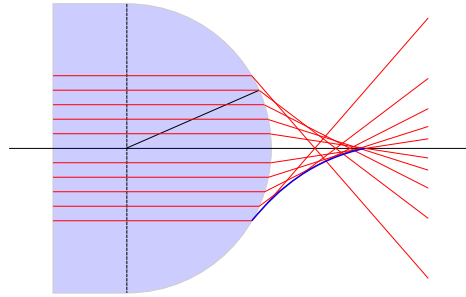
Figure 1.9: Sketch of spherical aberration with the caustic indicated in blue.

spherical converging lenses have a shorter focal length for rays far away from the optical axis than for paraxial rays. Thus, the formation of a sharp focus is inhibited. The envelope of all refracted beams is called "caustic" and is indicated by the blue line. This behavior is called longitudinal spherical aberration. If different distances to the optical axis of incident rays cause foci displaced from the optical axis (not shown), it would be a transversal spherical aberration.

Sometimes the spherical aberrations can be minimized by just using a lens according to its directionality (compare Fig. 1.10). If converging lenses or doublets with one planar surface are used, the curved surface should always be facing the parallel or less diverging / converging fraction of light. If more thorough elimination of spherical aberration is necessary, more complex multi-lens objective designs are needed, but these exceed the aim of this introduction.

(a) (b)
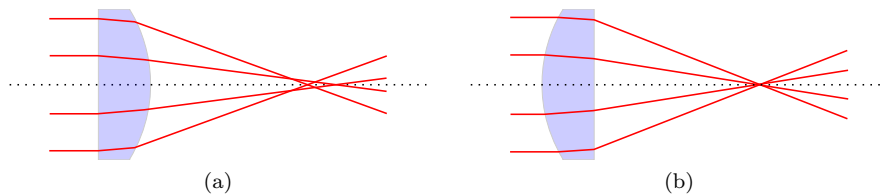
Figure 1.10: The amount of spherical aberration of a plan-convex lens is dependent on its orientation. The curved side should always be facing the parallel light for sharpest focusing as in b).

1.4.2 Coma

Coma is a phenomenon closely related to barrel distortion (subsection 1.4.5) as it originates from the fact that the magnification of a lens does not have to be constant. If the light bundles hitting the lens has an angular displacement to the

optical axis, the paraxial magnification differs from magnifications of the outer regions of the lens. This means, that even though all ray bundles emitted from a position that is not on the optical axis are focused in the same focal distance, they are not focused to the same points. The resultant PSF looks similar to a comet tail.
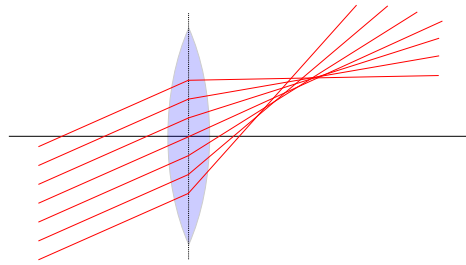
Figure 1.11: Coma can be described as a superposition of spherical– and astigmatic aberrations. As for astigmatic imaging, the angle of incidence alters the focal point, but here the spherical curvature of the lens adds to the error leading to no sharp focus but a conic PSF.

1.4.3 Astigmatism – the angle of incidence influences the focal point
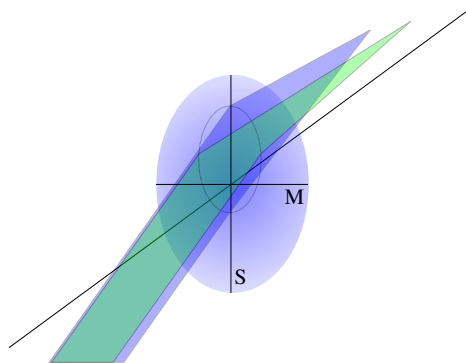
Figure 1.12: Astigmatism of a spherical lens caused by a large angle of incidence. The sagittal (S) fraction of the light encounters a differently curved surface than the meridional (M) fraction and thus both show distinct focal points.

Astigmatism is a phenomenon that may occur as an image aberration or be introduced willingly by optics that are not radially symmetric. The possibly best known occurrence of astigmatism is the stretching by a mirror that is only

curved in one direction – a children attraction on many fairs. I will deal with both astigmatism in general and the possibility to deliberately introduce astigmatism by using cylindrical– rather than spherical optics. A special example for the favorable use of cylindrical optics will be discussed in chapter 2.

If light falls on a spherical lens under a large angle as it happens in strongly magnifying optics, the angles of incidence of the meridional plane can differ from those in the sagittal plane. If that is the case, these two fractions of the incident light will focus in different points and no stigmatic – greek: point – imaging conditions are given (Fig. 1.12). The image will appear stretched in either direction depending on which focal point the sensor is placed in and there is no location for a detector, where both sagittal and meridional fractions are sharply imaged simultaneously. In fact, even a lateral displacement of both focal points may occur.
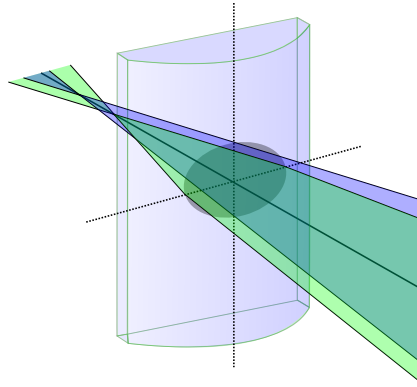
Figure 1.13: Cylindrical lenses are only curved in one direction and exhibit different focusing behavior for the meridional plane (vertical) and sagittal plane (horizontal) which are displayed in blue and green, respectively.

1.4.3.1 Special case: Cylindrical lenses

The astigmatism introduced by cylindrical lenses is easier to understand as the lens is only curved and thus focusing in one direction. The light perpendicular to that focusing direction only encounters two planar glass surfaces and thus does not get perturbed. As a result again we get two distinct focal points as in the general case mentioned above but here, it is important to realize that these focal points only show an axial shift but stay laterally on the optical axis. I have to mention that if a cylindrical lens is placed into light that is not parallel to

the optical axis, the sagittal part also exhibits a focal shift only by passing two plan parallel refractive index boundaries. Please refer to section 2.4 for further information.

1.4.4 Petzval field curvature – aperture dependence of focal distance

The term field curvature denotes the fact that if large objects are imaged, the focal length of the imaging system cannot be assumed constant and thus the focal plane is not exactly a plane but a curved surface. In other words, the further away from the optical axis a point is, the shorter will be the focal length where we find its image. If we put a planar sensor in the paraxial image distance, the image will be sharp in the center but blurred in the outer regions.
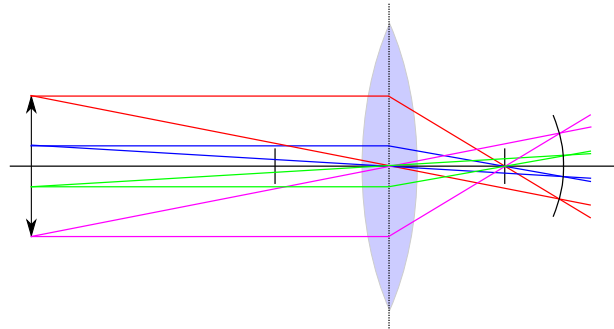
Figure 1.14: For big apertures, the image distance cannot be considered constant. This results in a curved image as described by Petzval.

1.4.5 Barrel– and pincushion distortions – non-uniformity of image magnification

Barrel– and pincushion distortions (abbreviated distortions in this part) on the other hand are often mixed up with field curvature but are nevertheless a different phenomenon. These distortions are named after the shape, the respective image resembles. In an optical system where only these distortions are present, the image is sharp on the whole detector and at any point on the detector, the same object plane is imaged. That is, in contrast to field curvature the focal length is constant. But the image will appear stretched (usually radially) because the *magnification* of the imaging system without special corrections is a function of the distance of an object point from the optical axis. In plain words: While
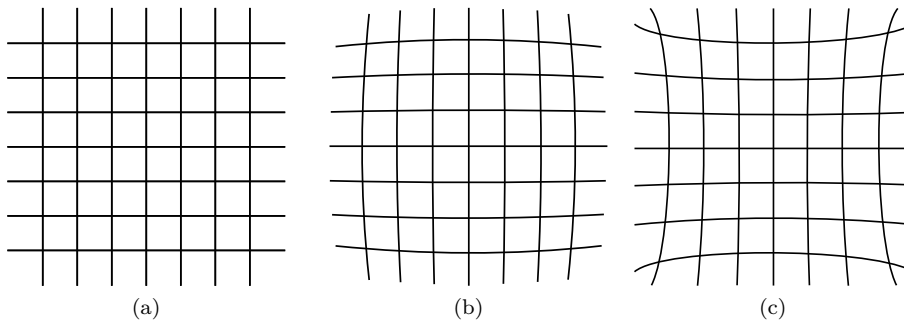
Figure 1.15: The magnification of an optical system may be a function of the distance to the optical axis. a) depicts an image of a raster with perfectly uniform magnification, while b) and c) show distortions that are – according to their shape – named barell– and pincushion distortion, respectively.

paraxial objects are nominally magnified, non paraxial points can exhibit higher– or lower magnification (pincushion or barrel, respectively) (cf. Fig 1.15).

1.4.6 Chromatic aberration

While all other aberrations discussed so far are monochromatic phenomena, another error occurs with simple lenses for light of more than one color. As shown schematically in Fig. 1.16a, the focal length of a simple lens is not constant for different wavelengths, i.e., blue light shows a shorter focal length than green and finally red. The underlying mechanism is that the refractive index of optical media varies with the wavelength – an aspect coined dispersion of the material.
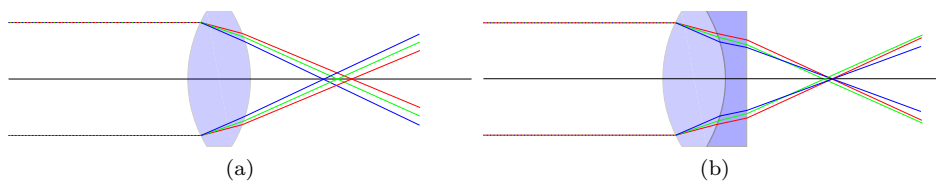
Figure 1.16: Single lens with chromatic aberration a) and doublet of lenses b) with different refractive indices (light blue: crown glass, dark blue: flint glass) correcting red and blue light. Apochromatic correction would at least need three lenses.

Of course it is usually beneficial to correct for these focal shifts as many optical measurements incorporate several colors. As depicted in Fig. 1.16b this can

partially be achieved by adding a second lens with refractive index n_2 (flint glass) to the initial lens with n_1 (crown glass). This assembly is usually pre-aligned and in many cases (but not necessarily) the two lenses are glued together. This construct accounts for the focal difference of red and blue light and is called *achromatic* lens. For any further correction, additional lenses would be needed. Accordingly, it is feasible to focus blue, red and green light to the same spot by introducing a third lens, which would be called an *apochromatic* lens. The higher the needed degree of correction for chromatic aberration, the more complex the design becomes and apochromatic correction is usually sufficient and thus widely used in high-end-optics.

2 Decoding the third dimension

In this chapter I aim to focus on how to deal with emitters, that are situated slightly above ($+z$) or below ($-z$) the plane of sharpest imaging ($z = 0$) that thus show a de-focused PSF. The major problem here is, that the PSF is axially symmetric (if no aberrations are apparent) and thus without further input, it would be possible to tell how far away from $z = 0$ the emission took place but not whether it was in the plus– or minus direction. I will first explain strategies to infer z-coordinates by breaking the axial symmetry and then outline how to calibrate and evaluate 3D measurements using the rapid, accurate program implementing direct stochastic optical reconstruction microscopy (rapi*d*STORM) 3.3.1 that was developed by Steve Wolter (Wolter et al., 2012a). I will thereafter highlight the most common aberrations frequently encountered in 3D (localization) microscopy, present some examples of successful 3D imaging and finally I will put some emphasis on 3D experiments with two-colors.

2.1 Different techniques for engineering the PSF

In the past years, quite a few methods have been proposed to break the axial symmetry of a PSF in order to enable 3D measurements. Not surprisingly, some approaches were not originally proposed for localization microscopy but for example they were employed in single particle tracking (Kao and Verkman, 1994; Holtzer et al., 2007). Nevertheless, they experienced a renaissance with the invention of single-molecule localization microscopy and they can roughly be split into four groups:

1. interferometry

2. lobe-splitting

3. biplane

4. astigmatism

The interferometric approach is by far the most challenging in the assembly of the microscope which is one reason why it was not considered for implementa-

tion during the work on my thesis. Nevertheless, it should be mentioned not only because of its unprecedented precision in z. In interferometric PALM (iPALM) as published by (Kanchanawong et al., 2010; Shtengel et al., 2009) the specimen is placed between two objectives each collecting light from one of the two half-spheres of the molecule's isotropic emission. These two detection paths are combined via a three-way beam splitter and exploiting the wave-particle duality, each photon is brought to interference with itself. The axial position of the fluorophore, i.e., whether it is closer to objective A or B gives distinct interference patterns and thus the z-coordinate can be extracted. While yielding axial resolutions of the order of 10 nm, interferometry is restricted to an axial range of about half of the emission wavelength. Because the final aim of this thesis was to enable 3D microscopy of up to hundreds of micrometers in z, this is another reason why I decided that interferometry would not be the method of choice.

The group of lobe-splitting approaches on the other hand introduces optical elements to the detection path that slit a PSF into two lobes that rotate around each other with respect to z. The originally proposed double-helix PSF (Pavani et al., 2009) made use of a polarization-sensitive spatial light modulator that serves as a phase mask. The resultant lobes rotate around each other. Even though very similar but simpler to build is the phase ramp imaging localisation microscopy (PRILM) technique (Baddeley et al., 2011) that uses a nearly plan parallel piece of glass in half of the parallel light path below the objective. The result are again two lobes but here, one stays stationary while the other rotates around the first. This latter approach was adopted by Zeiss with their Elyra localization microscope system partly because of its supposedly longer axial range that in theory stems from effectively reducing the detection NA of the objective for each lobe to one half of the full aperture. Both techniques have not been used throughout this thesis, because fitting to an experimental PSF is not supported by rapi*d*STORM 3.3.1.

Another way to break the PSF symmetry is a method called biplane imaging (Juette et al., 2008). The trick is to image two planes of the specimen simultaneously with one being some hundreds of nanometers out of focus in known axial direction. Comparing the sharpness of the corresponding PSFs, i.e., their size on both planes, the z-coordinate can be extracted. A big advantage of this technique is that the Gaussian approximation of the PSF holds for a considerable axial range and thus the evaluation with existing software (rapi*d*STORM) is straightforward but the drawback is the need to image two planes. That can either be achieved by splitting one detector in half which would reduce the imag-

ing area or by introducing a second camera which is not cost-efficient. From a computational point of view the complexity of biplane and astigmatism should be comparable.

Finally, astigmatism is the fourth technique and the one chosen in this thesis because of its experimental easiness and cost-efficiency. This method was initially used in single particle tracking (Kao and Verkman, 1994; Holtzer et al., 2007) but has later been applied to localization microscopy in a variety of publications (Dani et al., 2010; Huang et al., 2008a; Xu et al., 2012). Here, a cylindrical lens is introduced into the detection path of the microscope which serves as an extra focusing element in only one direction. The resulting PSFs are either sharply imaged in x– or y-direction while extended in the respective other depending on the axial location of the fluorophore. As sketched in Fig. 2.1 there exists an image plane where both dimensions are equally de-focused. That image plane can arbitrarily be set to $z = 0$ and PSFs from higher image planes are stretched vertically while those from lower planes are stretched horizontally (or vice versa depending on the orientation of the lens). Again, a Gaussian approximation holds for comparable axial ranges as in biplane imaging if the standard deviations in x and y are treated independently. All experiments described in the following were conducted using astigmatic 3D imaging.
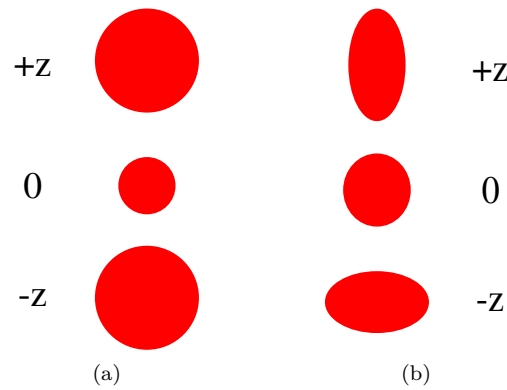
Figure 2.1: a) resembles a sketch of the symmetric defocusing behavior of an objective while b) sketches defocusing with broken symmetry achieved with astigmatic PSF-engineering by insertion of a cylindrical lens to the detection path.

2.2 Evaluating 3D measurements with rapi*d*STORM 3.3.1

A crucial step in 3D imaging is the calibration of the defocusing behavior of single emitters. For simulating the PSF of organic fluorophores, fluorescent particles of an average size of 100 nm (TetraSpeck, T-7279, life technologies) were immobilized either on a cover slip surface or in a statistical manner in 3D in a hydrogel with a refractive index of about 1.34 which is close to water ($n = 1.33$). For a detailed description please refer to sections 5.1 and 5.2.

Different calibrations have already been proposed:

1. fitting the standard deviations σ in x and y independently, subtracting σ_x from σ_y and thereby generating a sigma-difference lookup table for the extraction of the z-coordinate (Henriques et al., 2010)

2. fitting the PSF to a physically derived polynomial of second order (Eq. (2.1)) (Holtzer et al., 2007)

3. fitting to a polynomial of up to fourth order to better deal with imperfections in the optical system (Eq. (2.2)) (Huang et al., 2008b)

The sigma-difference method (1) was first assessed because of its relative simplicity but it turned out, that fitting the standard deviations independently and then looking up the closest match for a z-coordinate in the $\sigma_{x,y}$-space introduces an unphysical degree of freedom. It was already shown before for 2D that more degrees of freedom than needed lead to a loss in precision (Wolter, 2009) and indeed the respective data for a bright emitter in Fig. 2.3 supports that notion.

$$\sigma_{(x,y)}^2 = \sigma_{0,(x,y)}^2 + a_{(x,y)}(z - z_{0,(x,y)})^2 \tag{2.1}$$

$$\sigma_{(x,y)}^2 = \sigma_{0,(x,y)}^2 \left(1 + \sum_{i=1}^{4} \left(\frac{z - z_{0,(x,y)}}{\Delta\sigma_{i,(x,y)})^i}\right)^i\right) \tag{2.2}$$

Because of the unsatisfying localization precision encountered with the sigma-difference routine the other already proposed methods were as well assessed. The approaches 2 and 3 will in the following be grouped to polynomial methods as any finding applies to both. They both lack from the circumstance, that all fit parameters have global impact what makes it difficult to deal with calibration data which is not axially symmetric as it occurs in the case of spherical aberrations. Figure 2.2 a) gives exemplary data for such a case of axial asymmetry that
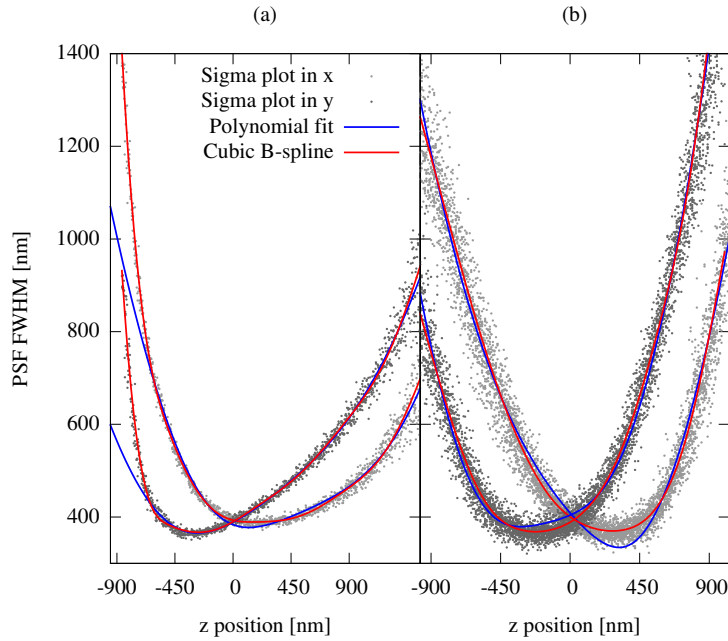
Figure 2.2: Typical sigma plots as obtained with a) oil-immersion objectives or b) water-immersion objectives. a) shows localizations of a single TetraSpeck, and b) shows a superposition of 27 TetraSpecks. Sample 1 and 2 in Fig. 2.3 were evaluated with the splines shown in a) and b), respectively. Note the strong axial asymmetry in a), which originates from the different refractive indices of oil and water at the glass-specimen-interface. Both samples show the typical oscillation behavior of the polynomial fits around the better-fitting cubic B-splines. Graphic and caption reproduced from (Proppert et al., 2014) with kind permission of The Optical Society.

occurred, because imaging was performed with an oil-immersion objective in an aqueous sample (please refer to section 2.3 for further information). Here, it was difficult to find an axial range that yielded reasonable fit results because either the steep slope to the left or the shallow one to the right were overemphasized if the range was not set appropriately. The fit results are the coefficients for the respective terms in the polynomial that would later be used for the evaluation of a measurement that is to be calibrated. Steve Wolter and I tried to improve the results by making the fit subject to Nelder-Mead optimization (Nelder and Mead, 1965) using the implementation in the GNU scientific library (Galassi et al., 2003) which also needs considerable expert knowledge because there is

no heuristic for finding the initial simplex. Nelder-Mead optimization did not show significant changes in the localization precision and axial range and was thus omitted in the further work. The finding, that a lot of expert knowledge is needed for a successful evaluation with the polynomial model led to the notion that it should be advantageous to find easier methods – especially as this thesis also had an emphasis on making 3D localization microscopy as robust and reliable as possible.
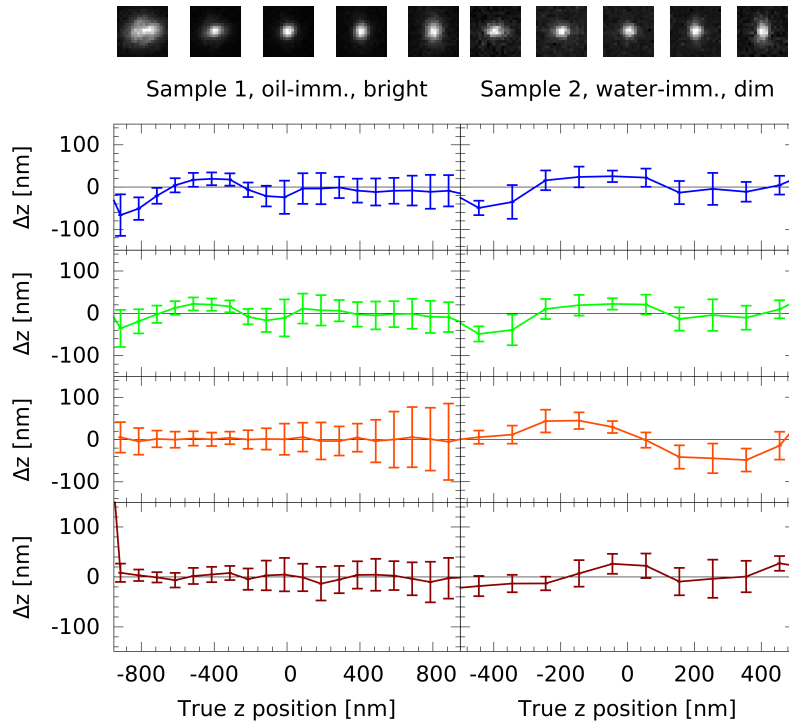
Figure 2.3: Axial localization performance of different fit routines. The figure shows data for two samples. The PSF snapshots (top of figure) were taken from the data presented and correspond to the z-position indicated on the abscissa. Sample 1 is a bright microsphere imaged with oil immersion, and Sample 2 is an emitter with fluorophore-like photon yield in water immersion. In Sample 1, the same bead was used for calibration and testing. In Sample 2, one bead was calibrated, and a different bead from the same acquisition tested. In each subplot, the fitted z position was plotted against the z ground-truth extracted from the piezo movement, and data within 100 nm intervals was averaged. Graphic and caption reproduced from (Proppert et al., 2014) with kind permission of The Optical Society.

The overall complexity and uncertainties of the polynomial method led to Steve Wolter's idea that if the physically derived model does not hold well anyway (e.g., due to aberrations), there is also no need to fit data to an arbitrary model. Instead, he proposed to fit the data with cubic B-splines which has the two major advantages that it is a well described and tested interpolation method known for decades from image analysis and the impact of some false interpolations would not be global as in the polynomial case but have only local influence. He decided to take the GNU scientific library implementation of cubic B-splines to model the data. The PSF widths obtained by fitting to a Gaussian was evaluated with ten knots and the obtained knot coordinates (z and σ) were stored in a file which can then later be used to infer the z coordinate to a measurement by expressing $\sigma_{x,y}$ as a function of z ($\sigma_{x,y} = \sigma_{x,y}(z)$).

It turns out that the evaluation with cubic B-splines combines both the precision of the polynomial model and the accuracy of the sigma-difference method. We reason, that the precision stems from the explicit modeling of the z-coordinate in the PSF model as in the polynomial model. The accuracy can be denoted to the model-free description of the relationship between the shape of the PSF and the respective z-coordinate, like in the sigma-difference method. B-Splines further benefit from the fact, that – in contrast to the polynomial method – any erroneous interpolation do only have local impact. The thereby enabled ability to account for axial asymmetry of the PSF as encountered in the case of refractive index mismatch, especially renders the interpolation with cubic B-splines superior to other techniques.

For a final judgment of the performance of the respective approaches we introduced an arbitrary scale on which the complexity and the error-proneness of a method is judged (cf. Fig. 2.4). The final score of a method was then related to the obtained localization error (Fig. 2.4) and the central finding is that cubic B-splines render the best trade-off between simplicity / robustness and localization error. Due to the aforementioned results, I only used the interpolation with cubic B-splines during the course of my thesis and will give some mathematical background in the following section.

Method	Parameter	Reasoning	Score
Nelder-Mead	Initial simplex	No heuristic, manual intervention needed, long feedback time	5
Polynomial	Fit region	Too large and too small fit region can be within $\pm$ 200 nm	4
cubic B-spline	Fit region	Accidentally included bad points have only local influence	1
cubic B-spline	Number of knots	1 knot per 150 nm worked for all our measurements	1
Sigma-difference	Smoothing factor	Factor depends on rate of σ change and method is robust to errors	1
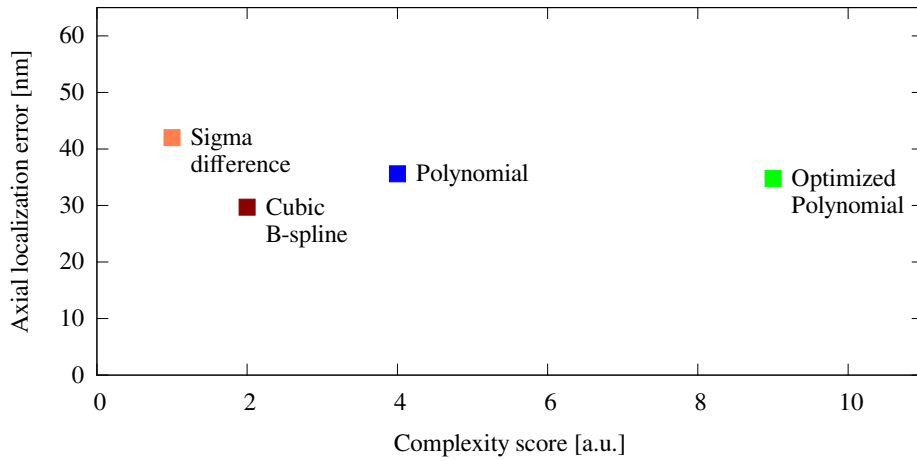
Figure 2.4: Comparison of complexity and axial localization error for the 3D inference methods. The complexity is given comparatively in arbitrary units, determined from a difficulty ranking of the steps in each procedure. We judged user-visible complexity as steps that have a high likelihood of error or require manual intervention. The values were chosen on a relative scale according to our experience with the methods' application during the preparation of this article. The axial localization error, given as the RMSD of localizations from the z ground truth, characterizes the precision achievable with the method. The cubic B-spline method combines the good precision of the polynomial method with the simpleness of the sigma-difference calibration. Graphic, table and caption reproduced from (Proppert et al., 2014) with kind permission of The Optical Society.

2.2.1 Interpolation of the PSF-shape using cubic B-splines

2.2.1.1 Theoretical background for cubic B-spline evaluation

Even though I was told that the implementation in rapi*d*STORM was straightforward (by the use of existing methods and classes) at least to me the underlying mechanisms were not trivial and thus I will describe them for the interested reader. The description of the evaluation with cubic B-splines is adapted from a part I wrote of the rapi*d*STORM manual (Wolter et al., 2012b).
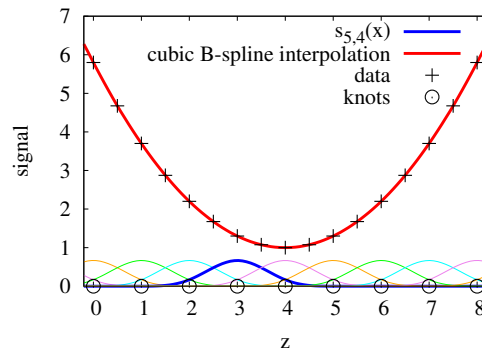
Figure 2.5: This diagram (arbitrary units) aims to visualize exemplarily how to handle data with cubic B-spline interpolation. The black crosses represent seventeen given data points while the rainbow-colored pseudo-Gaussians at the bottom of the diagram are plots of the B-spline basis functions $s_{i,4}(x)$ $(i = 0, 1, \ldots, 11)$ with the $n = 9$ knots indicated by black circles. Evaluation of Eq. (2.7) leads to amplitude factors for each basis function. The superposition with given amplitudes results in the interpolation represented by the red parabola. Graphic and parts of the caption reproduced from (Proppert et al., 2014) with kind permission of The Optical Society.

Definition of B-spline basis functions. Consider a given data set of m points $y_0(x_0)$, $y_1(x_1)$, $\ldots$, $y_m(x_m)$ on an interval $[L_1 : L_2]$ (black crosses in Fig. 2.5). In order to perform the interpolation, first that interval is split into segments represented by n equidistant knots t_i $(i = 0, 1, \ldots, n-1)$ marked as black circles. As implemented in the GNU Scientific Library for B-spline interpolation, the $n + 2$ basis functions $s_i(x)$ of order k are segmentwise recursively

defined following equations (2.3) and (2.4). For cubic B-splines, k goes from 1 to 4.

$$s_{i,1}(x) = \begin{cases} 1 & : t_i \leq x < t_{i+1} \\ 0 & : else \end{cases} \tag{2.3}$$

$$s_{i,k}(x) = \frac{x - t_i}{t_{i+k-1} - t_i} s_{i,k-1}(x) + \frac{t_{i+k} - x}{t_{i+k} - t_{i+1}} s_{i+1,k-1}(x) \tag{2.4}$$

Interpolation and least squares fitting (LSF) as implemented in rapi*d*-**STORM 3.3.1.** The interpolation to the data set is computed as in Eq. (2.5) and represents a set of linear equations with $\vec{y} = (y_0(x_0),\, y_1(x_1),\, \ldots,\, y_m(x_m))$ and $\vec{c} = (c_0,\, c_1,\, \ldots,\, c_n,\, c_{n+1},\, c_{n+2})$.
Matrix notation (Eq. (2.6)) indicates, that S is of diagonal form.

$$y_m(x_m) = \sum_i s_{i,k}(x_m) c_i$$

$$\vec{y} = S \cdot \vec{c} \tag{2.5}$$

$$S = \begin{pmatrix} s_0(x_0) & s_1(x_0) & s_2(x_0) & 0 & 0 & \cdots & 0 \\ s_0(x_1) & s_1(x_1) & s_2(x_1) & s_3(x_1) & 0 & \cdots & 0 \\ 0 & s_1(x_2) & s_2(x_2) & s_3(x_2) & 0 & \cdots & 0 \\ 0 & s_1(x_3) & s_2(x_3) & s_3(x_3) & s_4(x_3) & \cdots & 0 \\ \vdots & \vdots & \ddots & \ddots & \ddots & \ddots & \vdots \\ 0 & 0 & 0 & s_{n-1}(x_{m-1}) & s_n(x_{m-1}) & s_{n+1}(x_{m-1}) & s_{n+2}(x_{m-1}) \\ 0 & 0 & 0 & 0 & s_n(x_m) & s_{n+1}(x_m) & s_{n+2}(x_m) \end{pmatrix} \tag{2.6}$$

In equation (2.5) the vector $\vec{c}$ is unknown and object to least squares fitting, which is performed following Eq. (2.7).

$$\vec{c} = (S^T \cdot S)^{-1} \cdot S^T \cdot \vec{y} \tag{2.7}$$

Derivation of the formula for LSF (Eq. (2.7)). The fit residuals are defined as: $\vec{r}(\vec{c}) = \vec{y} - S \cdot \vec{c}$ with the i-th component of r being:

$$r_i(c_j) = y_i - \sum_j S_{ij} \cdot c_j.$$

The least squares fitting criteria is fulfilled when

$$\left|\vec{r}(\vec{c})^2\right| = \min \Leftrightarrow \frac{\partial \vec{r}(\vec{c})^2}{\partial \vec{c}} = 0 \qquad . \tag{2.8}$$

Evaluation of the right side of Eq. (2.8) for r_i gives

$$0 = \sum_i \frac{\partial \left(r_i(c_j)^2\right)}{\partial c_j} = \sum_i \frac{\partial r_i(c_j)}{\partial c_j} \cdot 2r_i(c_j)$$

$$= \sum_i -S_{ij} \cdot 2r_i(c_j) = \sum_i S_{ij} \cdot \left[y_i - \sum_k S_{ik} \cdot c_k\right]$$

$$= \sum_i S_{ij} \cdot y_i - \sum_i S_{ij} \cdot \sum_k S_{ik} \cdot c_k$$

$$\sum_i S_{ij} \cdot y_j = \sum_k \left[\sum_i S_{ij} \cdot S_{ik}\right] \cdot c_k$$

$$\sum_i S_{ji}^T \cdot y_i = \sum_k \left[\sum_i S_{ji}^T \cdot S_{ik}\right] \cdot c_k$$

$$= \sum_k \left(S^T \cdot S\right)_{jk} \cdot c_k$$

$$\left(S^T \cdot \vec{y}\right)_j = \left[\left(S^T \cdot S\right)\vec{c}\right]_j \tag{2.9}$$

which, rewritten in vector notation leads to the form of Eq. (2.7):

$$S^T \vec{y} = \left(S^T \cdot S\right)\vec{c}$$

$$\Leftrightarrow \left(S^T \cdot S\right)^{-1} S^T \vec{y} = \mathbb{1}\vec{c} \qquad . \tag{2.10}$$

2.2.2 Often encountered image errors

The quality of a 3D measurement is never to be trusted without taking a sharp look at the result. It occurred quite frequently that structures were localized multiple times to different and very discrete z planes. This especially occurs if the sample taken for calibration does not fit to the specimen that is to be measured or a calibration was taken with another objective.

The following two scenarios are crucial to avoid:

1. Measurement with water-immersion while calibration was performed with oil-immersion

2. Use of a calibration sample with unknown or wrong refractive index

While the first is usually a simple mistake of users that are not yet acquainted with the microscope and that can easily be corrected by taking the right calibration file, the second one is a bit trickier. For scientists that are new to the fundamentals of optical imaging, it is not trivial to take the refractive index of a specimen into account. Most simply speaking: **The calibration has to fit to the experiment.** Thus, if for example imaging is performed in intact cells this might have implications to the calibration process, because cells usually exhibit refractive indices of about 1.4. Therefor at least it has to be checked thoroughly if a calibration in water is suited or if the refractive index must be matched first.

Another reason for such image errors can be that the fluorophores are not bright enough. It seems like rapi*d*STORM's fit algorithm has some preferred axial planes if the signal-to-noise ratio (SNR) is low. In this case, the experimentalist is admonished to increase the photon budget as much as possible for example by changing the buffer composition or using different dyes. If that is not possible, for example because two-color experiments are performed and there simply is no single ideal imaging buffer for both fluorophores, the responsible researcher at least has to have understood that this layering or even mirroring is physically not correct and that he may have to restrict the axial fit interval to a range that might be a lot narrower than desired but at least gives reasonable results.

Even though the aforementioned might seem obvious, I cannot emphasize enough the need for having a sharp and honest look at x, y-z-cross-sections because these errors are not apparent in 2D localization microscopy (so even experienced localization microscopists are usually not familiar with them) and any mistake here might lead to false conclusions.

2.3 Aberrations induced by refractive index mismatch

While 2D localization microscopy needs the determination of the center of a PSF, in 3D localization microscopy also the shape of the PSF of a single molecule becomes an important factor as it encodes the axial location. In order to perform

reproducible and precise 3D microscopy, it is thus mandatory to understand possible aberrations, avoid or minimize them, or at least deal with them accordingly. I will show in the following sections (sections 2.3 - 2.4), that the two different immersion regimes – oil-immersion with mismatched specimen buffer, or index matching by using water-immersion – both show distinct disadvantages on inverted microscopes. Please note, that the respective aberrations are no intrinsic property of the different kinds of objectives but of the circumstance whether or not the refractive index is matched.

2.3.1 Depth scaling-factor
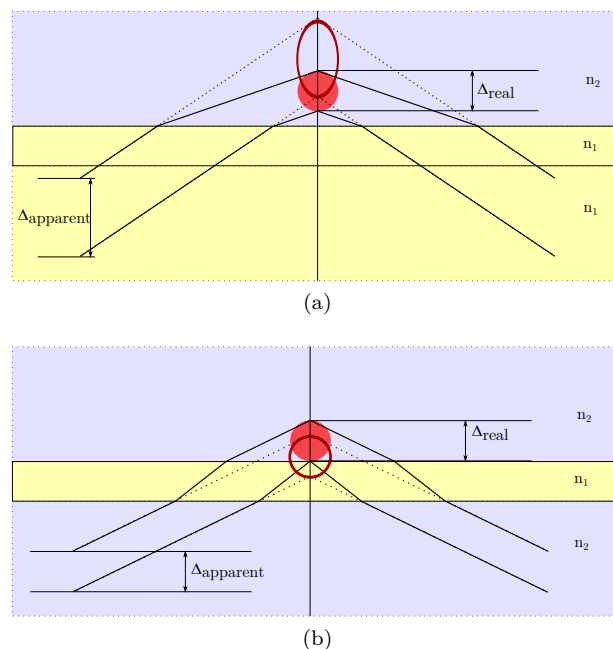
Figure 2.6: Image stretching because of refractive index mismatch. a) shows that if the refractive indices are not matched – imaging with oil-immersion in water – the axial distance Δ_{real} that is covered by the objective movement is smaller than the nominal distance the objective moved ($\Delta_{\mathrm{apparent}}$). Thus, if the nominal movement is used when reconstructing an image, the image will appear stretched. b) on the other hand indicates that for matched immersion media, the shape of the object is preserved. The worst that can happen is that the absolute location of the image is off the real location, if that shift was not corrected for by optics or software (adding a constant value).

With the triumph of CLSM the impact of optical aberrations on quantitative image acquisition became of interest. In one of the first papers (Hell et al., 1993) the deviations of the confocal PSF from a perfect PSF was calculated and it was found that upon imaging with an oil-immersion objective in aqueous samples, the image will appear stretched by a factor of 1.2 due to the refraction occurring at the refractive index interface. Fig. 2.6 sketches with ray optics that the axial distance Δ_{real} covered by the objective movement is smaller than the nominal distance the objective moved ($\Delta_{\mathrm{apparent}}$).

This notion is supported by a variety of other papers (Diaspro et al., 2002; Huang et al., 2008a; Biteen et al., 2012) written in the following decade with slightly different but overall consistent findings about the stretching factor. In (Sheppard and Török, 1997) the authors investigated the stretching factor as a function of the imaging depth and found that at imaging depths above 30 µm the stretching factor can be well approximated by the geometrically derived factor for oil-immersion imaging of aqueous samples $f_{stretch}$ (Eq. (2.11)) while it is slightly higher and consistent with (Hell et al., 1993) closer to the cover slip.

$$f_{stretch} = \frac{n_{immersion}}{n_{specimen}} \approx \frac{1.52}{1.33} \approx 1.14 \qquad (2.11)$$

It would thus lead to an error of about 20% if the apparent height was taken as the z-coordinate in the sample when imaging with oil immersion in water. There are three strategies to account for this error:

1. Rescale by the factor $f_{stretch}$. This is recommendable because of its ease of use for single measurements close to the cover slip.

2. If the specimen is permeable for the mounting medium, the refractive index of the mounting medium can be adjusted to match the immersion medium. However, this is not applicable for live-cell experiments and also tissues or tissue section usually show not adjustable refractive indices of ≈ 1.4.

3. Especially in localization microscopy it may be cumbersome to adjust the refractive index of the specimen accordingly, because the switching mechanism strongly relies on the chemical composition of the mounting medium. In this case, if there are no counter-indications, the safest choice would be to employ an objective that uses an immersion medium that matches the specimen in its refractive index. Water immersion should be used for fixed and permeable samples in aqueous environment or glycerol immersion for tissues.

2.3.2 Imaging depth dependent spherical aberration

Another problem arising when imaging with non-matched refractive indices is similar to the phenomenon of spherical aberration which was previously discussed in section 1.4.1. Usually, spherical aberration describes the fact that the focal length of an imaging system without special correction is dependent on the distance of the incident rays from the optical axis. With refractive index mismatch, quite similarly, the focal length is dependent on the angle of incident as calculated and depicted in Fig. 2.7 and Fig. 2.8 (the latter showing the case without aberration for comparison). While rays imaged under an acute angle deviate little from the nominal focal length of the objective, the respective focal length for big angles of incidence becomes significantly smaller. This leads to a disturbance of the focus similar to that in case of spherical aberration.
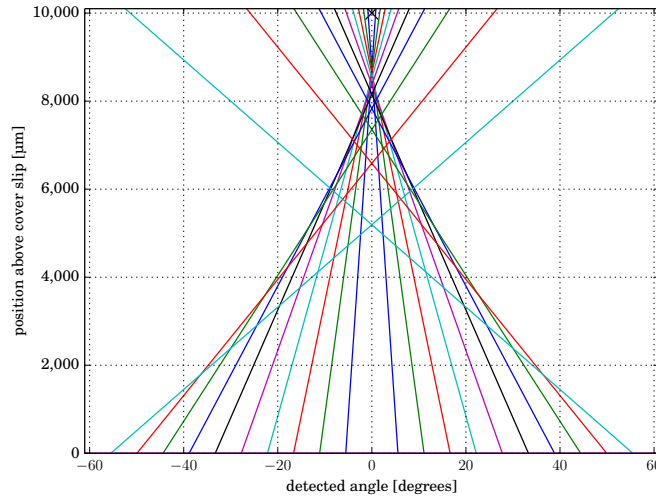
Figure 2.7: This figure depicts the spherical aberration due to focusing with an oil-immersion objective in aqueous samples. The slope of the respective rays becomes a function of their angle of incidence and only form a blurred, y-shaped area of least obstruction. The black cross indicates the nominal focus of a matched imaging system (as discussed in Sec. 2.3.1).

Furthermore, the angle under which a fluorophore can be imaged is a function of the axial position z. While the objective can use its full NA for fluorophores at $z = 0$, the further inside the specimen, the more acute is the maximum angle of incidence (cf. Fig. 2.9). Here, we must keep in mind that the full NA of an oil
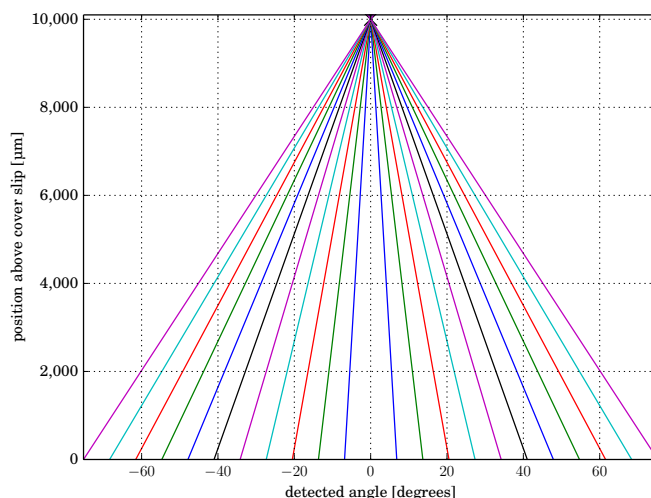
Figure 2.8: This figure indicates the geometrical approximation of the shape of a PSF when imaging with matched refractive indices. All rays combine in the same point neither any deviations from a sharp focus in form or location are apparent.

immersion objective is not the specified NA of, e.g, 1.45 but always at maximum 1.33 because any light imaged under a steeper angle will be totally reflected.

This decrease in NA does not mean, that the light collection efficiency of the objective is perturbed by the refractive index boundary. The light is only imaged under a more acute angle and thus, the PSF becomes wider laterally and longer in the axial directions.

If we now put this all together, we will realize, that the shape of a fluorophore's PSF must be a function of its axial coordinate. In fact it was already stated in 1993 (Hell et al., 1993) for confocal microscopes that the detected brightness of an emitter 20 µm above the cover slip is already decreased by 40 % compared to the brightness of an emitter imaged at $z = 10$ µm. To understand this, we must recap that – in order to minimize out of focus light – a confocal microscope employs a pinhole in front of the detector which is matched in size to the PSF. When it is matched to a PSF with hardly any perturbations (0 µm above cover slip), the PSF of a higher positioned emitter will not fit through the pinhole anymore and signal will be shadowed and thus not be detected. While localization microscopy is a widefield technique and thus does not employ pinholes in the detection this change in shape is nevertheless important because obviously the previously
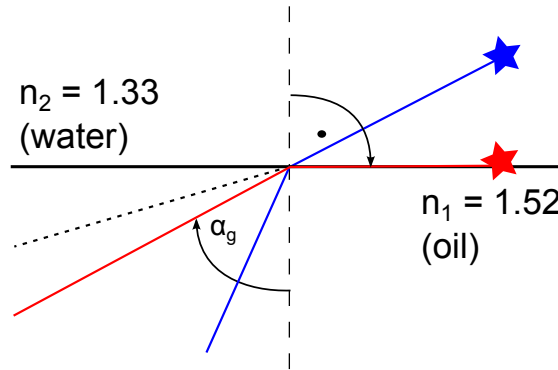
Figure 2.9: In the case of refractive index mismatch, a fluorophore far away from the cover slip is imaged under a much more acute angle than a fluorophore at $z = 0$. Thus, the PSF will broaden laterally and elongate axially as a function of z. Dashed: detection angle for NA = 1.45, red: maximum detection angle (α_g) when imaging with oil immersion in aqueous environments (for a fluorophore in close vicinity to the cover slip, resulting $\mathrm{NA_{max}} = 1.33$), blue: exemplary rays for an emitter which is far away from the surface.

conducted calibration will not fit to the data anymore or in other words: In the presence of refractive index mismatch, there has to be precise knowledge about the depth at which imaging is conducted as the system has to be calibrated accordingly. Any significant deviation from the calibrated imaging depth will result in false localizations.

The elongation of the PSF as a function of z is depicted in Fig. 2.10. Figures 2.10a and 2.10b show measured x-z-profiles of the PSFs of 100 nm TetraSpeck beads statistically deposited in Matrigel (refractive index of about 1.34, dependent on batch) and illuminated with 640 nm laser irradiation at $z = 0$ nm (2.10a, the lowest bead found in the specimen) and $z \approx 30$ µm above the cover slip. It is directly apparent that at deeper imaging depths, the PSF deviates significantly from a Gaussian focus and looks more like a Besselian PSF. Accordingly, Figures 2.10c and 2.10d depict the respective PSFs in the absence of refractive mismatch (measurements were performed with a water-immersion objective in aqueous environment). This deviation from a perfectly Gaussian shape originates from the fact that the cylindrical lens was in the detection path at all times in order to obtain realistic x-z-profiles as they would be encountered in a 3D localization microscopy experiment.
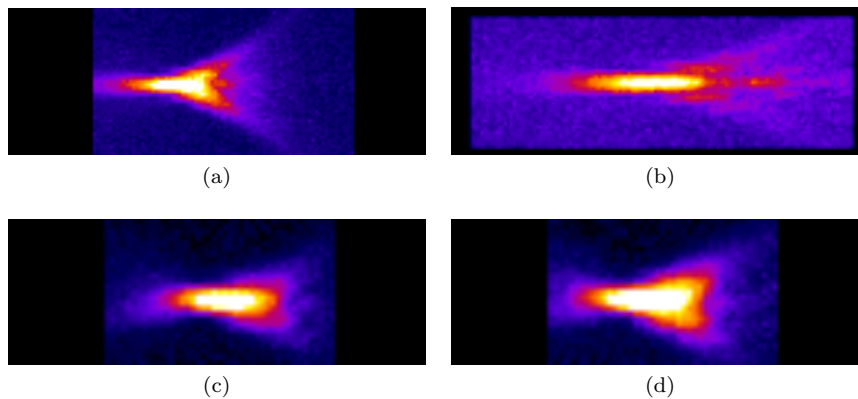
Figure 2.10: Measured PSFs with refractive index mismatch (a) and b)) and without (c) and d)). a) and c) show the x-z-profile of a 100 nm TetraSpeck bead at the cover slip surface, b) and d) corresponds to a bead about 30 µm above the cover slip. Beads were immobilized in Matrigel with an approximate refractive index of 1.34 and observed with an oil immersion – (a) and b)) or water immersion (c) and d)) objective. The refractive index mismatched of ≈ 0.01 in c) and d) is handled as close enough to zero as not to lead to significant image deformations.

The overall shape is nevertheless quite consistent with long-known findings for calculated PSFs of a confocal microscope (Fig. 2.11). By taking a closer look to either the calculated PSFs known from literature or the measured ones, it becomes apparent that the deviations between the respective PSFs at a cover slip or deep inside the specimen is not symmetric. As typical for a spherical aberration, below the point of sharpest focus (right sides in Figures 2.10a and 2.10b) the PSF deviates less from its ideal shape than above. This explains why (Deng and Shaevitz, 2009) and (Huang et al., 2008b, supporting information) found independently that the localization accuracy is not axially symmetric. If for example calibration took place 0.5 µm above the cover slip, all localizations in a subsequent experiment stemming from between 0 nm and 500 nm will be fitted with reasonable accuracy to the right location while localizations stemming from higher focal planes will be systematically fitted to a wrong position. The simple explanation is that due to little deviations below the point of sharpest focus, the data still more or less fits to the calibration, while the defocusing behavior above the point of sharpest focus cannot be modeled by the calibration which took place at another height and thus does not suit to calibrate the experiment.

Confocal Point Spread Function Contour Plots
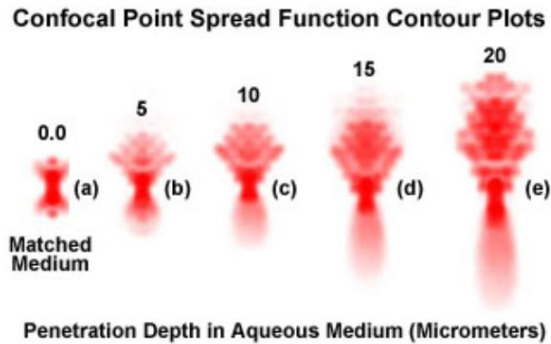
Figure 2.11: Confocal PSFs versus imaging depth (Brenner et al., 2014). a) depicts the PSF for a sample matched to the immersion medium, while b)-g) depict the theoretical PSFs in the case of non-matched media with varying imaging depth (indicated on top of each subfigure in micrometer).

It is now interesting to estimate until which imaging depth it is valid to use oil-immersion objectives – no matter whether due to their higher light collection efficiency, lower cost or the simple fact that they are available in most labs anyway while water immersion objectives are rarer. An estimate from literature is given by (Deng and Shaevitz, 2009) who performed measurements in heights between 0 µm and 3 µm above the cover slip and already found false localizations of up to 30%. To get an own estimate, I again imaged 100 nm TetraSpecks immobilized in Matrigel with an oil-immersion objective (Figures 2.12 and 2.13) and scanned the objective during the experiment from 0 µm to 50 µm (objective movement). As a result different beads will move through the focal plane throughout the experiments and after localization with a calibration file extracted from the lowest bead and subsequent subtraction of the known objective movement, the resultant beads should be imaged as sharp dots if no aberrations were apparent. This is not the case and in both measurements we see a significant gradient in axial localization accuracy. While the lowest beads show the expected point-like localization, the localizations of beads placed higher in the specimen stretch to several micrometers. As shown in Fig. 2.13a these traces seem to stretch in only one direction and then stop abruptly as predicted by (Deng and Shaevitz, 2009) and (Huang et al., 2008b).

The localizations in Figures 2.12b and 2.12c are outlined because the bead in Fig. 2.12c already appears significantly stretched while the respective bead in Fig. 2.12b still shows a quite accurate localization even though their axial

location is nearly equal. It is hard to give an absolute quantity from these measurements, but we can estimate that 10 µm is an upper bound for successful imaging with oil-immersion in aqueous samples.

For comparison I conducted the same experiment in the same sample with a water-immersion objective. The result is summarized in Fig. 2.14. In good agreement with theory – no significant aberration should be apparent –, the same calibration holds over the whole axial range. It is thus strongly recommended to use refractive index matching for imaging of big volumes or if the exact height of the specimen is unknown.

So, why are most 3D localization experiments conducted using oil-immersion objectives? On the one hand, water-immersion objectives are rare in most laboratories while oil-immersion objectives are standard and on the other hand, many localization microscopy experiments investigate rather thin specimen such as adherent cells with heights of less than 10 µm. Here it is reasonable to go with simply rescaling the result (cf. section 2.3.1) and take advantage of the option to use highly inclined and laminated optical sheet (HILO) (Tokunaga et al., 2008) or total internal reflection fluorescence (TIRF) illumination to either enhance the excitation power density in the (axial) region of interest or to fade out background from parts of the specimen that are largely out of focus. But in the case that large volumes are to be imaged, the aberrations discussed will become important and as HILO and TIRF are restricted to heights close to the cover slip anyway, it is safer to match the refractive indices of the sample and the immersion medium. Recently, an algorithm for depth-corrected localization microscopy was published (McGorty et al., 2014) stressing that apart from aberrations the highest advantage of oil-immersion objectives is their ability to collect more photons than other kinds of objectives and that thus their precision is unprecedented. Also their data is restricted to a rather small axial range. I would not rely on an algorithmic approach for imaging of large axial distances because as I showed the shape of the PSF deviates from the calibration so fast and becomes so stretched in z that in my understanding its sensitivity has to decrease significantly as a function of the imaging height. Thus, from a purely physical point of view, any localization precision better than $\approx$100 nm is fundamentally inhibited when imaging deep inside a sample with non-matched refractive index.
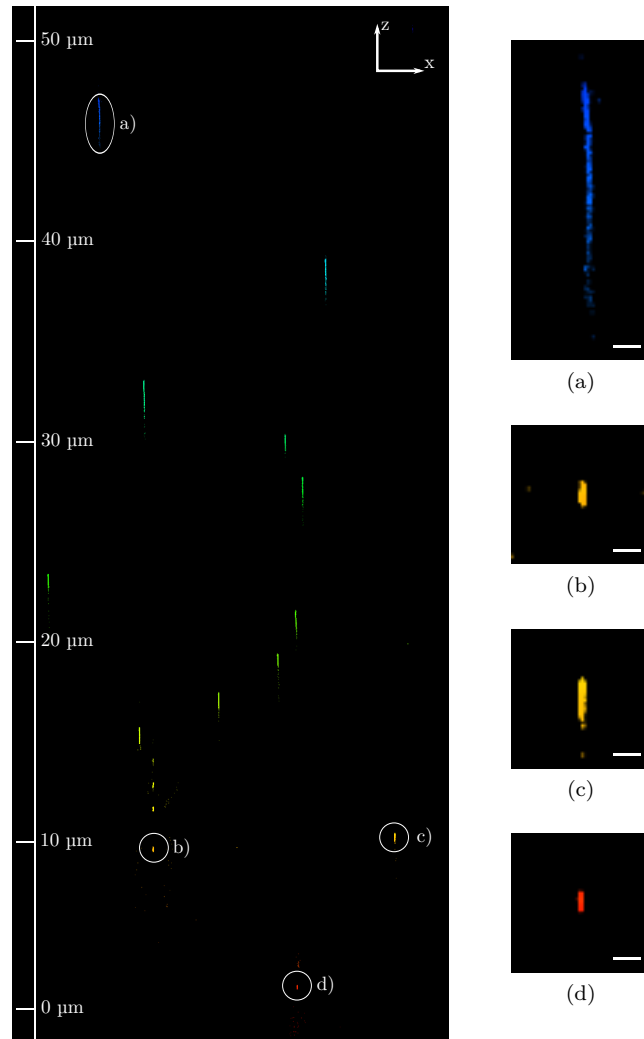
Figure 2.12: x-z view of the localizations obtained by the following experiment with oil-immersion: 100 nm TetraSpecks are immobilized statistically in Matrigel and the objective is axially scanned over 50 µm in z during the course of the measurement. After subtraction of the known objective movement, all beads should localize in one point if the calibration derived from the bottommost bead was valid over the whole axial range. There is a gradient in localization (in–) accuracy with increasing z. a) clearly indicates that using an oil-immersion objective is no safe choice for imaging far away from the surface. b) and c) support the notion that $z = 10$ µm is an upper estimate for the valid range of a calibration taken at $z \approx 0$ nm. Contrast is overemphasized for better visibility, the color encodes the axial position and the scale bars correspond to 10 µm in the main image and 300 nm in a)- d).
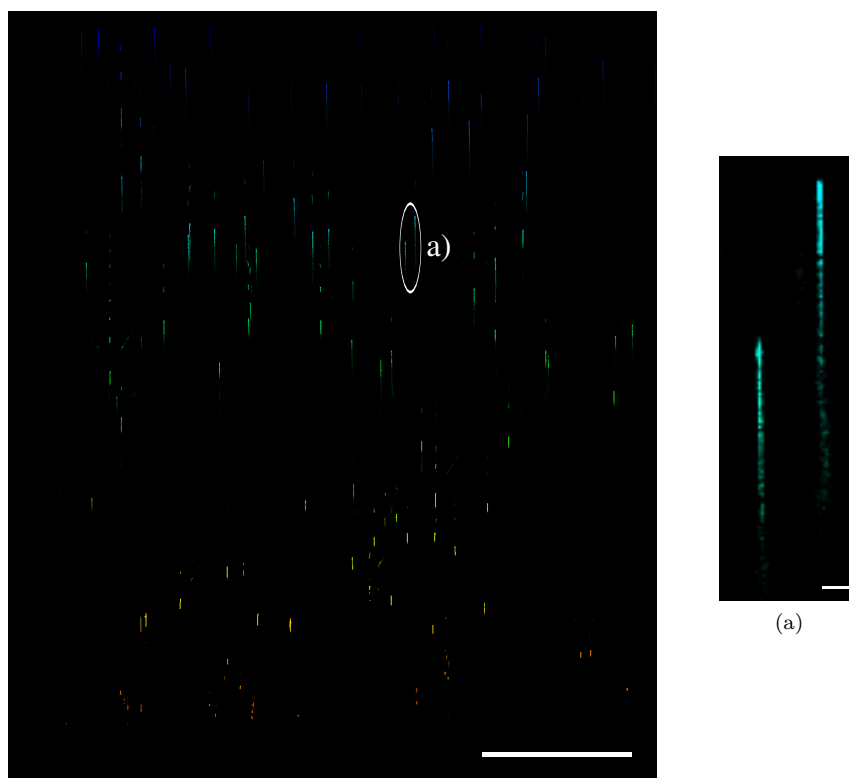
Figure 2.13: Same experiment as in 2.12. a) indicates the findings of (Deng and Shaevitz, 2009), that the localization precision is not axially symmetric as the trace stops abruptly at a certain position meaning that any localizations stemming from later frames were found precisely. Contrast, color and scale bars as in Fig. 2.12.
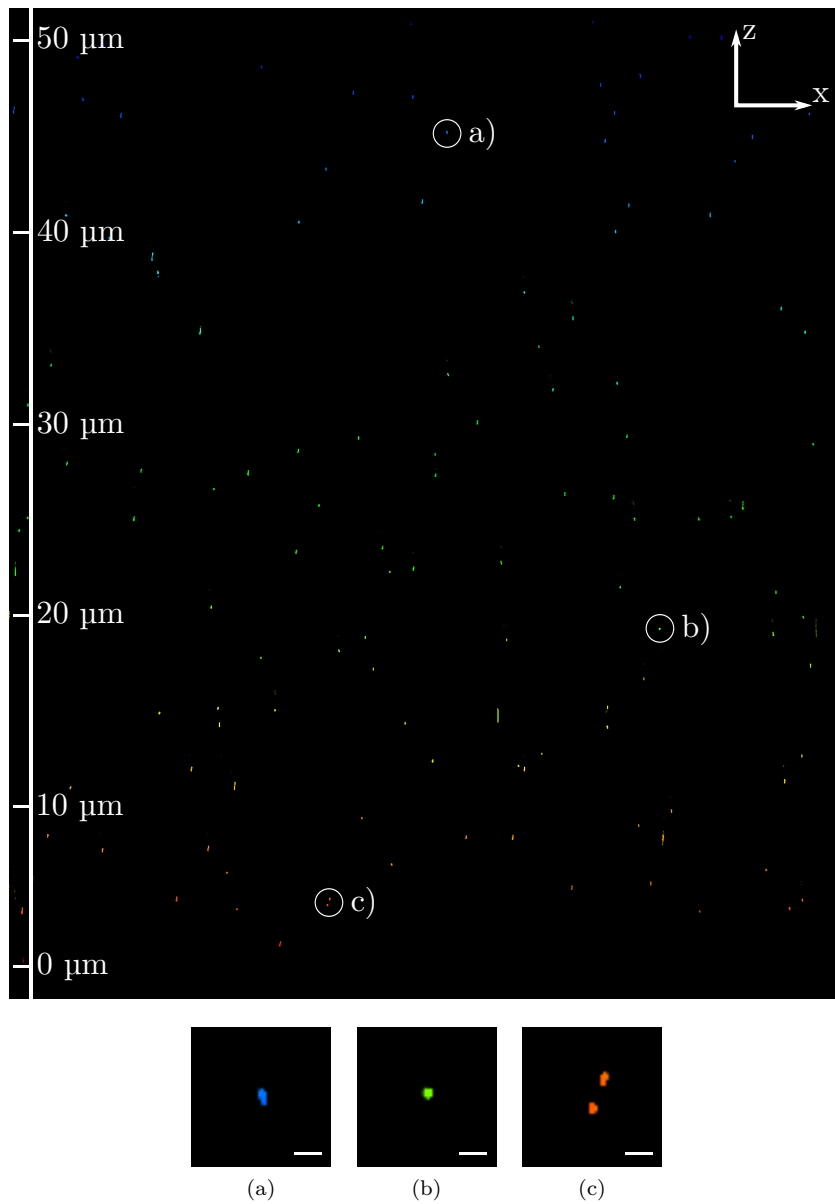
Figure 2.14: Experiment performed according to the description in Figures 2.12 and 2.13 but here, a water-immersion objective was used. Contrary to the aforementioned experiments, here, the calibration taken from the bottommost bead holds for the whole axial range of 50 µm. The zoom-ins in a) to c) highlight that all beads are localized with comparable precision and accuracy. Contrast, color and scale bars as in Fig. 2.12.

2.4 Cover slip tilt induced PSF deformation

So far, refractive index mismatch-specific aberrations have been treated and it would be a plausible notion to simply use a water-immersion objective when imaging in aqueous specimen. But unfortunately also this setup is prone to a distinct kind of aberration that will decrease the lateral localization accuracy if not treated carefully.

The only thing that can disturb the imaging behavior of a water-immersion objective is the cover slip. Most familiar is the fact that the use of a cover slip of wrong thickness will degrade the imaging properties / blur the image, thus decrease contrast and lead to axially asymmetric PSFs. Because in practice even high-precision cover slips may sometimes exhibit another thickness γ than their nominal thickness of 170 µm, many water immersion objectives have an objective collar which can be used to adjust the objective to imaging with cover slips with the thickness γ.

But another source for image errors cannot be accounted for by the objective: If the specimen is not leveled perfectly perpendicular to the optical axis but is tilted in any direction, undesired astigmatism will occur. This was described by (Arimoto and Murray, 2004) and they reasoned that if a cover slip is tilted in an axis x perpendicular to the optical axis z (the optical axis shall be the origin of x, left of the z-axis corresponds to negative x while right corresponds to positive x), the path lengths of light will differ for the positive– and negative half-space of x. That difference in path length is their explanation for PSFs that are axially bent to a banana-like shape (cf. Fig. 2.16c).

Not arguing with the aforementioned opinion, I prefer a different approach for explaining the phenomenon. We know from text books, e.g., (Demtröder, 2006), that a plan-parallel plate in a homogeneous medium introduces astigmatism. Here, we have exactly that scenario: The immersion medium is water and the specimen shall be assumed to be close enough to water in its refractive index, that it can be treated as water. The cover slip is approximately a plan-parallel piece of glass and therefore we have a plan-parallel plate in a homogeneous environment. What happens is sketched in Fig. 2.15: For simplicity, the cover slip is only tilted in the meridional direction, and thus in Fig. 2.15a the light only exhibits the focal shift the objective was designed for. But in the sagittal direction as shown in Fig. 2.15b the focus is dragged away from the optical axis. Furthermore, the focal length here is different to the undisturbed focal length as can be seen in the zoom-in in Fig. 2.15c where both meridional– and sagittal foci are displayed.
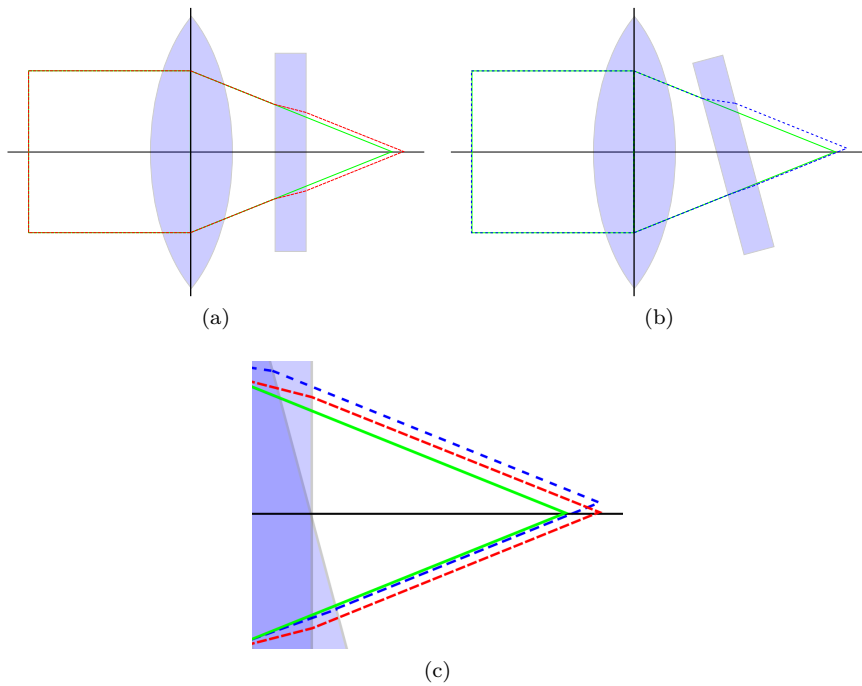
Figure 2.15: This figure gives a derivation by geometrical optics of the astigmatism caused by sample tilt. a) depicts the case, that the cover slip is aligned perfectly to the optical axis and thus no aberration occurs. In b) on the other hand, the cover slip is tilted which leads to a different focal length and another lateral position of the focus as compared to a). c) gives a zoom in of the resultant astigmatic focal points for imaging through a cover slip that is tilted only in the meridional– but not the sagittal direction.

This astigmatic disturbance leads to a significant loss in lateral localization accuracy as in that case the lateral coordinate becomes a function of z as the following example explains: Let's assume a perfectly vertical pillar with switching fluorophores attached at the bottom, in the middle and the upper end. These structures could for example be realized by the use of DNA-origami (Schmied et al., 2014). When theses switching fluorophores are localized they will all have comparable lateral coordinates if no tilt is apparent. But if the stage is tilted in x, the PSFs of the bottommost and highest fluorophores will be dragged away from the PSF of the fluorophore in the middle.

This aberration is especially bad for localization microscopy, because as already (Arimoto and Murray, 2004) stated, even a tilt of less than $1°$ already leads to a

significantly distorted PSF for water immersion objectives and Fig. 2.16 validates
their findings. Contrary to 2D localization microscopy where only a narrow axial
range is registered anyway, in 3D the resolution is limited by how accurately the
center coordinate is found over the whole axial range. If the leveling of the sample
stage was not performed carefully, the resulting astigmatic aberration can lead
to lateral (in–) accuracies of several hundreds of nanometers over the whole axial
range despite the usual 20 nm that is common for localization microscopy.

(a)   (b)   (c)
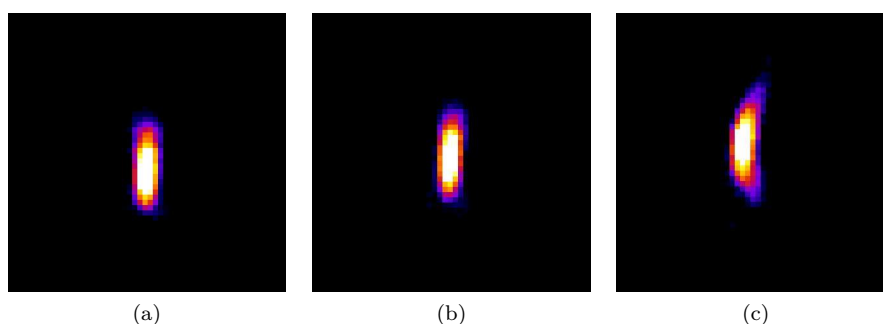
Figure 2.16: Measured x-z-profiles of PSFs for different specimen tilt. a) zero
tilt – the PSF shows no deviation from its lateral position–, c) ap-
proximately 1° tilt – the PSF is bent to the right-hand side and
would lead to lateral imprecision – and b) the tilt induced by one
adhesive strip under one corner of a LabTek (presumably around
0.05°) – a slight bending in the upper right corner of the PSF is
already visible.

This aberration can fortunately be extinguished to a satisfying degree with a
sample stage that can be leveled by micrometer screws, so there is no need for
the introduction of algorithmic methods – even though the lateral shift induced
by a tilted cover slip could presumably be calibrated. It is rather more advisable
to check the leveling of the stage prior to the beginning of each experimental
session (a protocol will be given in section 5.3) and this check is mandatory as
any data acquired with a misaligned optical system may lead to false conclusions.

2.5 Microscope design

The preceding considerations led to setting up the microscope described in the following. For details about the parts and filters employed please refer to Fig. 2.17, Tab. 2.2 and Tab. 2.1, respectively. The custom illumination and detection are built around a fully motorized Axio Observer.Z1 inverted microscope stand equipped with the Definite Focus autofocusing system.
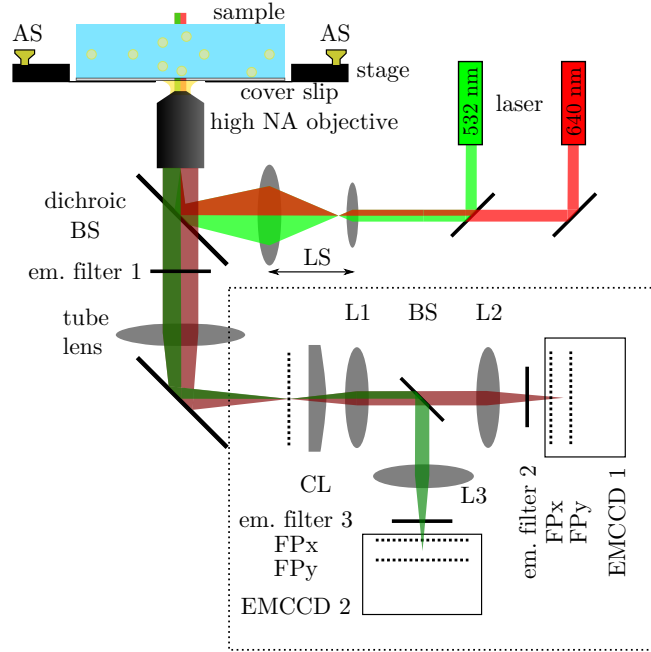
Figure 2.17: Sketch of the two-color 3D microscope as derived from the previous considerations. The illuminating lasers (404 nm and 488 nm are left out for simplicity) are combined by long pass filters and imaged on the back focal plane of the objective by a two-lens-system (LS). A quad-band dichroic beam splitter (dichroic BS) directs the light to the sample, the fluorescence emission passes through the dichroic beam splitter and an emission filter (em. filter 1) and leaves the stand via the side port with possible magnification using the Optovar. The light is imaged by three identical lenses L1-L3 on the two cameras EMCCD1 and 2. The long pass beam splitter (BS) thereby separates the two spectral channels. PSF engineering is obtained by a cylindrical lens (CL) that is placed in close vicinity to the focus near the side port. That leads to axially distinct focal planes for x and y (FPx and FPy). The adjustment screws (AS) serve for leveling the sample stage.

Four lasers (404 nm, 488 nm, 532nm and 640 nm) are combined with Laser-MUX long pass filters and imaged onto the back focal plane of the objective by a two-lens-system (LS). Focusing the light on the back focal plane leads to a wide field illumination in the sample which can be changed to HILO or TIRF illumination by moving the lens system with a micrometer screw.

The excitation light is directed to the sample by a quad-band dichroic beam splitter (dichroic BS) with a matching quad-band emission filter (em. filter 1) placed directly underneath in the filter cube. The stand is furthermore equipped with a 63x water-immersion objective with long working distance WD=0.6 mm while still having a considerably high NA of 1.15 for measurements deep inside a sample with aqueous refractive index and a 100x oil-immersion objective with an NA of 1.46 for measurements of thin samples close to the cover slip. The different magnifications of the respective objectives can be compensated with the Optovar (1x, 1.6x, 2.5x) in the microscope stand.

On the detection side, two Andor Ixon Ultra EMCCD cameras are coupled to a side port of the stand with a cage system assembled from Thorlabs parts. A 160 mm achromatic lens L1 parallelizes the fluorescence light to enable spectral separation of the two channels and two identical 160 mm achromatic lenses L2 and L3 focus on the respective cameras. All lenses are mounted in laterally adjustable optics mounts. Between the lenses L1 and L2 a long pass beam splitter (BS) is arranged at an angle of 45° for spectral separation and independent detection of the two channels. In front of each camera is another emission filter (em. filter 2 and 3) to ensure a clear signal with as little spectral cross-talk as possible.

The engineering of the PSF of single fluorophores is performed by a 250 mm achromatic cylindrical lens (CL) that resides in close vicinity to the focus near the side port. This position has three advantages: Between the lenses L1 and L2 is only very little space for putting the cylindrical lens and in this position in front of L1 the achromatic lens manipulates both spectral channels simultaneously. Third and most important, the amount of astigmatism induced by the cylindrical lens can be adjusted by axially moving the lens. If the cylindrical lens was placed in a parallel fraction of the detection path, the astigmatism induced will not be a function of the lens's position but constant for a given optical configuration. Thus, the focal length would have to match to the other optics while in the configuration chosen, the focal length of the cylindrical is of little importance.

The inverted stand is used even though section 2.4 suggests that the most elegant setup would be an upright stand with water dipping objectives because

then, aberration-free imaging is provided as there is no cover slip disturbing proper imaging. The inverted stand on the other hand has the certain advantage to provide TIRF abilities for thin specimen. For leveling the sample, a custom stage with adjustment screws (AS) is attached to the microscope stand with a highly sensitive XYZ positioning stage for moving the sample. The custom layout was necessary because the microscope should also be ready for perpendicular Selective Plane Illumination Microscopy / Lightsheet (SPIM) illumination.

All experiments were performed on this setup if not indicated otherwise.

Table 2.1: Used filters for wavelength clean-up of the lasers, beam combination and fluorescence imaging.

Part	Supplier
Wavelength clean-up:	
MaxDiode LD01-640/8	Semrock
ZET532/10x	
ZET488/10x	
ZET405/20x	Chroma
Beam combination:	
LaserMUX LM01-552-25	
LaserMUX LM01-503-25	
LaserMUX LM01-427-25	Semrock
Filter cube:	
BrightLine Di01-R405/488/532/635-25x36	
quad-band dichroic beam splitter	Semrock
ZET405/488/532/642m	
quad-band rejection filter	Chroma
Channel splitting:	
630 DCXR	Chroma
Detection:	
ET700/75m	Chroma
BrightLine FF01-582/75-25	Semrock

Table 2.2: Used parts for the two color 3D microscope.

Part	Supplier
Microscope stand:	
Axio Observer.Z1	
fully motorized	
1 bottom port, 2 side ports	
Definite Focus	
(autofocus system)	
Optovar 1x, 1.6x, 2.5x	
Halogen light	
Fluorescence revolver	Carl Zeiss Microscopy GmbH
Objectives:	
LD C-Apochromat	
63x/1,15 W Korr M27	
alpha Plan-Apochromat	
100x/1,46 Oil DIC M27	
A-Plan 10x/0,25 M27	Carl Zeiss Microscopy GmbH
two Andor Ixon Ultra DU897U-CSO	
EMCCD cameras	Andor
Lasers:	
iBeam smart	
640 nm 150 mW	
488 nm 200 mW	
404 nm 120 mW	Toptica
GEM 500	
532 nm 300 mW	Laser Quantum
Stage:	
Custom stage attached to:	
M-562 XYZ stage	
Nano PZA12 actuators	
PZC-SB controller	Newport
Lenses:	
three 160 mm achromatic lenses	
(detection)	
250 mm achromatic cylindrical lens	
(PSF engineering)	
either 20 mm or 40 mm and	
100 mm achromatic lens	
(illumination)	Thorlabs
Broadband dielectric mirrors	Thorlabs

2.6 Measurements demonstrating the performance of the 3D localization setup

2.6.1 3D measurements assessing the localization performance in a biological sample (microtubules)

The measurements with fluorescent beads presented in section 2.3.2 already give some estimates about the 3D precision as well as the accuracy and my co-workers and I published that the algorithm provides a good axial precision (Proppert et al., 2014). For dSTORM applications it is inevitable to finally assess these quantities in a real, i.e., biological specimen. While a determination of the localization precision is straightforward, there are only very few targets that are suited for a determination of the accuracy. To bypass this, I measured adherent cells that were fixed, permeabilized, and subsequently microtubules were labeled by Thorge Holm with indirect immunostaining with a primary mouse antibody (AB) against β-tubulin and a F(ab')$_2$ fragment of a goat-anti-mouse AB coupled with Alexa647. The 63x NA = 1.15 water-immersion objective was scanned in z with the microscope stand's z-drive during the course of the measurement, staying 100 frames in each position and then taking a 10 nm step in z thus leading to a mean movement of 0.1 nm per frame. Imaging was performed in switching buffer (called standard buffer) consisting of 100 mM β-mercaptoethylamine (MEA) at pH 7.4 and an oxygen scavenging system (glucose oxidase and glucose) with an NA 1.15 water-immersion objective, a power density of about 10 kW/cm^2 at 640 nm and an exposure time of 10 ms per frame.

The idea is, that localizations from a sufficiently small fraction of a microtubule should resemble the objective movement and the axial slope of the localizations can be taken as a measure of the axial localization accuracy. In other words, emissions from the beginning of the experiment should look like emissions from lower origin while localizations from the end of the measurement should look like emissions from upper origin and if there is a high agreement between the found localizations and the true slope of the objective movement, the accuracy is good.

We see, that the slope of the localizations fits well to the objective movement. I do thus reason, that the system accurately found the right axial coordinates. The deviation (FWHM) from the true slope in this experiment is 133 nm which at first sight seems to mean a rather bad precision. But if we take into account that the sample itself has an axial elongation, the value becomes more reasonable. Microtubules have a known outer diameter of about 25 nm (O'Connor, 2010) and
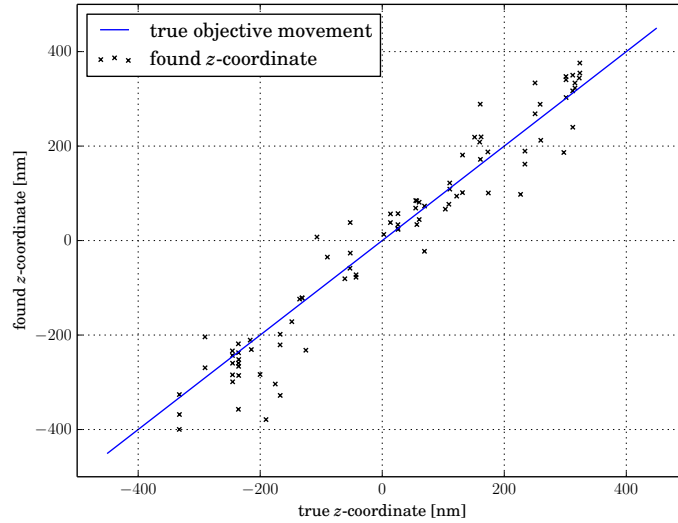
Figure 2.18: Axial accuracy estimate with microtubules. During the measurements, the objective was scanned in z with an average speed of 0.1 nm per frame indicated by the blue straight line. The localizations of a 300 nm section of a microtubule are given as black crosses and follow the slope of the objective movement.

atomic force microscopy estimated the diameter of an antibody to be about 8 nm (Dong and Shannon, 2000). We can now estimate the apparent size of the microtubule to be 25 nm plus the size of the antibody-F(ab')$_2$-pairs (I assume around 10 nm, as the F(ab')$_2$ is smaller and the binding site is not necessarily at the outer edge of the AB). In total, as a pessimistic assumption I assume the labeled microtubule to have a size of about 40 nm even though some work in literature assumes up to 50 nm. Subtracting these 40 nm from the 133 nm, the corrected value becomes 93 nm which would mean a sub-100 nm axial precision. This is not too bad for a first shot but I want to emphasize that this kind of measurement is not best suited for the extraction of a final axial precision. The aim was only to test the accuracy by checking if the optics and the localization algorithm can map the overall movement which it nicely does.

In this experiment, the movement of the objective is a significant source of errors, as we can a priori not trust the stand to take exactly 10 nm steps and even worse, for simplicity, I simplified the real movement (10 nm every 100 frames) to an average movement of 0.1 nm per frame. Another reason for the

rather large imprecision is that I had to assume that there was no axial drift but have no way to verify this assumption. These considerations explain to a certain degree the rather large value and I will show in the following that the axial precision of the system is in fact a lot better than the 93 nm estimated here.
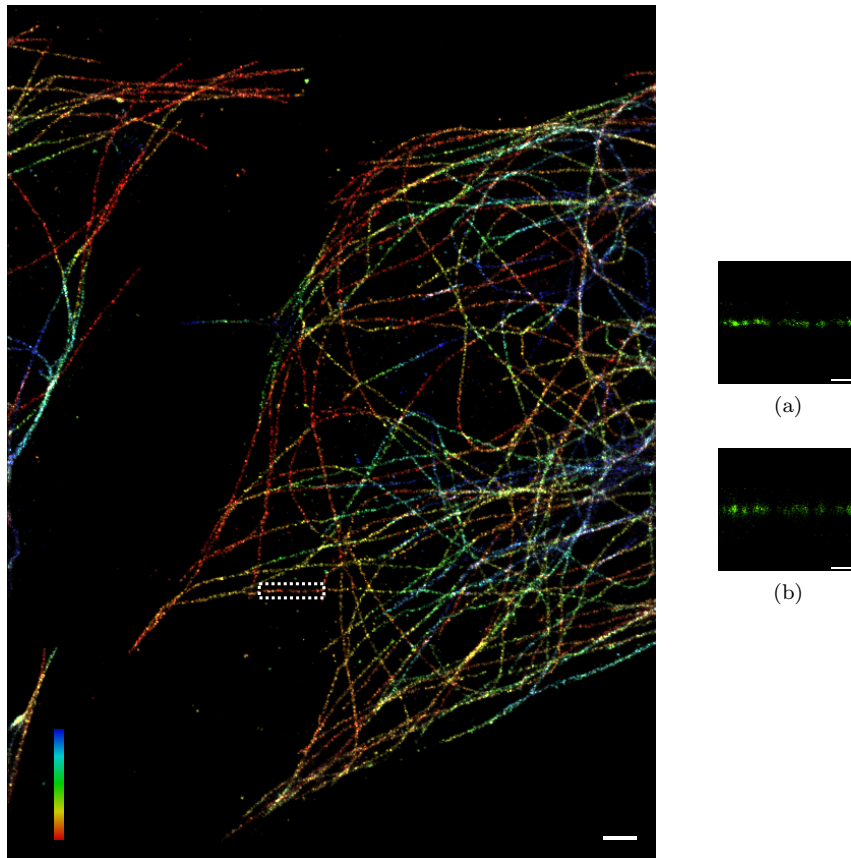
Figure 2.19: Microtubules stained by indirect immunostaining with Alexa647 and imaged in 3D. a) represents a microtubule section indicated by the dashed white box in the main image, while b) represents an x-z-view of the same section. The scale bars correspond to 1 µm and 300 nm in a) and b) and the axial position is encoded by the color covering an axial range of 700 nm.

Having verified with the latter experiment that the algorithm and optics not only find some axial position but the right position, I will now give some more realistic estimates for the lateral– and axial precision with another measurement. Microtubules prepared as in the latter experiment were imaged for 40,000 frames

under the same conditions but now, the objective remained at a fixed axial position with engaged definite focus system. The axial range in Fig. 2.19 covers 700 nm and x-y– and x-z- views of the microtubule section indicated by the white box are given in Figures 2.19a and 2.19b, respectively. Line-profiles (not shown) over the section of the microtubule yield FWHMs of 55 nm laterally and 90 nm axially.

Upon subtraction of the known size of the labeled structure of about 40 nm, in x-y we get a precision of 15 nm and the axial x-z precision we can estimate from this measurement becomes 50 nm. The lateral value is in good agreement with typical lateral precisions in localization microscopy and the about three times bigger value for the axial precision fits well to the fact that the PSF is about three to four times longer than it is wide.

2.6.2 The nuclear pore complex

The nuclear pore complex (NPC) – a transport channel in the nuclear envelope – has successfully been established as a test structure for assessing the lateral precision in 2D localization microscopy (Löschberger et al., 2012). It is straightforward to check, whether this structure is also a good candidate for testing the 3D precision. Here, a protein (gp210) in the outer ring of nuclear pores of A6 cells (*Xenopus laevis*, kidney) was indirectly immunostained with Alexa647 by Anna Löschberger and imaged under standard buffer conditions with an NA 1.2 water immersion objective on an earlier setup similar to that described in section 2.5. These proteins are known to form a ring with a diameter of about 145 nm to 160 nm and a sub-structure of eightfold rotational symmetry. The ability to resolve this eightfold symmetry is commonly taken as a measure for the lateral resolution.

I was not only interested in the localization precision of the bottommost layer of the cell but measured the whole nucleus by subsequent imaging of eight different axial planes and stitching together the resultant localizations. The assumption in this measurement is, that we can laterally resolve the ring and its eightfold sub-structure while axially we should at least be able to measure a ring with about 150 nm in diameter. The findings are summarized in Fig. 2.20 and Fig. 2.21. The pores that were oriented in plane are fairly well resolved laterally – a cross-section (not shown) gives a diameter in good agreement with literature and one can even count to eight in Fig. 2.21a. An x-z-view of the front of the nucleus represented in Fig. 2.21 already indicates that even though there are

(a)
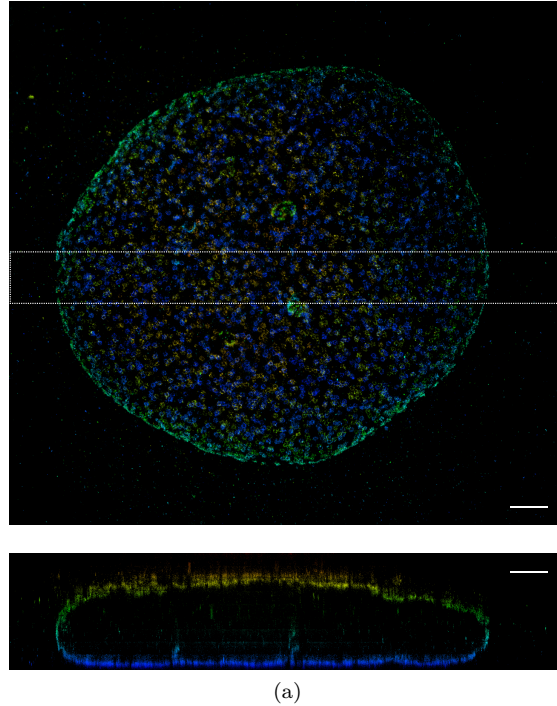
Figure 2.20: 2D projection of the NPC from a whole nucleus with an x-z-cross-section given in a). The cross-section indicates that the localization precision is not a function of z as the axial width of single pores is constant (with some deviation in the uppermost plane which I denote to a stitching artifact). The scale bar corresponds to 1.5 µm in both images and the color encodes the z positions with a range of 4.6 µm.

some pores that might be resolved, it is cumbersome to assess the resolution as many pores do not show a central dip.

On the other hand, some pores with x-z-orientation show a central dip. Figures 2.21d to 2.21f represent x-y–, x-z–, and y-z-views of a single pore that is axially tilted by about 50°. A cross-section (not shown) through Fig. 2.21f gives a distance between the upper– and lower edge of the ring of about 150 nm after accounting for the angular orientation. Considering the uncertainties of cross-sections taken from few localizations, a rather rough estimate of the angular orientation and the fact that we do not know whether or not this pore might have been squeezed a little, the obtained 150 nm fit well to the published values (Löschberger et al., 2012).

(a)   (b)   (c)

(d)   (e)   (f)
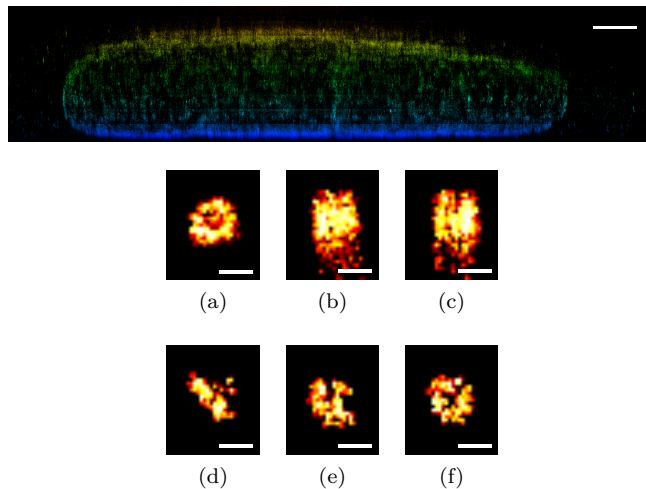
Figure 2.21: x-z-view of the front of the same nucleus as in Fig. 2.20 (axial range: 4.6 µm) and x-y–, x-z–, and y-z-views of a horizontally oriented single pore in a)–c) and a pore with inclined orientation in d)–f), respectively, demonstrating that the channel can be resolved in all three dimensions. The scale bars correspond to 1.5 µm in the upper graph and 150 nm in a)–f) while the color code is the same as in Fig. 2.20.

Overall, the NPC is a challenging target for the assessment of the localization precision and resolution in 3D because many requirements have to be fulfilled to image a target structure that has a diameter of only a little more than twice the anticipated axial precision. First to mention is the sample preparation as too few labels will hamper the resolution according to the Nyquist-Shannon sampling theorem (Shannon, 1984) while too many will lead to double-spot artifacts (van de Linde et al., 2010). Furthermore, even with a perfectly labeled sample, the buffer condition and irradiation power density has to be set perfectly for a sufficient on/off-ratio in order to avoid double-spot events. The requirements are even stricter than in 2D as we have to consider, that we want to estimate the widths of the PSFs of distinct fluorophores and extract their z-coordinates from these widths precisely. We thus have to deal with PSFs that are considerably bigger than common in 2D and therefor we need even lower on/off-ratios in 3D as in 2D – a prerequisite not overly met in this measurement as indicated by the false localizations in the center of the pore represented in Fig. 2.21a.

2.6.3 Centrioles

As the NPC proved to be a very challenging target, my next test subject were centrioles, a pairwise occurring cylindrical cellular compartment that is formed in mitotic cells and takes part in the organization of the mitotic spindle and cytokinesis. Each centriole usually consists of nine microtubule triplets. Rarer are centrioles consisting of singlets or doublets, but the ninefold rotational symmetry is preserved.

Centrioles have recently been introduced as potential rulers for localization– and other super-resolution microscopy techniques (Lau et al., 2012). For the experiments presented here, the protein CEP152 (Olivier et al., 2013) was indirectly immunostained with Alexa647 by Teresa Klein, imaged under standard buffer conditions with an NA 1.15 water-immersion objective and a camera exposure time of 5 ms/frame and approximately 10 kW/cm^2 epifluorecence-laser-illumination at 640 nm. Even though the short exposure led to a weaker signal it was nevertheless chosen to obtain as few double-spot events as possible as the measurements of the NPC proved that double spots have to be treated as a major source for false localizations.

(a)   (b)   (c)
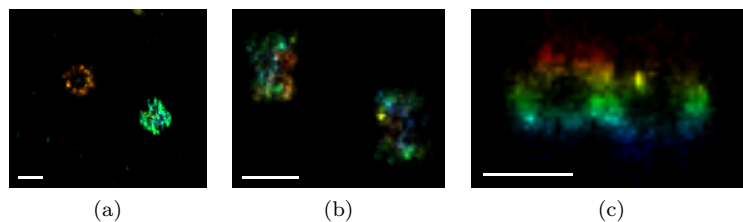
Figure 2.22: Centrioles in COS-7– (a)) and U2OS cells (b)-c)). The x-y-representation in a) demonstrates that the ninefold substructure of in-plane centrioles can be resolved while c) demonstrates the axial resolution of the ring structure of vertically oriented centrioles (x-y-representation of the same centriole given in b)). The scale bar corresponds to 400 nm and the axial position is encoded by the color covering a range of 400 nm.

The images in Fig. 2.22 were each reconstructed from 40,000 frames and show that if by chance a centriole with horizontal orientation is measured, the ninefold substructure can laterally be resolved (Fig. 2.22a). In the more likely case that the centrioles are randomly oriented, still the hollow cylindrical structure is well resolved. While SIM measurements estimated the diameter of a centriole to be about 435 nm (Lawo et al., 2012), all centrioles presented here exhibit a smaller

diameter of about 375 nm. This might originate from the cell lines used that differ from the one taken in the above mentioned paper.

Furthermore, in Fig. 2.22c the centrioles seem to be squeezed a little, i.e., their axial elongation appears to be smaller than their lateral width. This is at first glance a little confusing as the structure is proposed to be cylindrical and thus rotationally symmetric and it would be valid to think of the occurrence of some aberration. But fortunately, the figures in literature (Lawo et al., 2012) indicate as well that centrioles are not necessarily perfect cylinders. Because in theory there should be no aberrations apparent, I reason that this squeezing is indeed not an error but correct.

2.6.4 The synaptonemal complex

The synaptonemal complex (SC) is yet another interesting biological structure as it shows great potential for the assessment of the microscope's 3D resolution. The structure is a multiprotein complex that is specific for meiosis and plays an important role in genetic recombination as it stabilizes homologous chromosome pairing.

We know from transmission electron microscopy (TEM) that its structure looks like a ladder with two thicker outer rims (called lateral elements in the following) that are separated by about 200 nm (Wettstein et al., 1984) and a central element. The region in between the lateral– and central elements are reminiscent of the rungs of a ladder.

This ladder-like structure is interesting for 3D measurements as it is twisted around its center leading to a helical structure of which the height and the thickness should be comparable in their value. So, when measuring the SC, one can extract the nominal distance between the lateral elements straight ahead from a lateral (x,y) view and compare the value with the distance obtained in axial (z) orientation.

For this investigation, the testis of a mouse were extracted and single cells were immobilized on a poly-L-lysine coated cover slip. After short incubation the cells were fixed, permeabilized and stained with a primary AB against SYCP3 – a protein that is specific to the lateral elements – and a secondary AB coupled to Alexa647. The keeping of the mice, all extraction steps and the staining were performed by Katharina Schücker (Chair for Cell– and Developmental Biology, Theodor-Boveri-Institut for Life Sciences, Biocenter, Julius Maximilian University of Würzburg).

As purposely only the bottommost SCs of the attached cells were imaged, the measurement was performed with a 100x NA = 1.46 oil-immersion objective in standard buffer to maximize the SNR. As discussed in section 2.3.1, the resultant z-coordinates were divided by 1.14 to account for the stretch induced by refractive index mismatch.

We can extract from the different views in Fig. 2.23 that the distance between the lateral elements is indeed close to be constant and nearly isotropic. Cross-sections from the respective views (not shown) yielded the values for the distance between– and the size of the lateral elements that are summarized in Tab. 2.3.

(a)

(b)

(c)
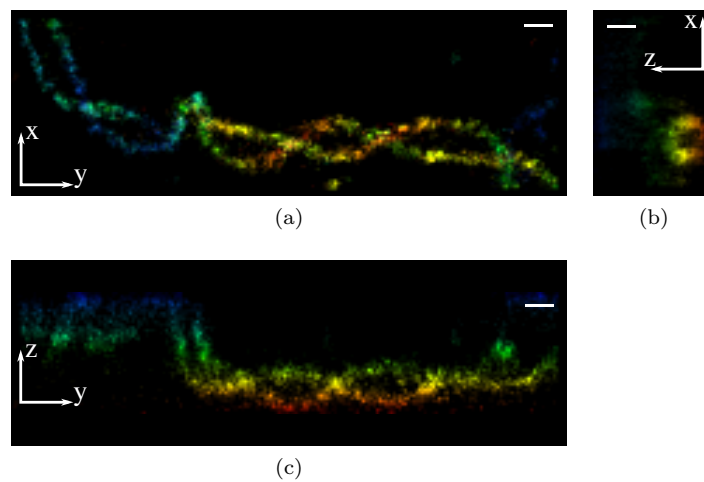
Figure 2.23: A 3D representation of the synaptonemal complex. a) gives an x-y-view of the SC, b) and c) resemble the respective x-z– and y-z-views of that same complex. Note especially that every crossing in a) corresponds to a region of maximum distance in c) and vice versa, indicating that the helical trajectories of the lateral elements are correctly imaged. The scale bars correspond to 200 nm and the axial range encoded by the color covers 850 nm.

It is interesting to notice that the lateral distance seems to be a bit longer than the axial distance but nevertheless, the values fit very well to the values that Katharina Schücker and Thorge Holm estimated from previous measurements (Schücker et al., 2014). It is planned for the future to repeat the experiment with a water-immersion objective to investigate whether that slight difference in the distance is biologically correct or whether the value of the correction factor was chosen erroneous. In my opinion, the most interesting here is, that the values for the thickness of the lateral elements in lateral– and axial orientation are very

close. That clearly indicates that the values are not limited by the respective precision but by the size of the lateral element itself.

Table 2.3: Distances extracted from the measurement represented in Fig. 2.23.

orientation	distance [nm]	thickness [nm]
x-y	230	70
y-z	220	85
x-z	220	85

As the SC can be well resolved and its dimensions renders it an easy target for 3D, it is in my opinion a perfect test sample for assessing the 3D resolution of a localization microscope. Not only can distances be precisely extracted but the very regular structure of the SC also provides a direct control of the imaging quality as false localizations and systematic deformations will become obvious immediately.

2.6.5 Bead-based demonstration of the 3D resolution with two colors over $25 \times 25 \times 100 \times \mathrm{\mu m}^3$

When it comes to two color imaging both the photochemistry of the fluorophores and the biology of the sample preparation lead to a manifold of new problems. The staining of two different cellular organelles can be a lot more complicated as there might not be a valid protocol that works for both organelles. For example, there are methanol-based protocols for the staining of the cytoskeleton that work very well for the preparation of microtubules but would wash away virtually everything else. Or even if the impact of the protocol was not as dramatic, some organelles are better fixed with formaldehyde while glutaraldehyde works better for the other. So, the staining protocol clearly is a first obstacle.

Another obstacle is that different fluorophores tend to need different switching buffer conditions. It has for example been shown that whilst enzymatic oxygen scavenging systems leads to more stable and bright switching of Alexa647, under these conditions Alexa532 will not show any significant switching. Therefore, the switching buffer always has to be a trade-off between the requirements of both fluorophores. To make it even worse, the exact buffer composition seems to be depending on the staining protocol and labeling technique used – even

different ABs seem to have an impact as I learned from numerous discussions with colleagues.

In order to avoid the obstacles of biological samples I again chose 100 nm TetraSpeck beads embedded in a Hydrogel (Matrigel) for assessing the three-dimensional two color imaging capabilities of the setup. The experiment was performed with a NA = 1.15 water-immersion objective as I showed before that oil-immersion is an inappropriate choice for imaging deep inside a specimen. During the image acquisition the objective was scanned over an axial range of 100 µm. During the evaluation of the measurement, the B-spline algorithm is allowed to localize in an axial lock-in range of ± 400 nm and the known objective movement is subtracted from the found localizations. If the precision is good and there is no extra aberration the result should be small elliptical localization clouds. For testing the co-localization performance, the (pairwise) Pearson correlation-coefficient for both channels is evaluated. The Pearson correlation-coefficient gives results on a scale from -1 to 1 with -1 meaning perfectly anti-correlated data, 0 (zero) meaning no correlation at all and 1 meaning perfect correlation. With a high correlation-coefficient obtained at worst the channels could have some constant offset that can easily be subtracted.
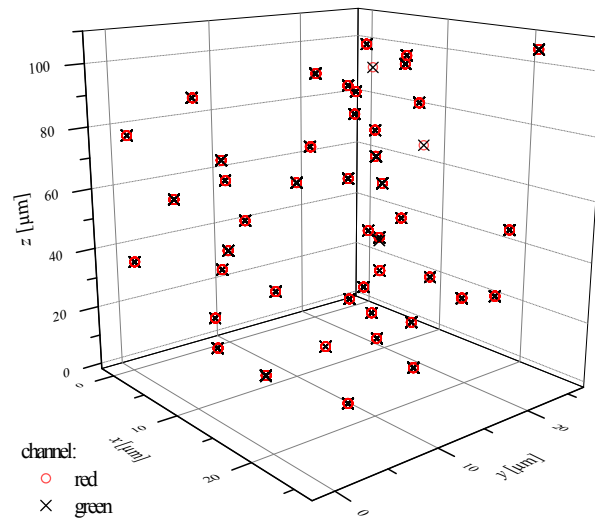

Figure 2.24: This three dimensional plot visualizes that there is a high correlation between the red– and the green channel and that there is no significant z-dependent aberration.

There were quite a few open questions I want to address in the following. In the first attempts to do 3D localization, a simple $f = 1000$ mm cylindrical lens

without achromatic correction was used and it was questionable whether that lens could be used simultaneously for red emission around 700 nm and green emission around 600 nm respective wavelengths. It turned out that the impact of chromatic aberration was even worse than expected and while the defocusing in the red channel was adjusted to be decent, the de-focusing in the green channel was way too extreme leading to a very short axial range. In fact there is no position where the lens can be placed that leads to satisfying results in both channels.

One bypass of this problem would have been to use one cylindrical lens in front of each camera – two lenses in total – instead of one cylindrical lens for both cameras and to adjust both lenses independently. But then suppliers launched affordable achromatic cylindrical lenses and I preferred to assess their performance because in the end, a setup with only one cylindrical lens would be easier to maintain. It turned out that even the cylindrical lens doublet with achromatic correction exhibits some chromatic aberration but the amount of aberration was small enough to enable finding a trade-off position that works well enough for both channels.

Another big obstacle in two color imaging is that there are always some displacements and aberrations between both channels. In 2D these are accounted for with a transformation matrix aligning the green and the red channel accordingly. After choosing a cylindrical lens that is suited for two color imaging and its position, it was another open question whether a two color transformation matrix is valid for every imaging depth or whether a transformation must be obtained for each imaging depth individually. Figure 2.24 indicates that the transformation is not dependent on the imaging depth. If that was the case, the co-localization should degrade the deeper inside the specimen. This 3D plot shows no shear between the channels and no systematic displacement in any direction and I therefor reason that for well aligned two color 3D measurements, no prior knowledge about the imaging depth is required. The evaluation of the Pearson correlation-coefficient strongly supports the aforementioned notion as the respective correlation values of the $x-$, $y-$ and z-coordinates of the red– and the green channel are 0.99, 0.99 and 0.98.

Now having assessed the localization accuracy of two color 3D imaging, the last missing quantity is the precision of both channels. As from the previous experiments I can assume that there is no significant loss in precision over the covered axial range, I wrote a small algorithm to superimpose all bead traces in each channel and subsequently evaluate the statistical standard deviation which

is then converted to the FWHM of the localization distribution in x, y and z. For the identification and extraction of the bead traces I used the rather conservative criterion that two subsequent localizations of the same trace should show no lateral displacement bigger than 50 nm. Before superimposing the obtained traces, I furthermore filtered out traces that had an unreasonably large axial imprecision of more than 150 nm.

Table 2.4: Two color 3D localization precisions FWHM and the respective standard error of the mean (SEM) obtained from simultaneously imaging 100 nm TetraSpeck beads over an axial range of 100 µm. The values are rounded to integers.

dimension	FWHM [nm]	SEM [nm]
Green channel:		
x	23	< 1nm
y	17	< 1 nm
z	68	< 2 nm
Red channel:		
x	14	< 1 nm
y	17	< 1 nm
z	67	< 2 nm

Some traces may not have been found by the trace filter and others could simply not have been apparent in both channels, so the FWHM was computed for a different amount of traces. Evaluation of 23 traces in the green channel and 27 traces in the red channel yielded the values summarized in Tab. 2.4.

It is very interesting to note that these values seem inconsistent with Thompson / Mortensen according to whom the localization precision scales with the brightness of the emitter (cf. equations (1.9)). It does not fit to that theory that the FWHMs of the localizations here are different for x and y and that even though the red channel is better in x the value in y is the same as in the green channel. To make it even more confusing, the green emissions were three times brighter than the red emissions and should therefore exhibit better localization precisions.

Of course, in fact it is not inconsistent as we have to realize that the FWHMs not only depend on the localization precision which is a function of the SNR but they also depend on the localization accuracy and the latter is limited by the alignment quality of the imaging optics.

3 Possible strategies for extending 3D localization microscopy to huge volume imaging

While I have shown in the previous sections that imaging over a large axial range is fundamentally feasible, it is still a challenge in biological samples as they are in general not homogeneous, transparent and the fluorophores are limited in their brightness. In the following I will outline some strategies to bypass this obstacle and to enable imaging of huge volumes on a scale of $100 \times 100 \times 100$ µm^3.

3.1 Selective Plane Illumination Microscopy / Lightsheet

The imaging of huge volumes is for example of special interest in neurology as it can elucidate the synaptic plasticity and connectome of whole brains. So far, neurological studies are often performed with adherent neuronal cell culture specimen which is an artificial sample compared to brains extracted from formerly living animals.

Since its introduction (Huisken et al., 2004) SPIM gained a lot of interest as it enables the investigation of small organisms like zebrafish with unprecedented resolution while minimizing the irradiation-introduced stress. The argument, that a combination of SPIM with localization microscopy would minimize phototoxicity of living samples obviously does not hold because if we imagine to scan a zebrafish and performing localization microscopy in each axial section, the whole specimen was sequentially subject to very high laser power densities as they are needed for switching fluorescent dyes.

But on the other hand, SPIM can still prove to be very beneficial as by selectively illuminating only the imaging plane, the SNR is significantly enhanced as compared to epifluorescent illumination of the whole sample at once. The fluorophores also benefit from a perpendicular illumination scheme as upper planes of the specimen will not be illuminated the whole time but only when imaging of these planes is performed. This will greatly enhance the longevity of the fluorophores and presumably improve the image quality.

In order to enable SPIM measurements on an inverted microscope I developed a custom specimen chamber which is sketched in Fig. 3.1. The chamber is assembled from a block of polydimethylsiloxane (PDMS) that serves as a support for holding together the bottom cover slip and a side window of cover slip thickness. The gap between the bottom cover slip and the window is sealed with a UV-curing lens glue (Norland NOA 68).
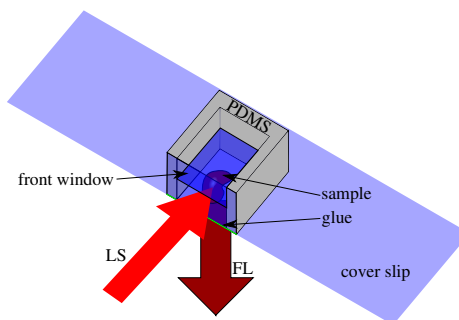
Figure 3.1: Custom specimen chamber for perpendicular illumination and compatibility with inverted microscopes. The lightsheet laser illumination (LS) hits the sample via a window which is glued (indicated by the green straight line) to the bottom cover slip. The chamber is tailored to be compatible with the collection of fluorescence light (FL) by an inverted microscope.

A master student assessed the possibility to perform localization experiments with SPIM illumination and therefore cultivated adherent cells on different hydrogels with matching refractive indizes. As an example, Fig. 3.2 gives a reconstructed 2D representation of microtubules stained with Alexa647 in a HeLa cell cultivated on Matrigel. Unfortunately, by that time the essentials of 3D localization imaging were still under investigation but the result is nevertheless promising as it shows that also with perpendicular illumination a reasonable localization precision can be obtained.
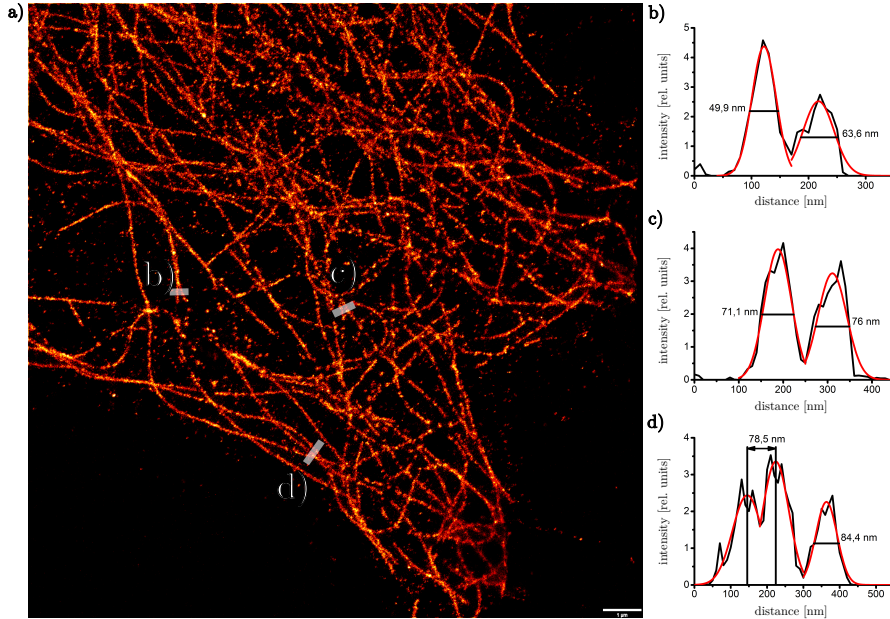
Figure 3.2: Precision estimates from a SPIM measurement of micrutubules with line profiles as indicated in a). Reproduced (translated) from (Wengler, 2012).

But there is still a lot of work to be done. For example, in every experiment so far drift was only accounted for by estimating an average linear drift, but this will not be sufficient for stitching together subsequent measurements over long axial ranges. A promising approach here would be to use fluorescent beads that are statistically embedded around the sample and can be tracked during the measurement as proposed by (Zessin et al., 2013). We have to keep in mind that this might significantly complicate the sample preparation and in my opinion a tailored strategy has to be found for each kind of sample independently.

Another obstacle will be that biological samples are in general not translucent and exhibit varying refractive indizes which will degrade the SNR and will possibly also hamper the axial localization as variances in the refractive index cannot be precisely accounted for by any z-calibration method. One promising way around these problems is to clarify (Chung and Deisseroth, 2013) the sample prior to the imaging.

We will see where SPIM localization microscopy will go as the ongoing experiments with scanned lightsheets and a modified OpenSPIM setup[1] of two other Master students I work with are very promising.

3.2 From brain slices to array tomography

As there are still many remaining obstacles in combined SPIM localization microscopy, I want to shortly outline another approach initiated and mainly driven by Martin Pauli (Institute of Physiology, Department of Neurophysiology, Julius Maximilian University of Würzburg) who also did the sample preparation. His strategy is to produce brain slices of 1 µm thickness or less and imaging the synaptic plasticity of different regions in the brain with localization microscopy. While most of these measurements were so far performed with 2D imaging, we tried 3D imaging as well as this allows addressing questions that cannot be answered with two-dimensional imaging.

(a) (b)
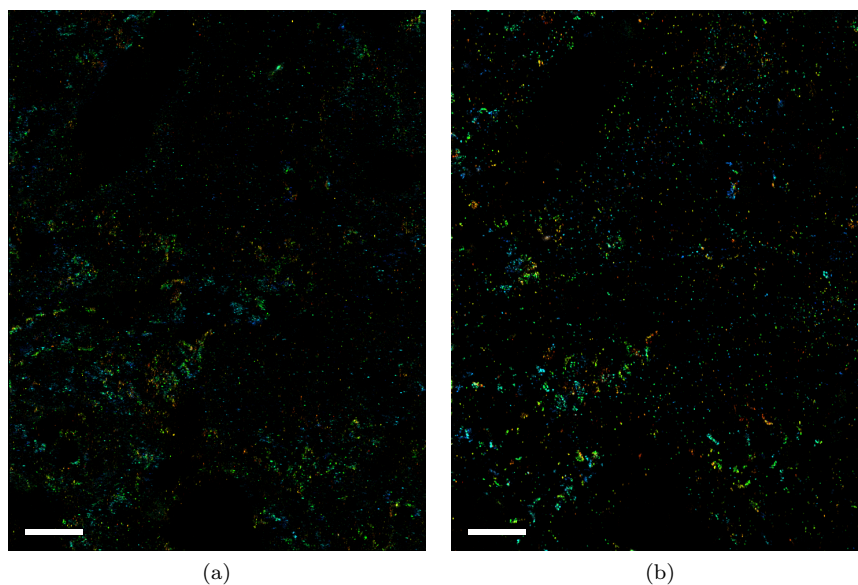
Figure 3.3: 3D measurements of a 1 µm brain slice. a) represents the signal from the presynaptic protein Bassoon which was labeled with Alexa532 and b) represents the postsynaptic signal of Homer labeled with Alexa647, with the color encoding the respective z-coordinates. The scale bars correspond to 3 µm and the axial range covers 850 nm.

---

[1] http://openspim.org
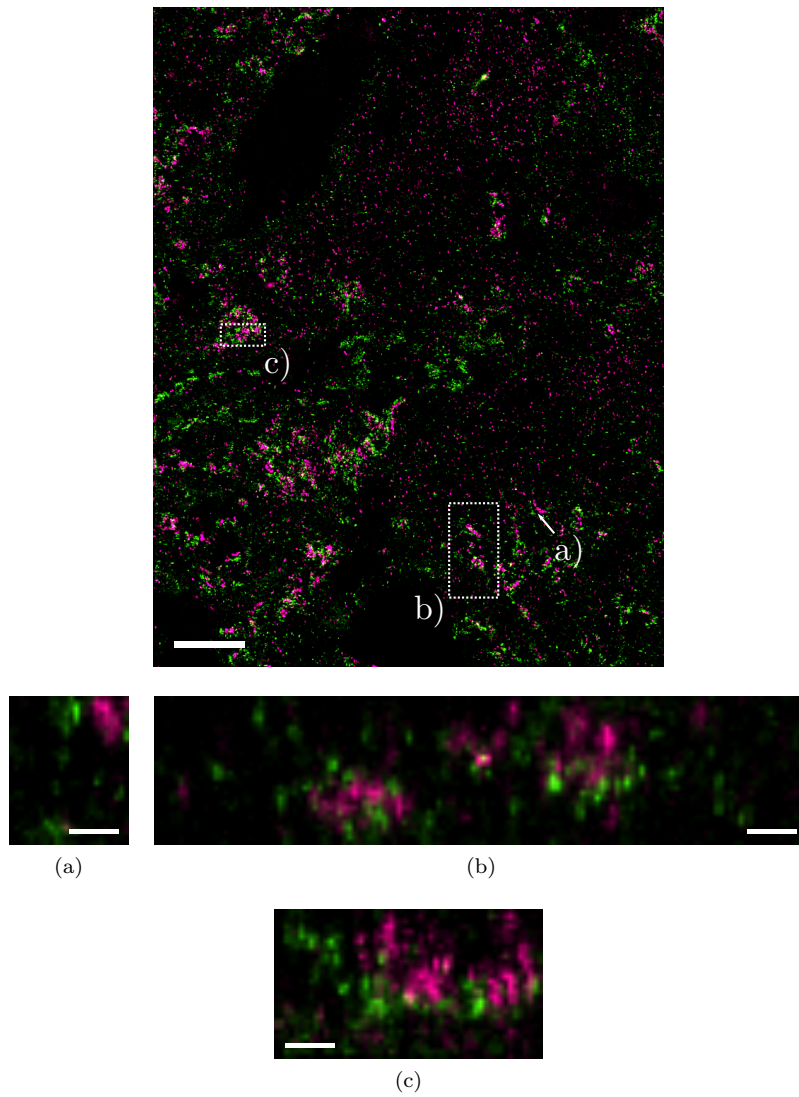
Figure 3.4: Superposition of the measurements from Fig. 3.3 (green: Bassoon, magenta: Homer). The boxed regions indicate the respective regions from which the x-z-views in b) and c) were extracted and the arrow indicates the viewing angle of the x-z-view in a). a) represents a x-z-view of a vertically oriented synapse, the y-z-representation in b) indicates that one synapse was horizontally oriented while the other shows vertical orientation and c) represents an x-z-view of a section of another horizontally oriented synapse. The scale bars correspond to 3 μm and the axial range covers 850 nm in the overlay, while the scale bars in a)-c) correspond to 300 nm.

One major difference between neuronal cell culture and slices taken from a mouse brain is the orientation of the synapses. While most synapses show a parallel orientation to the z-axis and thus the pre– and postsynaptic sides are imaged as two parallel lines in neuronal cell culture, in a brain slice the synapses are distributed with random orientation. This leads to the problem in analysis of the synaptic plasticity that, while there still is the possibility to get an estimate of the synaptic density, it is more problematic to assess the average size of a synapse or a change in size. This is a hard to assess quantity in brain slices as the obtained size of a synapse is a function of the orientation of the synapse which is not accessible from a 2D projection.

In the following I will discuss some preliminary data demonstrating that three-dimensional imaging can produce extra knowledge about the orientation of individual synapses. Figures 3.3a and 3.3b show reconstructed images of measurements of the presynaptic protein Basson labeled with Alexa532 and the postsynaptic protein Homer labeled with Alexa647, respectively, with the color encoding the axial position. Figure 3.4 is an overlay of both measurements now encoded green for Bassoon and magenta for Homer for better visibility. We see that both channels are reasonably aligned and that there are indeed some synapses found that seem to be oriented vertically (one green– and one magenta structure that are parallel to each other) and others that might have horizontal orientation (those, where both signals overlay in the 2D projection in Fig. 3.4).

The exemplary representations of synapses with different orientation in subfigures 3.4a to 3.4c may not be striking evidence but they point in the right direction. The synapse in Fig. 3.4a may indeed be oriented vertically as the x-z-view along the localization patterns gives two parallel signals. On the other hand the synapse shown in Fig. 3.4c seems to be oriented horizontally as in the x-z-representation the magenta localizations are on average plotted to higher coordinates as the green ones and Fig. 3.4b indicates that the synapse left in this figure is oriented vertically while the right one is oriented horizontally.

These measurements show some key advantages of 3D localization microscopy. Even though the axial resolution of tomographic EM imaging of ultrathin sections (a slice thickness of about 40 nm is achievable) or imaging and subsequent ablation with a Focused Ion Beam (FIB) is at least as good as in 3D localization microscopy or even better, fluorescence imaging still excels in the specificity and label efficiency of commercially available ABs coupled to organic dyes. Compared to fluorescent labels, the staining with immunogold ABs generally suffers from way worse quality. Furthermore, 3D localization imaging is faster and less inva-

sive in sample preparation as other techniques and especially in data acquisition. While EM has to perform ten measurements of 100 nm slices with subsequent stitching, 3D localization microscopy obtains even denser data at comparable resolution with only one measurement of a 1 µm slice.

For imaging larger volumes of a brain an array-tomographic approach can be followed. Array tomography means that several subsequent slices are imaged individually and a volume view is reconstructed by stitching the respective results together. As the amount of data obtained by such experiments is immense, the crunching of the data will be a major challenge for the future and the introduction of standards will be most important for the extraction of solid conclusions.

If now SPIM can contribute here with its ability to *in situ* slice a specimen optically, that would be a new very elegant and robust way of investigating the brain possibly paving the way to completely new insights.

4 Conclusion

Since its introduction around 2000 and the extension of the method to localization microscopy around 2008, e.g., (Schütz et al., 2000, 2001; Holtzer et al., 2007; Huang et al., 2008a), the various techniques for obtaining three-dimensional information about the distribution of single molecules in biological samples gained significant interest. My own experience from conferences is that the fundamentals of 3D PSF engineering and fitting are believed to be well established but to my knowledge they were poorly documented previously.

Therefor, I wrote this thesis with a special emphasis on summarizing and reviewing the basic optics that have to be concerned. A major aspect qualifying this thesis as a new contribution to the field is the systematic consideration of challenges as they will occur depending on the sample that is to be imaged and the optics that are used.

By imaging various biological and artificial samples I was able to confirm the validity of my considerations, as resolutions of about 20 nm laterally and 70 nm axially (FWHM) could be demonstrated even for two color experiments. I was as well able to demonstrate that the developed microscope also localizes accurately in z when all limitations of the respective optics are accounted accordingly. But at least as importantly, this thesis outlines that especially the accuracy drops dramatically when imaging is not performed correctly, i.e., fit to the respective sample. Especially, the use of an oil-immersion objective for deep volume imaging has been proved to be an invalid choice. I want to emphasize that so far the optics have caught little attention as the brightness of fluorophores was identified by the community to be the key parameter but this identification is dangerous. We have to remember that the fluorophore brightness can only be the second most important parameter because even the brightest fluorophore is useless if imaged poorly.

It has been demonstrated in this work that depending on the sample, the choice of the detection objective has significant impact on the resolution that can be obtained. While the widespread use of oil-immersion objectives is a reasonable choice for the imaging of thin samples or for measurements that are

restricted to the vicinity of the bottom cover slip, the often believed superiority of that kind of objective was shown to be wrong for deep volume imaging. I have demonstrated that the refractive index of the sample has a major impact on the axial localization accuracy when imaging beyond 10 µm inside the sample without matching the refractive index.

If on the other hand the refractive index is matched, one major advantage, i.e., the ability for TIRF, is lost. There are still some advantages remaining, one being that oil-immersion objectives are commonly available in most labs while objectives using other immersion media are rarely found. Another is the superior light collection efficiency. But considering that it is cumbersome to adjust the refractive index of the switching buffer and the specimen to the refractive index of oil while still preserving good photoswitching capabilities, it is in my opinion well worth considering to go the other way and match the immersion medium of the objective – and thus the objective itself – to the conditions of the specimen.

In most cases, a sample in localization microscopy can be assumed to be an aqueous environment and thus the use of a water-immersion objective is the method of choice for deep volume imaging as this objective with matched refractive index does not suffer from a z-dependance of its image quality. In the future, when the technique may be extended to imaging deep in tissues, the objective of course would have to be matched to that regime and there a glycerol-immersion objective should be best suited.

However, on inverted microscope stands even with matched refractive indizes the alignment of the sample has to be carefully checked. As discussed in literature (Arimoto and Murray, 2004) and verified in this work, for matched refractive indizes, the sample orientation is a crucial parameter. That is, it has to be verified that the bottom cover slip is oriented perfectly perpendicular to the optical axis as even slight angular deviations of the order of 1° lead to a significant deformation of the axial profile of the PSF. This deformation leads to a significant loss in lateral accuracy and is not trivial to account for afterward. Fortunately, a seasoned experimentalist is able to guarantee a good imaging ability with little efforts. Please refer to section 5 for detailed descriptions on how to assess the alignment and re-align the microscope if necessary. As many biological samples are tailored during their preparation for the use of inverted microscopy, it is totally reasonable to build up 3D localization microscopes alike the one characterized in this thesis. But it has to be kept in mind that this device will not be a failsafe microscope in the near future.

In a nutshell, both water– and oil-immersion objectives have major disadvantages when used on inverted microscopes. I would therefore recommend for forthcoming developments to consider using an upright microscope stand rather than an inverted microscope. Even though inverted microscopes have become a standard in biological studies, an upright microscope has the certain advantage that dipping objectives can be used. So, when using a water-dipping objective the axial uniformity of the imaging quality found for water-immersion objectives should be granted and additionally cover slip-induced aberrations will be eliminated. The only aberration that can then still occur is sample-induced and they would be apparent in any measurement on any other kind of microscope as well. If highest resolutions are not needed anyway – and imaging deep inside a sample will almost certainly coincide with a loss in resolution due to sample inhomogeneities – I conclude that employing dipping objectives for fluorescence detection is the most elegant and robust solution.

But a good microscope is only one prerequisite for successful localization microscopy. The other is the availability of reliable algorithms for extracting the z-coordinate from the shape of the PSF. As described in this work and in (Proppert et al., 2014) a new interpolation methods based on cubic B-splines was introduced and thoroughly tested. I reason, that the implementation in rapi*d*STORM is the first method that can combine precision, accuracy and simplicity. This desirable combination withdraws one of the most important obstacles, i.e., the question whether the results can be trusted. The fact that this implementation is freely available with rapi*d*STORM makes it even more valuable for the community.

5 Protocols for two color 3D alignment

5.1 Preparation of TetraSpeck surfaces

Needed chemicals:

- 10% sodium azide (NaN_3) in water (toxic)

- TetraSpeck Microspheres, 0.1 µm, T-7279, life-technologies

- distilled water / Millipore filtered water (called distilled water in the following)

- 1:1000 dilution TetraSpeck stock in distilled water

- Thermo Scientific Nunc LabTek II chamber slide (called LabTek in the following)

- Kimwipes, Kimtech Science

- Parafilm sealing tape, Sigma-Aldrich

Preparation of the surface:

1. Fill one or more chambers of the LabTek with 500 µl distilled water.

2. Vortex the 1:1000 dilution TetraSpeck stock in distilled water shortly.

3. Pipette 50 µl of the 1:1000 dilution to each chamber previously filled with distilled water.

4. Mix thoroughly by pipetting and re-dispersing the whole volume of each chamber multiple times (alternatively prepare and vortex the mixture in an Eppendorf tube).

5. Because 100 nm TetraSpecks do not sediment, the solvent (distilled water) has to be evaporated. Put the prepared LabTek without its cover in a drying oven pre-warmed to 50-70°C.
   ↪ Do not use too high temperatures as the plastic and glue of the LabTek might degrade and you also do not want the water to boil because then the TetraSpecks could vanish with the water vapor.
   ↪ Cover the LabTek with a Kimwipe to prevent dust from falling onto the sample.
   ↪ Leave the LabTek in the oven until the water is fully evaporated.

6. Carefully add a new 500 µl of distilled water and 20 µl of the sodium azide stock. Mix carefully and seal the LabTek with Parafilm for storage (unseal it for calibration!)
   ↪ The refractive index of the sample must resemble aqueous environments for calibration purposes – air would be inappropriate.
   ↪ Sodium azide inhibits the growth of bacteria and other undesired biological units.

5.2 Preparation of TetraSpecks dispersed statistically in 3D in Matrigel

Needed chemicals:

- TetraSpeck Microspheres, 0.1 µm, T-7279, life-technologies

- Matrigel matrix, phenol-red free, Corning

- 1:200 dilution of TetraSpeck stock in Matrigel

- Thermo Scientific Nunc LabTek II chamber slide (called Labtek in the following)

- 4% formaldehyde solution (toxic) in distilled water pre-warmed to 37°C for further cross-linking the thermally unstable Matrigel

- Parafilm sealing tape, Sigma-Aldrich

- 10% sodium azide (NaN_3) in water (toxic)

Side note to Matrigel:

Matrigel is a bio-polymer hydrogel that comes in a rather large stock volume. It is advisable to split the stock to 1 ml aliquots under a clean-bench that can be stored at -20°C for long term. According to the manufacturer, a Matrigel stock stored at 4°C may degrade over time. Be aware that Matrigel is also sensitive to multiple freezing and thawing cycles. The needed aliquot should thus only be thawed once. Be most careful: Put the aliquot on ice and let it thaw *on ice* at 4°C over night. Once thawed always keep it at 4°C as otherwise Matrigel might start undesired cross-linking or degrading. In other words: Work quickly, keep it on ice if possible and keep in mind, that especially your fingers are an excellent warmth supply.

Matrigel is liquid at 4°C and cross-links at 37°C. The cross-linked state, however, is not stable when the sample is stored at room temperature. I thus recommend that once the thermal cross-linking is done, you should further cross-link it chemically with formaldehyde. Glutaraldehyde may work as well and should cross-link even better but it is known to introduce background. It might be worth a try.

Sample preparation:

0. You must be fast here, so read the protocol carefully and have everything prepared before you start.

1. Quickly vortex the 1:200 TetraSpeck dilution *once.*
   ↪ *Do not* try to mix it in an ultrasonic bath as this would disrupt the bio-polymers.

2. Pipette 10 µl of the 1:200 TetraSpeck dilution to the central region of each LabTek chamber you want to use.
   ↪ 10 µl is enough for a 1-2 mm strip over the whole length of the chamber. The resultant thickness after cross-linking should be sufficient for most experiments. For thicker coatings, more material is needed and the time for thermal cross-linking may have to be adjusted.
   ↪ Hint: It is a good ideal to add a small air bubble at one edge of the sample chamber because Matrigel is transparent and its refractive index is very close to that of water. The air bubble helps to find the Matrigel layer on the microscope.

3. Put the TetraSpeck in Matrigel dilution back at 4°C.

4. Put the covered LabTek in a 37°C cell culture incubator. Let the sample cross-link for 35 minutes.
   ↪ Respect the rules for cleanly working in cell-culture, i.e., wash and disinfect hands. If in doubt, ask staff.
   ↪ The cell incubator is needed for two reasons: 1. its stable temperature of 37°C and 2. its humid atmosphere. If you try to cross-link Matrigel in dry environments, the gel will sooner fall dry than cross-link.

5. Pre-warm the 4% formaldehyde solution in a 37°C water bath.

6. After the 35 minutes, take the LabTek out of the incubator, quickly check whether the Matrigel is still fluid or cross-linked – the cross-linked gel does not flow anymore.
   ↪ If the gel does not cross-link even after repeated incubation, the Matrigel is degraded. Prepare a fresh 1:200 dilution and try again. If that still does not cross-link, the Matrigel aliquot itself is degraded. Thaw another aliquot according to the side note (see above) and try again.

7. Immediately, add some pre-warmed 4% formaldehyde solution for further chemical cross-linking. At best, keep it warm for the first minutes.

8. You can leave the specimen covered with the 4% Formaldehyde solution for final storage. This should already inhibit the growth of bacteria but to be sure, you can add 20 µl of 10% sodium azide. Seal LabTek with Parafilm.
   ↪ Samples prepared accordingly will last for weeks as long as the water does not evaporate.

5.3 Stage leveling

The leveling of the stage and possible re-alignment of the optics should only be performed by experienced users as it can get you into severe trouble otherwise.

It is easier to assess the leveling of the sample stage if there is no cylindrical lens in the detection path because the first step is to investigate the defocusing behavior of single TetraSpeck beads – the easiest in my opinion is to take a TetraSpeck surface as prepared in section 5.1. It is also advisable to first check the alignment only with the camera that is placed straight on the optical axis (camera 1 in Fig. 2.17) as the other has an additional degree of freedom – I will discuss that later in this protocol.
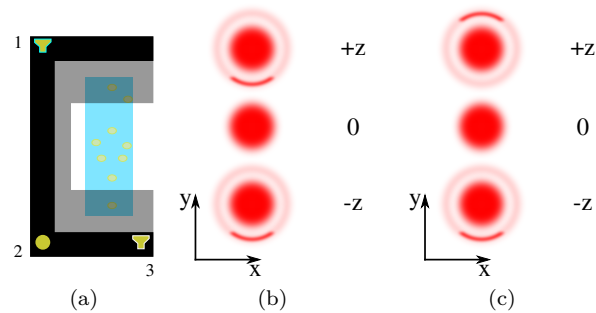
Figure 5.1: Here, two different kinds of PSF deformation as commonly encountered during the alignment of a 3D microscope and its sample stage a) are sketched. b) sketches that the PSF moves away from the center position upon de-focusing. It is important to note, that the displacement from the center goes to the same direction for positive and negative z. This is a typical sign for a tilted cover slip. In this example, the slope of the cover slip is positive for positive y and zero for x meaning that the stage has to be lowered at micrometer screw 1 in a) (1 and 3 are micrometer screws for tilt adjustment in x and y, while 2 is only a support point and not adjustable). c) on the other hand sketches that if any optics in the detection is off-axis, the light is imaged to the camera under an inclined angle. The displacement of the defocused PSF is not axially symmetric.

If the sample is tilted, the PSF will move away from the center position upon de-focusing the sample in a way depicted in Fig. 5.1b. The displacement is axially symmetric and has to be distinguished from the asymmetric movement depicted in Fig. 5.1c. If the specimen de-focuses as in Fig. 5.1c the general alignment of each lens in the detection path has to be doubted and thorough testing with different samples is mandatory. For this testing, an oil immersion objective should be used as it is not as sensitive to stage tilt. If all samples show the same PSF distortion, at least one lens is off axis what makes it necessary to re-align the detection optics.

If a de-focusing behavior similar to that in Fig. 5.1b is apparent, adjust the respective micrometer screw until no displacement is visible by eye. Then, add the cylindrical lens to the detection and again check, if the image of the sample stays roughly in the same position – then the cylindrical lens is most likely correctly aligned with the optical axis. Hint: Due to the extra focusing in only one direction the cylindrical lens will appear to shift the sample. In fact, this apparent shift originates from a change in magnification. If no displacement in

the other direction is visible and the PSF now spreads to a horizontal and a vertical ellipse upon de-focusing (cf. Fig. 5.2a), the alignment can be trusted for now.
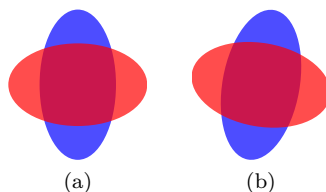

(a)   (b)

Figure 5.2: Twisted elliptic PSFs as encountered if the cylindrical lens is not aligned correctly. red: shape of the PSF in $+z$, blue: shape in $-z$.

If on the other hand, the stretched PSFs are tilted from a perfect horizontal– and vertical axis (cf. Fig. 5.2b) there are two possible reasons:

1. The cylindrical lens is off axis.

2. The cylindrical lens is twisted around the optical axis.

Reason 1 is easy to check: Displace the lens laterally to the optical axis and check if there is an impact on the orientation of the PSF. Hint: It is only reasonable to displace the lens in the direction in which the lens has a curvature. If any other possible explanation can be neglected, the initial alignment of the lens was bad and it is twisted around the axis. Turn the lens until the PSFs de-focus in the desired way (as in Fig. 5.2a).

Now, let us assume the PSF looks decent. We can now take a closer look whether the alignment is good enough or not. In order to finally check the fidelity of the stage leveling, take a z-stack of at least one – better several – TetraSpecks and localize its / their emission with rapi$d$STORM 3.3.1 (cf. section 5.4). If everything is precisely aligned, all localizations will be fit to a spot of about 20 nm or less as in Fig. 5.3a. If any false alignment is still apparent, the localizations will form a line as in Fig. 5.3b where the severe stretch originates from a mis-aligned imaging lens (the light incides on the camera under an angle) and the slight banana-like curvature stems from a slight cover slip tilt in x.

As mentioned before, it is harder to assess the quality of the stage leveling in the green channel. Because the light is redirected to the second camera by a dichroic beam splitter, there is an extra degree of freedom in aligning the imaging lens in front of the camera. If the beam splitter is in a wrong position or angle and that lateral shift is accounted for by adjusting the imaging lens,

(a)　　　　　(b)
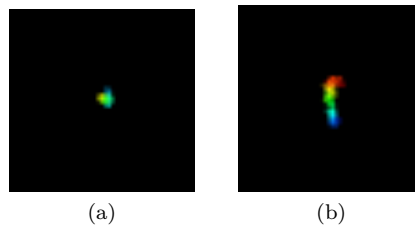
Figure 5.3: a) shows a bead with high lateral localization precision while b) corresponds to a bead with bad precision due to two mis-alignments: An imaging lens is off-axis and the stage is slightly tilted in x. Both images are x-y-representations with a pixel size of 10 nm and an axial range of ±500 nm. The color encodes the z-coordinate.

the light will not hit the sensor perpendicularly leading to the aforementioned lateral movement of the PSF upon de-focusing (cf. Fig. 5.1c). It often occurred that the localization precision in the red channel was good but pretty bad in the green channel. That is a good indicator that beam-splitter and final lens need a thorough re-alignment. It is simply a recommendation to first use only the red channel for checking the stage leveling because the quality may be harder to judge in the green channel as that one is in general harder to align. When happy with the red channel, a cross check of the green channel is nevertheless a good idea.

5.4 How to obtain proper 3D calibration curves

5.4.1 Red channel only

Needed software and sample:

- rapi*d*STORM 3.3.1[2]

- Micromanager 1.4.16[3] (other versions not tested)

- A programm like Gnuplot[4], Matlab[5] or Origin[6]

- Any of the samples described in sections 5.1 and 5.2

---

[2] www.super-resolution.biozentrum.uni-wuerzburg.de/research_topics/rapidstorm/
[3] www.micro-manager.org
[4] www.gnuplot.info
[5] www.mathworks.com/products/matlab/
[6] www.originlab.com

Aquisition of calibration data:

1. Start Micromanager and load a hardware configuration only involving the camera for red imaging.
   ↪ The green channel will later be used as a slave channel to the red master camera and will not be controlled by Micromanager.

2. Set the camera settings to appropriate values and set the Exposure to 100 ms in the main window.

3. Press the Live button for a live view.

4. Place the specimen on the microscope and focus on a TetraSpeck bead.
   ↪ Check quickly, if the PSF appears distorted in any way (cf. section 5.3). Assuming that everything looks OK:

5. Restrict the image acquisition to a region of interest (ROI) with only one bead that looks decent.

6. Open the Multi-dimensional Acquisition dialogue by pressing the Multi-D Acq. button.

   a) Tick the Z-stacks (slices) box. Un-check any other box. Set the following values:

      - Z-start [um]: -2
      - Z-end [um]: 2
      - Z-step [um]: 0,01
      - Choose relative Z from the drop-down menu.
      - Tick the Keep shutter open box.

   b) Tick the Save images box. Set the Directory root where you want to save your measurements and a Name prefix. Choose the Saving format to be Image stack file.

   c) The Summary indicates the length of the measurement (Total images). In this example this is 401 frames. Remember this value if you want to do a two color calibration.

   d) Start the data acquisition by pressing the Acquire! button.

Evaluation of the data and how to judge its quality:

1. Open rapi*d*STORM 3.3.1.

   a) Load the .tif file.

   b) Set the Size of input pixel correctly.

   c) Set the Intensity threshold to a reasonable value.

   d) Choose a higher Fit window radius. 1100 nm is a good value. Remember this value!

   ↪ It does not make sense to only give rapi*d*STORM a small Fit window as the de-focused PSFs we want to calibrate are significantly larger than sharp foci.

   ↪ It is indeed mandatory to remember this value as we will need it as an input for the evaluation of *every* measurement that is to be calibrated with the calibration file we will generate in this protocol.

   e) Tick the PSF width is free fit parameter box.

   f) Tick the Store PSF width box.

   g) Go to the Expression filter.

   - Set Number of expressions to at least 4.

   - Enter the Value to assign from drop-down menu and choose posz.

   - Give rapi*d*STORM information about the axial movement that took place during the acquisition, i.e., assign a *z*-coordinate by `10 nm/fr * frame`

   - Choose new output: Count localizations
     ↪ It is nice to validate that you have one localization per frame for the bead you calibrate with.

   h) Press the Run button.

2. The output of this first step is going to look pretty bad which is natural as we did not apply any filtering yet. Especially, we allowed localizations from the whole axial range of 4 µm which, combined with fitting to free PSF widths, leads to the localization of virtually everything, including noise and dirt. We will now find valid filters for the extraction of a 3D calibration curve:

3. You should have one bright spot where the bead supposedly lies. Try getting rid of noise by applying some of the following filters.

- Set the Minimum localization strength to a value that deletes some noise but leaves the wanted localizations unaffected.

- `psffwhmx < 3000 nm && psffwhmy < 3000 nm`
  ↪ Until now we allowed every PSF width. With this filter, the totally unphysical localizations are deleted (PSFs of this size do not occur for 100 nm beads).

- Also a spatial filter around the supposed bead coordinates is often reasonable.
  ↪ Example: `posx < 3000 nm && posx > 2000 nm`
  `&& posy > 3000 nm && posy < 4000 nm`

4. Take the localization file and plot columns 6 (PSF-FWHM$_x$) and 7 (PSF FWHM$_y$) against column 3 (assigned z-coordinate).
   ↪ To get this straight: Column 3 shall be the x-axis of the plot.

5. Find characteristics of the remaining spurious localizations, e.g., their minimum PSF size, brightness or lateral position. Filter those with rapi*d*STORM and re-plot the localization file.

6. We take the crossing point of the two graphs for the PSF FWHM in x and y as the (arbitrarily set) zero for the later 3D calibration file. Extract the z-coordinate of that crossing point and enter it to rapi*d*STORM by modifying the assignment of the z-coordinate `10 nm/fr * frame` accordingly.
   ↪ Example: Crossing point is at $z = 1100$ nm.
   ↪ Modification: `10 nm/fr * frame - 1100 nm`

7. Now, you can directly restrict the data to a reasonable axial range – significantly more than 1 µm axial range is not realistic for single fluorophores – by setting the filter `posz > -500 nm && posz < 500 nm`

8. Do not close this localization job yet, as we will need the settings we just entered!

9. Re-load the filtered localization file to your plotting program and check, if the plots for the PSF FWHM are smooth or if there is still any noise.

10. Also check the lateral localization precision by evaluating the spread of the found x-coordinates and the found y-coordinates.
    ↪ If the precision is significantly higher than 20 nm you can consider to either try to restrict the axial range even more – but a too short range is

seldom desirable – or to try another sample and check whether the findings are consistent. If that was the case, some re-adjustment of the stage and / or optics might be necessary (cf. section 5.3).

11. Supposing the last step yielded satisfying results, we can now generate the 3D PSF width calibration table.

    a) Go back to the Job options tab – do not close your localization job as we need the filters.

    b) Copy Minimum localization strength, filters and the string assigning the z-coordinate from the dStorm job tab we just used to the Job options tab.

    c) Choose new output 3D PSF width calibration table.
       ↪ In this output, the name of the calibration table and the amount of knots used for the evaluation of the cubic B-spline can be set. Usually, there is no need to change these settings.

12. Run evaluation by pressing the Run button.
    ↪ rapi*d*STORM will generate an additional text file to the familiar localizations– and settings file. The new file has the default name *name of the measurement*-sigma-table.txt. It consists of one column with the z-coordinates of the knots used for the cubic B-spline and two columns for the respective amplitude factors in x and y. See section 2.2.1.1 for further information. This text file is the calibration table you will need when evaluating subsequent 3D measurements.

Evaluation of 3D data using a B-Spline 3D PSF width calibration table:

- Open a new instance of rapi*d*STORM.

- Set 3D PSF model to Interpolated 3D.

- Load the 3D PSF width calibration table – default file suffix is -sigma-table.txt

- Set the Fit window radius to *the same* value used for evaluation of the calibration table – 1100 nm in this example.

- Set the image display options to serve your needs, e.g., color coding the output by z-coordinate.

- Recommendation: Again, set the Number of Expressions to at least 4, because for investigating the quality of the measurement, often many filters are helpful.

- Run the job. This will take significantly longer as for 2D evaluations.

- Have a sharp look, if the output is consistent. A good check are x-z-cross-sections that will uncover layering artifacts and axial regions with false localizations. Further information is given in section 2.2.2.

5.4.2 Both red– and green channel

Needed software and sample:

- Same as in section 5.4.1

- Andor Solis[7]

Aquisition of calibration data:

1. Follow the instructions in section 5.4.1. Before starting the experiment follow these steps for simultaneous acquisition of the data of the green channel:

2. Start Andor Solis. As mentioned before, the camera for the green channel will be used as slave.

   - Open the shutter.

   - Navigate to the Acquisition Setup dialogue and set the Triggering option to External and the Exposure Time to the minimum value.
   ↪ Set the Length of the Kinetic Series to be one frame less than the length of the red measurement – in this example: 400.
   ↪ With every frame, the red camera sends a fire pulse to the green camera, so if the red camera is not running, neither will the green camera.

   - Enable spooling, choose a file location and .tif as file format.

3. Set the camera to a ROI around the same bead as in the red channel.

4. Disable the live view of the red camera.

---

[7] www.andor.com/solis

5. Press the Take Signal button in Andor Solis for the green camera *prior to data acquisition by the red channel.*

6. Start the data acquisition by pressing the Acquire! button in Micromanager. What happens:
   ↪ The acquisition of the red channel starts.
   ↪ *After* the first frame of the red channel the first fire pulse is sent to the green camera. The green channel starts the acquisition. That offset of one frame is to be kept in mind for the later evaluation.

Evaluation of the data and how to judge its quality:

- Follow the instructions for the evaluation of the red channel (section 5.4.1).

- Remember to check the Mirror data along Y axis box.

- Remember that the green data is shifted one frame against the red data. It is necessary to use the same zero coordinate for the z calibration files in both channels because otherwise there will be an axial offset between corresponding data in red and green.

- Account for that shift by assigning the z coordinate accordingly.
  ↪ Example: In the red channel `10 nm/fr * frame - 1100 nm` was assigned to posz
  ↪ The correct input for the green channel is `10 nm/fr * frame - 1090 nm`.

5.5 Two-color channel alignment with a raw transformation matrix

5.5.1 Acquisition and evaluation of two color alignment data with rapi*d*STORM 3.3.1

1. Make sure to have installed rapi*d*STORM 3.3.1[8]. Other versions might crash.

2. Simultaneously record data of fluorescent beads (100 nm TetraSpecks) with both cameras. Do not use a bought calibration sample but use TetraSpecks in aqueous environment. If the alignment can be trusted you can axially

---

[8]http://www.super-resolution.biozentrum.uni-wuerzburg.de/research_topics/rapidstorm/

scan through TetraSpecks immersed in Matrigel despite taking data from different regions of a TetraSpeck surface to get enough beads.

3. Evaluate both channels with rapi*d*STORM 3.3.1 and make use of the following settings:

   - Flip the green channel along the *y*-axis.

   - Set the Size of the input pixel accordingly (and to the same values used during the generation of the raw transformation file and the 3D PSF width calibration table).

   - Set 3D PSF model to Interpolated 3D and load the appropriate (B-spline) calibration file by using the Select button.

   - Filter: `posz > -250 nm && posz < 250 nm`
     $\hookrightarrow$ If the axial range is too long, it becomes likely, that localizations are filtered in one channel while still apparent in the other. For the calculation of the transformation, both channels need to contain the same localizations. A too narrow axial range is not reasonable because the transformation should fit to the later experiments. Also a too narrow range may lead to localizations that are not apparent in both channels.

   - Filter with high Minimum localization strength because noise would also disturb the transformation.

   - Histogram normalization can be set to 0.3 for better visibility even though 0 would theoretically be more precise. Avoid too high contrast by setting to a high value, because that would overemphasize noise.

   - Set Colour palette for display to Constant colour and Select colour hue to 0.3 for the green channel and 0.9 for the red channel.

   - Remember the pixel sizes set (default: 10 nm for *x* and *y*) for the resultant images as they will later be needed for the evaluation of two color measurements with automatic transformation.

5.5.2 Generation of a raw transformation with the Fiji plugin bUnwarpJ

1. Load both .png images created by rapi*d*STORM in Fiji[9]. As long as the ROI in both channels was the same, you do not have to worry about dif-

---

[9] http://fiji.sc/Fiji

ferent image sizes as they originate from the fact that in two color 3D the pixel sizes or the two respective channels are slightly different (even a good achromatic cylindrical lens is not perfect).

2. Navigate through the menu: Plugins → Registration → bUnwarpJ

3. Use the following settings. Leave settings set to default values if there is no reason to do otherwise:

   - Source Image: red channel, Target Image: green channel
     ↪ The final transformation will later be applied to the green channel in rapi*d*STORM 3.3.1!

   - Registration Mode: Mono
     ↪ "Accurate" would find the best transformation for red to green *and* green to red. This is not supported by rapi*d*STORM.

   - Initial Deformation: Coarse
     ↪ As the data is very sparse, a setting to a high value will only overemphasize local disturbances.

   - Final Deformation: Very Fine
     ↪ Same reason as for Initial Deformation.

   - Divergence Weight: 0 (default value)

   - Curl Weight: 0 (default value)

   - Landmark Weight: a value between 0 and 0.5
     ↪ It is often helpful to set *some* landmarks, e.g., one in each corner and one in the middle to give the algorithm some initial values. However, at least try once if the algorithm does find a good transformation without any landmarks as erroneously set landmarks can hamper the result. Setting the landmark weight to a high value will overemphasize erroneously set landmarks and give the algorithm a bad initial value.

   - Image Weight: 1
     ↪ The image should be of highest importance for the transformation algorithm.

   - (Consistency Weight: 10 (default value, cannot be adjusted))

   - Stop Threshold: 0.01 (default value)

   - Tick Verbose box.

- Tick Save Transformation box.
  ↪ If the box was not ticked, only the two images would be aligned but the found elastic transformation (needed for later use) would not be saved.

- *Do not hit the OK button yet* unless you know you do not need landmarks.

- Now, set some landmarks if necessary using the according symbols of the Fiji task bar. Make sure, the landmarks are set to the same respective beads in both channels.

- Go to the bUnwarpJ menu – an icon resembling a letter – and save the landmarks to a text file (Save Landmarks As...). If anything went wrong with the transformation you don't want to do all the work again in a second try.

- Hit the OK button.
  ↪ The algorithm now aligns both images and will ask you where to save the transformation file. This may take a while.

- Close all bUnwarpJ windows and re-load the localized images created by rapi*d*STORM in order to check whether the obtained transformation is reasonable.

  - Open bUnwarpJ again and set Source– and Target Image and Registration Mode accordingly.

  - Navigate to the bUnwarpJ menu and choose Load Elastic Transformation.
    ↪ The two images will now be transformed. Close all bUnwarpJ windows (despite the transformed images) and create an overlay of both images(Fiji menu → Process → Image Calculator). For better visibility, the contrast can be enhanced (Ctrl + Shift + c). Check by eye, if there is a bead in the green channel for each bead in the red channel and if they coincide. Hint: A perfect co-localization of green and magenta results in white.

  - If the result is not satisfying, try again using slightly different settings or landmarks. If nothing helps, try another set of data. Maybe something went wrong during the acquisition and / or evaluation.

- If the result looks good, navigate a last time to the bUnwarpJ plugin. I don't know whether or not it has any impact (in theory it should not) but you may want to set the same settings as for the generation of the elastic transformation.
↪ Open the bUnwarpJ menu and choose Convert Transformation To Raw. Navigate to the elastic transformation you just saved and load it. Immediately, another window will open that looks similar to the load dialogue. Do not be confused: This is the save dialogue so type in a file name of your choice – do not forget the suffix .txt – and hit Open (Yes, a bit misleading...). The resultant file will have a size of a few hundred megabytes.

4. You are now finished. You can close Fiji and start evaluating your two color 3D data.

5.5.3 Evaluation of two color 3D data using rapi*d*STORM 3.3.1 with automatic alignment of both channels

1. Apply the transformation to the measurement that was taken as target for the generation of the raw transformation file. In this protocol the channel that is to be transformed is the green channel. Be aware that the transformation is only valid for measurements taken in the same ROI as the data that was used for the generation of the raw transformation.

2. Make sure that the Mirror data along Y-axis box is checked.

3. Set the Size of the input pixel accordingly (and to the same values used during the generation of the raw transformation file and the 3D PSF width calibration table).

4. Set 3D PSF model to Interpolated 3D and load the appropriate (B-spline) calibration file by using the Select button.

5. Change the Plane alignment setting to Support point alignment and load the raw transformation file via the Select button. Drag and drop may cause a crash of the software.

6. For transformation resolution enter the pixel sizes of the images used to generate the raw transformation (default value and the value used in this protocol is 10 nm for x and y).

7. Set the Number of expressions in the Expression filter to a higher value – at least 5 – because four are needed to enter necessary values and one should be left for the ability to filter the data.

8. Change Value to assign to from Filter to the following variables:

   - minposx
   - maxposx
   - minposy
   - maxposy

9. Set Expression to assign from to the according values of the red channel. Example: Transformation took place with images that have a pixel size of 10 nm. The size of the red image is 2168 pixel in x and 2805 pixel in y.

   - Set minposx and minposy both to 0 nm.
     ↪ If this value is not set, it can happen that the green channel is transformed correctly but is (constantly) shifted against the red channel by some pixel.
   - Set maxposx to 21680 nm or 2168 px. Both expressions are valid.
   - Set maxposy to 28050 nm or 2805 px.
     ↪ If the values for maxposx and maxposy are not set, rapi*d*STORM will either give no result or an error upon running the evaluation or might even crash because the algorithm does not have any information of the dimensions of the resultant image.

10. You are now ready to run the rapi*d*STORM evaluation by pressing the Run button.

Bibliography

E. Abbe. Beiträge zur Theorie des Mikroskops und der mikroskopischen Wahrnehmung. *Archiv für Mikroskopische Anatomie*, 9(1):413–418, December 1873. URL http://www.springerlink.com/content/k7154700k345404p/.

R. Arimoto and J. M. Murray. A common aberration with water-immersion objective lenses. *Journal of Microscopy*, 216(1):49–51, 2004. ISSN 1365-2818. URL http://dx.doi.org/10.1111/j.0022-2720.2004.01383.x.

D. Baddeley, M. Cannell, and C. Soeller. Three-dimensional sub-100 nm super-resolution imaging of biological samples using a phase ramp in the objective pupil. *Nano Research*, 4:589–598, 2011. ISSN 1998-0124. URL http://dx.doi.org/10.1007/s12274-011-0115-z.

M. Bates, T. R. Blosser, and X. Zhuang. Short-Range Spectroscopic Ruler Based on a Single-Molecule Optical Switch. *Physical Review Letters*, 94(10):108101, 2005. URL http://link.aps.org/abstract/PRL/v94/e108101.

E. Betzig, G. H. Patterson, R. Sougrat, O. W. Lindwasser, S. Olenych, J. S. Bonifacino, M. W. Davidson, J. Lippincott-Schwartz, and H. F. Hess. Imaging Intracellular Fluorescent Proteins at Nanometer Resolution. *Science*, 313 (5793):1642–1645, 2006. URL http://www.sciencemag.org/cgi/content/abstract/313/5793/1642.

J. S. Biteen, E. D. Goley, L. Shapiro, and W. E. Moerner. Three-Dimensional Super-Resolution Imaging of the Midplane Protein FtsZ in Live Caulobacter crescentus Cells Using Astigmatism. *ChemPhysChem*, 13(4):1007–1012, 2012. ISSN 1439-7641. URL http://dx.doi.org/10.1002/cphc.201100686.

M. Born and E. Wolf. *Principles of Optics: Electromagnetic Theory of Propagation, Interference and Diffraction of Light*. Cambridge University Press, 2002. ISBN 9781139643405.

M. Brenner, S. Schwartz, T. J. Fellers, and M. W. Davidson. Water Immersion Objectives. 2014. URL http://www.microscopyu.com/articles/optics/waterimmersionobjectives.html. accessed: July 18, 2014.

M. K. Cheezum, W. F. Walker, and W. H. Guilford. Quantitative Comparison of Algorithms for Tracking Single Fluorescent Particles. *Biophysical Journal*, 81(4):2378–2388, October 2001. URL http://www.biophysj.org/cgi/content/abstract/81/4/2378.

K. Chung and K. Deisseroth. CLARITY for mapping the nervous system. *Nature Methods*, 10(6):508–513, June 2013. ISSN 1548-7091. URL http://dx.doi.org/10.1038/nmeth.2481.

A. Dani, B. Huang, J. Bergan, C. Dulac, and X. Zhuang. Superresolution Imaging of Chemical Synapses in the Brain. *Neuron*, 68(5):843–856, December 2010. ISSN 0896-6273. URL http://linkinghub.elsevier.com/retrieve/pii/S0896627310009372.

W. Demtröder. *Experimentalphysik 2: Elektrizität und Optik.* Springer-Lehrbuch. Springer, 2006. ISBN 9783540337942.

Y. Deng and J. W. Shaevitz. Effect of aberration on height calibration in three-dimensional localization-based microscopy and particle tracking. *Applied Optics*, 48(10):1886–1890, April 2009. URL http://ao.osa.org/abstract.cfm?URI=ao-48-10-1886.

A. Diaspro, F. Federici, and M. Robello. Influence of refractive-index mismatch in high-resolution three-dimensional confocal microscopy. *Applied Optics*, 41(4):685–690, February 2002. URL http://ao.osa.org/abstract.cfm?URI=ao-41-4-685.

Y. Dong and C. Shannon. Heterogeneous Immunosensing Using Antigen and Antibody Monolayers on Gold Surfaces with Electrochemical and Scanning Probe Detection. *Analytical Chemistry*, 72(11):2371–2376, 2000. URL http://dx.doi.org/10.1021/ac991450g.

M. Galassi, J. Davies, J. Theiler, B. Gough, G. Jungman, M. Booth, and F. Rossi. *Gnu Scientific Library: Reference Manual.* Network Theory Ltd., February 2003. ISBN 0954161734.

C. G. Galbraith and J. A. Galbraith. Super-resolution microscopy at a glance. *Journal of Cell Science*, 124(10):1607–1611, 2011. URL http://jcs.biologists.org/content/124/10/1607.short.

M. G. L. Gustafsson. Surpassing the lateral resolution limit by a factor of two using structured illumination microscopy. *Journal of Microscopy*, 198(2):82–87, 2000. doi: 10.1046/j.1365-2818.2000.00710.x.

E. Hecht. *Optics*. Addison-Wesley Longman, Incorporated, 2002. ISBN 9780805385663.

E. Hecht. *Optik*. Oldenbourg, 6th edition, 2014. ISBN 9783110347968.

M. Heilemann, E. Margeat, R. Kasper, M. Sauer, and P. Tinnefeld. Carbocyanine Dyes as Efficient Reversible Single-Molecule Optical Switch. *Journal of the American Chemical Society*, 127(11):3801–3806, March 2005. URL http://dx.doi.org/10.1021/ja044686x.

M. Heilemann, S. van de Linde, M. Schüttpelz, R. Kasper, B. Seefeldt, A. Mukherjee, P. Tinnefeld, and M. Sauer. Subdiffraction-Resolution Fluorescence Imaging with Conventional Fluorescent Probes. *Angewandte Chemie International Edition*, 47(33):6172–6176, 2008. URL http://dx.doi.org/10.1002/anie.200802376.

M. Heilemann, S. van de Linde, A. Mukherjee, and M. Sauer. Super-resolution imaging with small organic fluorophores. *Angewandte Chemie International Edition*, 48(37):6903–6908, 2009. URL http://dx.doi.org/10.1002/anie.200902073.

S. Hell, G. Reiner, C. Cremer, and E. H. K. Stelzer. Aberrations in confocal fluorescence microscopy induced by mismatches in refractive index. *Journal of Microscopy*, 169(3):391–405, 1993. ISSN 1365-2818. URL http://dx.doi.org/10.1111/j.1365-2818.1993.tb03315.x.

S. W. Hell and J. Wichmann. Breaking the diffraction resolution limit by stimulated emission: stimulated-emission-depletion fluorescence microscopy. *Optics Letters*, 19(11):780, 1994. URL http://ol.osa.org/abstract.cfm?URI=ol-19-11-780.

R. Henriques, M. Lelek, E. F. Fornasiero, F. Valtorta, C. Zimmer, and M. M. Mhlanga. QuickPALM: 3D real-time photoactivation nanoscopy image processing in ImageJ. *Nature Methods*, 7(5):339–340, May 2010. ISSN 1548-7091. URL http://dx.doi.org/10.1038/nmeth0510-339.

S. T. Hess, T. P. Girirajan, and M. D. Mason. Ultra-High Resolution Imaging by Fluorescence Photoactivation Localization Microscopy. *Biophysical Journal*, 91(11):4258–4272, December 2006. URL http://dx.doi.org/10.1529/biophysj.106.091116.

L. Holtzer, T. Meckel, and T. Schmidt. Nanometric three-dimensional tracking of individual quantum dots in cells. *Applied Physics Letters*, 90(5):053902, 2007. URL http://link.aip.org/link/?APL/90/053902/1.

B. Huang, S. A. Jones, B. Brandenburg, and X. Zhuang. Whole-cell 3D STORM reveals interactions between cellular structures with nanometer-scale resolution. *Nature Methods*, 5(12):1047–1052, December 2008a. ISSN 1548-7091. URL http://dx.doi.org/10.1038/nmeth.1274.

B. Huang, W. Wang, M. Bates, and X. Zhuang. Three-Dimensional Super-Resolution Imaging by Stochastic Optical Reconstruction Microscopy. *Science*, 319(5864):810–813, February 2008b. ISSN 1095-9203. URL http://dx.doi.org/10.1126/science.1153529.

J. Huisken, J. Swoger, F. Del Bene, J. Wittbrodt, and E. H. K. Stelzer. Optical Sectioning Deep Inside Live Embryos by Selective Plane Illumination Microscopy. *Science*, 305(5686):1007–1009, 2004. URL http://www.sciencemag.org/content/305/5686/1007.abstract.

M. F. Juette, T. J. Gould, M. D. Lessard, M. J. Mlodzianoski, B. S. Nagpure, B. T. Bennett, S. T. Hess, and J. Bewersdorf. Three-dimensional sub-100 nm resolution fluorescence microscopy of thick samples. *Nature Methods*, 5(6):527–529, June 2008. ISSN 1548-7091. URL http://dx.doi.org/10.1038/nmeth.1211.

P. Kanchanawong, G. Shtengel, A. M. Pasapera, E. B. Ramko, M. W. Davidson, H. F. Hess, and C. M. Waterman. Nanoscale architecture of integrin-based cell adhesions. *Nature*, 468(7323):580–584, November 2010. ISSN 0028-0836. URL http://dx.doi.org/10.1038/nature09621.

H. Kao and A. Verkman. Tracking of single fluorescent particles in three dimensions: use of cylindrical optics to encode particle position. *Biophysical Journal*, 67(3):1291–1300, September 1994. ISSN 0006-3495. URL http://linkinghub.elsevier.com/retrieve/pii/S0006349594806010.

T. Klein, S. Proppert, and M. Sauer. Eight years of single-molecule localization microscopy. *Histochemistry and Cell Biology*, 141(6):561–575, 2014. ISSN 0948-6143. URL http://dx.doi.org/10.1007/s00418-014-1184-3.

L. Lau, Y. Lee, S. Sahl, T. Stearns, and W. Moerner. STED Microscopy with Optimized Labeling Density Reveals 9-Fold Arrangement of a Centriole Protein. *Biophysical Journal*, 102(12):2926 – 2935, 2012. ISSN 0006-3495. URL http://www.sciencedirect.com/science/article/pii/S0006349512005681.

S. Lawo, M. Hasegan, G. D. Gupta, and L. Pelletier. Subdiffraction imaging of centrosomes reveals higher-order organizational features of pericentriolar material. *Nature Cell Biology*, 14(11):1148–1158, November 2012. ISSN 1465-7392. URL http://dx.doi.org/10.1038/ncb2591.

K. Lidke, B. Rieger, T. Jovin, and R. Heintzmann. Superresolution by localization of quantum dots using blinking statistics. *Optics Express*, 13(18):7052–7062, September 2005. URL http://www.opticsexpress.org/abstract.cfm?URI=oe-13-18-7052.

A. Löschberger, S. van de Linde, M.-C. Dabauvalle, B. Rieger, M. Heilemann, G. Krohne, and M. Sauer. Super-resolution imaging visualizes the eightfold symmetry of gp210 proteins around the nuclear pore complex and resolves the central channel with nanometer resolution. *Journal of Cell Science*, 125 (3):570–575, 2012. URL http://jcs.biologists.org/content/125/3/570.abstract.

R. McGorty, J. Schnitzbauer, W. Zhang, and B. Huang. Correction of depth-dependent aberrations in 3D single-molecule localization and super-resolution microscopy. *Optics Letters*, 39(2):275–278, January 2014. URL http://ol.osa.org/abstract.cfm?URI=ol-39-2-275.

K. I. Mortensen, L. S. Churchman, J. A. Spudich, and H. Flyvbjerg. Optimized localization analysis for single-molecule tracking and super-resolution microscopy. *Nature Methods*, 7(5):377–381, May 2010. ISSN 1548-7091. URL http://dx.doi.org/10.1038/nmeth.1447.

J. A. Nelder and R. Mead. A Simplex Method for Function Minimization. *The Computer Journal*, 7(4):308–313, 1965. URL http://comjnl.oxfordjournals.org/cgi/content/abstract/7/4/308.

J. U. O'Connor, C. M. & Adams. *Essentials of Cell Biology*. Cambridge, MA: NPG Education, 2010.

N. Olivier, D. Keller, P. Gönczy, and S. Manley. Resolution Doubling in 3D-STORM Imaging through Improved Buffers. *PLoS ONE*, 8(7):e69004, 07 2013. URL http://dx.doi.org/10.1371%2Fjournal.pone.0069004.

S. R. P. Pavani, M. A. Thompson, J. S. Biteen, S. J. Lord, N. Liu, R. J. Twieg, R. Piestun, and W. E. Moerner. Three-dimensional, single-molecule fluorescence imaging beyond the diffraction limit by using a double-helix point spread function. *Proceedings of the National Academy of Sciences of the United States of America*, 106(9):2995–2999, 2009. URL http://www.pnas.org/content/106/9/2995.abstract.

J. E. Pawley. *Handbook of Biological Confocal Microscopy*. Springer, 2006. ISBN 9780387259215.

S. Proppert, S. Wolter, T. Holm, T. Klein, S. van de Linde, and M. Sauer. Cubic B-spline calibration for 3D super-resolution measurements using astigmatic imaging. *Optics Express*, 22(9):10304–10316, May 2014. URL http://www.opticsexpress.org/abstract.cfm?URI=oe-22-9-10304.

L. Rayleigh. On the Theory of Optical Images, with Special Reference to the Microscope. *Journal of the Royal Microscopical Society*, 23(4):447–473, 1903. ISSN 1365-2818. URL http://dx.doi.org/10.1111/j.1365-2818.1903.tb04830.x.

M. J. Rust, M. Bates, and X. Zhuang. Sub-diffraction-limit imaging by stochastic optical reconstruction microscopy (STORM). *Nature Methods*, 3(10):793–795, October 2006. URL http://dx.doi.org/10.1038/nmeth929.

J. J. Schmied, M. Raab, C. Forthmann, E. Pibiri, B. Wünsch, T. Dammeyer, and P. Tinnefeld. DNA origami-based standards for quantitative fluorescence microscopy. *Nat. Protocols*, 9(6):1367–1391, June 2014. ISSN 1754-2189. URL http://dx.doi.org/10.1038/nprot.2014.079.

K. Schücker, T. Holm, C. Franke, M. Sauer, and R. Benavente. Elucidation of synaptonemal complex organization by superresolution imaging with isotropic resolution. 2014. submitted.

G. J. Schütz, V. P. Pastushenko, H. J. Gruber, H.-G. Knaus, B. Pragl, and H. Schindler. 3D Imaging of Individual Ion Channels in Live Cells at 40nm Resolution. *Single Molecules*, 1(1):25–31, 2000. ISSN 1438-5171. URL http://dx.doi.org/10.1002/(SICI)1438-5171(200004)1:1<25::AID-SIMO25>3.0.CO;2-O.

G. J. Schütz, M. Axmann, and H. Schindler. Imaging Single Molecules in Three Dimensions. *Single Molecules*, 2(2):69–74, 2001. ISSN 1438-5171. URL http://dx.doi.org/10.1002/1438-5171(200107)2:2<69::AID-SIMO69>3.0.CO;2-N.

C. Shannon. Communication in the Presence of Noise (reprinted). *Proceedings of the IEEE*, 72(9):1192–1201, 1984. ISSN 0018-9219.

C. J. R. Sheppard and P. Török. Effects of specimen refractive index on confocal imaging. *Journal of Microscopy*, 185(3):366–374, 1997. ISSN 1365-2818. URL http://dx.doi.org/10.1046/j.1365-2818.1997.d01-627.x.

G. Shtengel, J. A. Galbraith, C. G. Galbraith, J. Lippincott-Schwartz, J. M. Gillette, S. Manley, R. Sougrat, C. M. Waterman, P. Kanchanawong, M. W. Davidson, R. D. Fetter, and H. F. Hess. Interferometric fluorescent super-resolution microscopy resolves 3D cellular ultrastructure. *Proceedings of the National Academy of Sciences of the United States of America*, 106(9):3125–3130, 2009. URL http://www.pnas.org/content/106/9/3125.abstract.

S. Stallinga and B. Rieger. Accuracy of the Gaussian Point Spread Function model in 2D localization microscopy. *Optics Express*, 18(24):24461–24476, November 2010. URL http://www.opticsexpress.org/abstract.cfm?URI=oe-18-24-24461.

R. E. Thompson, D. R. Larson, and W. W. Webb. Precise Nanometer Localization Analysis for Individual Fluorescent Probes. *Biophysical Journal*, 82(5):2775–2783, 2002. URL http://www.biophysj.org/cgi/content/abstract/82/5/2775.

103

M. Tokunaga, N. Imamoto, and K. Sakata-Sogawa. Highly inclined thin illumination enables clear single-molecule imaging in cells. *Nature Methods*, 5 (2):159–161, February 2008. ISSN 1548-7091. URL http://dx.doi.org/10.1038/nmeth1171.

S. van de Linde and M. Sauer. How to switch a fluorophore: from undesired blinking to controlled photoswitching. *Chemical Society Reviews*, 43:1076–1087, 2014. URL http://dx.doi.org/10.1039/C3CS60195A.

S. van de Linde, S. Wolter, M. Heilemann, and M. Sauer. The effect of photoswitching kinetics and labeling densities on super-resolution fluorescence imaging. *Journal of Biotechnology*, 149(4):260–266, 2010. ISSN 0168-1656. URL http://dx.doi.org/10.1016/j.jbiotec.2010.02.010.

S. van de Linde, A. Loschberger, T. Klein, M. Heidbreder, S. Wolter, M. Heilemann, and M. Sauer. Direct stochastic optical reconstruction microscopy with standard fluorescent probes. *Nature Protocols*, 6(7):991–1009, June 2011. ISSN 1754-2189. URL http://dx.doi.org/10.1038/nprot.2011.336.

D. Wengler. Immobilisierung einzelner Zellen für die hochauflösende Lichtblattmikroskopie. Master's thesis, Bielefeld University, July 2012.

D. Wettstein, S. W. Rasmussen, and P. B. Holm. The Synaptonemal Complex in Genetic Segregation. *Annual Review of Genetics*, 18(1):331–411, 1984. URL http://dx.doi.org/10.1146/annurev.ge.18.120184.001555.

S. Wolter. An accurate and efficient algorithm for real-time localisation of photoswitchable fluorophores. Master's thesis, Bielefeld University, March 2009.

S. Wolter, A. Löschberger, T. Holm, S. Aufmkolk, M.-C. Dabauvalle, S. van de Linde, and M. Sauer. rapi*d*STORM: accurate, fast open-source software for localization microscopy. *Nature Methods*, 9(11):1040–1041, Nov. 2012a. ISSN 1548-7091. URL http://dx.doi.org/10.1038/nmeth.2224.

S. Wolter, S. Proppert, S. Aufmkolk, A. Lampe, and T. Klein. rapi*d*STORM manual. 2012b. URL http://www.super-resolution.de/home/rapidstorm/.

K. Xu, H. P. Babcock, and X. Zhuang. Dual-objective STORM reveals three-dimensional filament organization in the actin cytoskeleton. *Nature Methods*, 9(2):185–188, February 2012. ISSN 1548-7091. URL http://dx.doi.org/10.1038/nmeth.1841.

P. J. Zessin, C. L. Krüger, S. Malkusch, U. Endesfelder, and M. Heilemann. A hydrophilic gel matrix for single-molecule super-resolution microscopy. *Optical Nanoscopy*, 2(1):4–4, 2013. ISSN 2192-2853. URL http://dx.doi.org/10.1186/2192-2853-2-4.